BRNO UNIVERSITY OF TECHNOLOGY
VYSOKÉ UČENÍ TECHNICKÉ V BRNĚ

FACULTY OF ELECTRICAL ENGINEERING AND COMMUNICATION
FAKULTA ELEKTROTECHNIKY
A KOMUNIKAČNÍCH TECHNOLOGIÍ

DEPARTMENT OF MICROELECTRONICS
ÚSTAV MIKROELEKTRONIKY

IMPLEMENTATION OF A MULTIPURPOSE MEASUREMENT SYSTEM FOR (SUB)TERAHERTZ ELECTRON SPIN RESONANCE SPECTROSCOPY

REALIZACE VÍCEÚČELOVÉHO MĚŘÍCÍHO SYSTÉMU PRO (SUB)TERAHERTZOVOU ELEKTRONOVOU SPINOVOU REZONANČNÍ SPEKTROSKOPII

DOCTORAL THESIS
DIZERTAČNÍ PRÁCE

AUTHOR AUTOR PRÁCE	Ing. Matúš Šedivý
SUPERVISOR ŠKOLITEL	prof. Ing. Radimír Vrba, CSc.
CO-SUPERVISORS ŠKOLITELÉ SPECIALISTI	doc. Ing. Petr Neugebauer Ph.D. and Dr. Oleksii Laguta

BRNO 2024

Abstract

Electron spin resonance (also called electron paramagnetic resonance or just EPR) spectroscopy includes methods that investigate matter via unpaired electrons. One of the progressive EPR methods is the rapid scan, which allows one to observe the kinetics of chemical reactions. Moreover, recent developments of high-frequency components expand application of high-frequency EPR (HFEPR), that use sub-terahertz and terahertz waves. This thesis deals with the connection of both paths into the frequency rapid scan (FRaScan) HFEPR spectrometer that was recently developed at CEITEC BUT. A brief introduction to the theoretical background of EPR is provided, followed by an overview of the HFEPR instrumentation. The practical part describes a technical solution for the spectrometer. The emphasis is on the implementation of software through which the spectrometer is controlled, and measurements are automated. Afterward are shown example measurements of solid state materials, namely vanadium doped silicon carbide (SiC:V), lithium phthalocyanine (LiPc), and crystal of 1,3-bisdiphenylene-2-phenylallyl (BDPA). The examples demonstrate the capabilities of the spectrometer to acquire multi-frequency continuous wave spectra and frequency-swept spectra with dependency on the temperature and orientation of the sample, as well as the frequency rapid scan spectra.

Keywords

Electron-spin resonance, spectroscopy, spectrometer, magnetic resonance, development, instrument, experimental setup, prototype, terahertz beams, rapid scan, defects in crystals, qubit, silicon carbide, software, LabVIEW, simulation

Abstrakt

Spektroskopie elektronové spinové rezonance (také nazývaná elektronová paramagnetická rezonance nebo jen EPR) zahrnuje metody, které zkoumají hmotu prostřednictvím nepárových elektronů. Jednou z progresivních metod EPR je rychlé skenování, které umožňuje pozorovat kinetiku chemických reakcí. Kromě toho nedávný vývoj vysokofrekvenčních součástkách rozšířil použití vysokofrekvenční EPR (HFEPR), které využívají sub-terahertzové až terahertzové vlny. Tato práce se zabývá propojením obou cest do HFEPR spektrometru s prudkým skenováním frekvencí (FRaScan), který byl nedávno vyvinut na CEITEC VUT. Na začátku je stručně uvedena základní teorie k EPR, následovaný přehledem přístrojového vybavení pro HFEPR. V praktické části je popsáno technické řešení spektrometru. Důraz je kladen na implementaci softwaru, pomocí kterého je spektrometr ovládán a měření jsou automatizována. Následně jsou ukázány příklady z měření pevných látek, konkrétně karbidu křemíku dopovaného vanadem (SiC:V), ftalocyaninu líthia (LiPc) a krystalu 1,3-bisdifenylen-2-fenylallylu (BDPA). Příklady demonstrují schopnosti spektrometru získat multifrekvenční vlnově spojitá EPR spektra a frekvenčně rozmítaná spektra v závislosti na teplotě a orientaci vzorku, a taky spektra pomocí prudkého skenování frekvencí.

Klíčová slova

Elektronová spinová rezonance, spektroskopie, spektrometr, magnetická rezonance, vývoj, přístroj, měřící aparatura, prototyp, terahertzové vlny, prudký sken, defekty v krystalech, kvantové bity, karbid křemíku, software, LabVIEW, simulace

Bibliographic citation

ŠEDIVÝ, Matúš. *Realizace víceúčelového měřicího systému pro (sub)terahertzovou elektronovou spinovou rezonanční spektroskopii.* Brno, 2024. Dostupné také z: https://www.vut.cz/studenti/zav-prace/detail/159402. Dizertační práce. Vysoké učení technické v Brně, Fakulta elektrotechniky a komunikačních technologií, Ústav mikroelektroniky. Vedoucí práce Radimír Vrba.

Declaration

I declare that I am the author of the doctoral thesis “Implementation of a multipurpose measurement system for (sub)terahertz electron spin resonance spectroscopy” under the supervision of Prof. Radimír Vrba, Doc. Petr Neugebauer, and Oleksii Laguta, using specialized literature and other information sources, all of which are cited in this work and listed in the bibliography at the end of the work.

As the author of this dissertation, I further declare that in connection with the creation of this dissertation I have not infringed the copyrights of third parties, in particular, I have not infringed illegally on foreign personal rights, and I am fully aware of the consequences of violating Section § 11 and subsequent Copyright Act No. 121/2000 Coll., including possible criminal consequences arising from the provisions of Section § 152 the Criminal Code No. 140/1961 Coll.

Brno . . . .

author’s signature

Acknowledgement

I would like to express my sincere gratitude to my supervisor, prof. Radimír Vrba, for his support and patience with me. I also want to thank my co-supervisors doc. Petr Neugebauer and Dr. Oleksii Laguta, for their invaluable guidance and mentorship throughout the completion of this thesis. Their expertise, encouragement, and constructive feedback were instrumental in shaping the success of this work.

My deepest appreciation goes to my family, my parents, and my siblings, for their unwavering love and encouragement during my whole studies in the Faculty of Electrical Engineering and Communication at Brno University of Technology. I especially want to thank my wife Klárka. Her support provided the foundation for my perseverance, and I am grateful for the understanding and patience she demonstrated throughout this process.

I want to extend my gratitude to my colleagues at CEITEC BUT, namely Vinicius, Tonda, Janka, other Janka, Lenka, Jorge, Pawel, Jan, Ikram, Muhammad, Luboš, Arthur, Andriy and Oleh for their collaboration and teamwork. I am thankful for the positive and motivating work environment that we collectively created. I shall not forget to thank Dr. Roman Motiyenko and Prof. Joris Van Slageren for the internship in their research groups, where I learned about instrumentation used in terahertz spectroscopy and the HFEPR.

At the end I want to acknowledge the projects co-funding my Ph.D. study and research: First, THz Frequency Rapid Scan Electron Spin Resonance spectroscopy for spin dynamics investigations of bulk and surface materials (ERC Starting grant AN714850), next, Implementation of Frequency Rapid Scan Electron Spin Resonance Spectroscopy into Nuclear Magnetic Resonance Systems (GAČR EXPRO 21-20716X), then, Use of new knowledge from micro- and nanotechnology for complex electronic circuits and sensors (FEKT-S-17-3934) and New approaches in the use of modern micro- and nanoelectronics (FEKT-S-20-6215).

Contents

Introduction

Electron spin resonance (ESR) spectroscopy, also called electron paramagnetic resonance (EPR) or electron magnetic resonance (EMR) spectroscopy, allows studying materials with unpaired electrons. It is a technique similar to nuclear magnetic resonance (NMR), both are based on interaction of electromagnetic wave with magnetic dipole moment, but in EPR the origin of the magnetic dipole is the electron, not the nuclei. The EPR is a widely used technique in chemistry, biology, and physics where it provides information on the structure and dynamics of free radicals to understand the kinetics of chemical reactions, oxidation and reduction processes, catalysis, photosynthesis, enzyme reactions, the behavior of antioxidants, photochemical reactions, radiation effect on biological compounds, organic conductors, migration of electrical charge carriers and defects in materials [1]. Apart from basic research, there are several industrial applications of EPR. For example, packaging materials in the food industry are irradiated for sterilization. By measuring the specific radical concentration using EPR, it is possible to judge, the appropriate dose of radiation. Another example of industrial application is the monitoring of antioxidants in beer samples, which protects it from premature staling [2]. Besides these, there is significant progress in the research of medical applications similar to magnetic resonance imaging (MRI) called EPR imaging [3], which can be used also for non-living objects as batteries, to monitor redox reactions on its electrodes [4]. It is also a key method for research and development in spintronics [5, 6]. Examples of material research can be found in semiconductor materials based on silicon carbide, which can be used in photovoltaic cells, where EPR allows to study of their defects and impurities [7]. EPR can be also used in the investigation of thin film materials [8]. Pulsed EPR methods are mostly used to study the structure of biomolecules [9]. Finally, a high-frequency EPR technique is needed in the research of single molecular magnets [10].

EPR was first observed in 1944 by Evgeny Zavoisky on a sample of $MnSO_4$. He was focused to study of the physical and chemical impact of ultrashort waves on matter in laboratories of Kazan State University. His aim was to improve nuclear magnetic resonance experiments. However, his work was interrupted because of the Second World War. At the end of 1943, he changed his focus to electron spins. He measured the absorption coefficient of the radiofrequency field as a function of static magnetic field in solutions of manganese salts. Zavoisky demonstrated that the ratio of radio wave frequency and static magnetic field corresponding to the absorption maximum was constant. Moreover, it was in agreement with the expected value, of the energy difference of a magnetic dipole transition between quantum states of electron spins [11]. The reconstruction of Zavoisky's experimental setup is in Figure 1. Another pioneer in EPR was Brebis Bleaney who was looking for possibilities of using the recently developed microwave technology. His first EPR experiments were done in 1946 at the University of Oxford, unaware of Zavoisky's work. Results of these experiments showed that the broadening of spectral lines could be reduced by using cryogenic temperatures and dilution of samples [12].

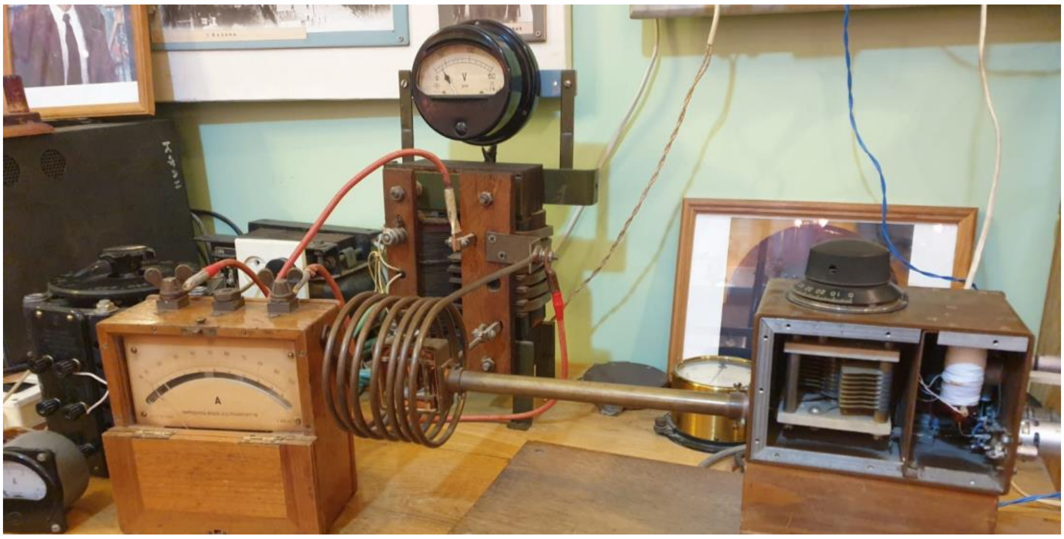

Figure 1: Reconstruction of EPR experimental setup in Evgeny Zavoisky Lab-Museum in Kazan. Photo made by Petr Neugebauer (11.03.2021).

During the second half of the 20th century, EPR spectroscopy significantly evolved, and the range of its applications has broadened from analytical and physical chemistry to biology and medicine. The technological advances allowed to the improve precision and sensitivity of EPR spectrometers and make a large variety of experimental setups. The first multi-frequency, high-frequency, and pulsed EPR spectrometers were developed [13, 14]. A few companies started to produce and sell EPR spectrometers (Bruker, Magnettech, JEOL). Although, even nowadays new ways for EPR spectroscopy are explored. One of the revolutionary approaches is EPR-on-a-chip (EPRoC) developed at the Institute of Smart Sensors at the University of Stuttgart. It focuses on the miniaturization and integration of EPR instrumentation in a single chip (excluding electromagnet), that to be mass-produced and consequently suitable for low-cost and portable EPR applications [15]. Electrically-detected magnetic resonance (EDMR) is another approach to conduct EPR by detection of changes in conductivity. This technique is more suitable for solid state materials for determination of intrinsic properties such as density and charge carrier mobility. Moreover, newer microwave technologies allowed the development of high-frequency spectrometers that can operate at higher frequencies of the sub-terahertz region and with a broader range. Another cutting-edge pathway in EPR spectroscopy is a rapid scan EPR – a revolutionary method developed by an Eaton group at the University of Denver. It significantly improves signal-to-noise ratio and decrease acquisition time [16]. Finaly, the EPR also drives further development in NMR via so called a dynamic nuclear polarization (DNP), that offers promising opportunities to significantly enhance NMR sensitivity and expand the capabilities of NMR spectroscopy.

1 Brief theory of the EPR

One of the quantum mechanics properties of elementary particles is a spin. It is an intrinsic form of angular momentum. For a single electron, the spin angular momentum *S* is equal to ½, and the spin quantum number m_s has a value ±½ (according to its orientation). The spin angular momentum is then ½ multiple of the reduced Planck constant $\hbar$. Because the electron is a particle that carries an electrical charge q, due to the spin, it behaves as a current loop which exhibits magnetic momentum called spin magnetic momentum μ_s that is proportional to spin angular momentum. Via gyromagnetic ratio γ we can calculate the spin magnetic momentum of a free electron

$$\mu_{\boldsymbol{s}} = \gamma\hbar\boldsymbol{S} = g\frac{q}{2m_e}\hbar\boldsymbol{S} = -g_e\beta_e\boldsymbol{S} \ \ [\mathrm{J\cdot T^{-1}}], \tag{1}$$

where m_e is the mass of electron $9.1094\cdot10^{-31}$ kg, q is elementary charge $1.6022\cdot10^{-19}$ C, β_e is Bohr magneton whose value is $9.274\cdot10^{-24}$ $\mathrm{J\cdot T^{-1}}$, and g_e is a dimensionless parameter called g-factor of a free electron and its value is about 2.0023 [17].

In many chemical compounds, electrons are paired, and the net spin moment is zero. As a result, they do not react to external magnetic field. In materials that contain unpaired electrons (paramagnetic centers), spin magnetic moments have randomly distributed orientations and cancel each other because of heat (k_bT, where k_b is Boltzmann constant $1.381\cdot10^{-23}$ $\mathrm{J\cdot K^{-1}}$, and T is absolute temperature). Such material is called paramagnetic and without an external magnetic field, both spin orientations (½ and -½) share the same energy level (energy levels are degenerated). However, in the presence of a static external magnetic field, spin magnetic moments tend to orient parallel to the direction of the external field B_0 because it is energetically favorable (and less favorable in antiparallel direction) in terms of their potential energy. Under the influence of the magnetic field, the energy levels for both spin orientations (½ and -½) split, which is called the **Zeeman effect**, as shown in Figure 2. A shift from degenerated energy level for each orientation is defined as:

$$E = m_s g\beta_e B_0 \ \ [\mathrm{J}], \tag{2}$$

then the difference between energy levels is:

$$\Delta E = \frac{1}{2}g\beta_e B_0 - \left(-\frac{1}{2}g\beta_e B_0\right) = g\beta_e B_0 \ \ [\mathrm{J}], \tag{3}$$

where B_0 is the external magnetic field (also called a flux density or induction) and g is a factor which in most materials slightly differs from g_e because of contributions such as spin-orbital coupling and thus is characteristic for each paramagnetic species. It is obvious that two spin states have the same energy if there is no external magnetic field. On the other hand, energy difference depends linearly on the magnetic field [17, 18].

By applying radiation with the magnetic component B_1 perpendicular to the static magnetic field, which energy of photons meets the energy difference between different spin states, causing the electron spin resonance. A fundamental equation that expresses a resonance condition in electron paramagnetic resonance spectroscopy is:

$$hf = g\beta_e B_0 \ \text{[J]} \tag{4}$$

where *hf* is the energy of the photon (*h* – Planck constant, *f* – frequency).

Meeting this condition will cause an absorption of radiation that can be interpreted as the intensity of a spectral line. The effect is even more significant in low temperatures due to higher differences in the Boltzmann population of states. The intensity of the spectral line also depends on the total amount of paramagnetic centers. However, too high a concentration may cause a broadening of spectral lines. Another way to achieve electron spin resonance is by applying microwave radiation of constant frequency and adjusting the magnetic field. This approach is technically easier to achieve, by simply changing electrical current through a coil [19]. Technical aspects of EPR spectrometers will be discussed later in section 1.2.

If an atom with non-zero nuclear spin is present near the paramagnetic center, so-called hyperfine splitting of energy levels effectively occurs. It arises from the interaction between electronic spin *S* and nuclear spin *I*. A simple example can be presented on a single hydrogen atom (hydrogen molecule has paired electrons). It has one valence electron with spin S= ½ and a single proton also gives nuclear spin I= ½ (deuterium has I= 1). Without an external magnetic field, both electron spin states (m_S= ±½) share the same energy level. However, in the magnetic field, sublevel m_S= +½ is going up, and sublevel m_S= -½ is going down. At each sublevel, electron spin interacts with both nuclear spin states (m_I= ±½) giving four energy sublevels. Their energy can be calculated by equation:

$$E = m_S g\beta B + A m_S m_I \tag{5}$$

where m_I is the nuclear quantum spin number, and *A* is a hyperfine coupling constant.

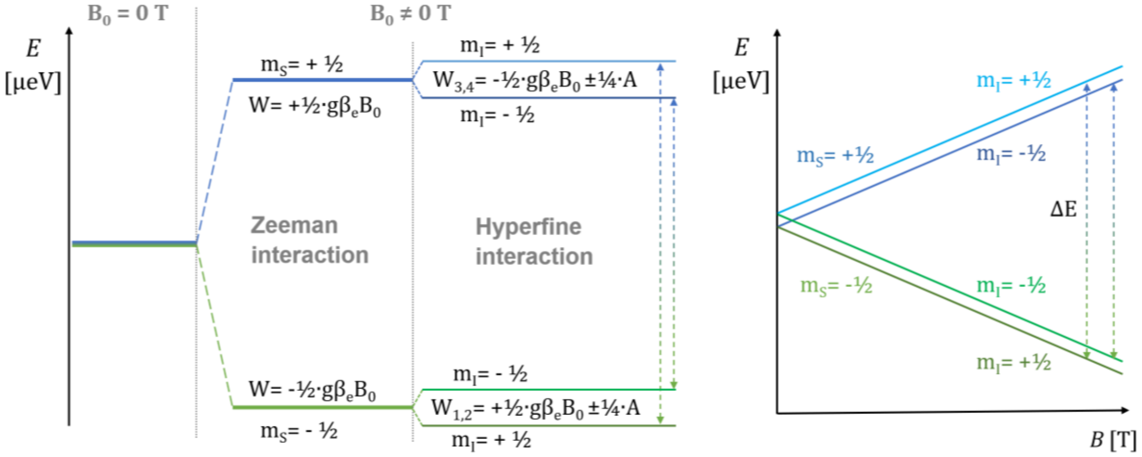

Figure 2: Splitting of energy levels and allowed EPR transitions between them in static magnetic field (left) and linearly varying magnetic field (right) for a hydrogen example.

For clarification, Figure 2 contains a diagram of energy level splitting and allowed EPR transitions (selection rule: $m_s = \pm 1$, $m_I = 0$) in the constant and the varying magnetic field. Because only two transitions are allowed, an EPR spectrum would contain two lines separated by $A \approx 1417$ MHz [20]. The nearer paramagnetic center and nuclei are a stronger hyperfine coupling can be expected. For cases of multiple equivalent nuclei n_i, or when nuclear spin is more than ½ ($I = 1, 3/2, 2\ldots$), the number of possible spin transitions will be:

$$N_t = 2 \cdot n_i \cdot I + 1 \tag{6}$$

If $n_i > 1$, intensity ratio follows Pascal triangle (1, 1:1, 1:2:1, 1:3:3:1, ...).

1.1 Mathematical description of electron spin resonance phenomenon

As was shown in the previous section, various interactions with electron spin increase the complexity of a spin system. Some spin systems can be so complex that it is difficult to make a full quantum-mechanical description of the electron-spin-resonance event. To simulate EPR spectra, the concept of an **effective spin Hamiltonian** is used for the description of spin interactions as well as for the system reaction to the external magnetic field. However, the spin Hamiltonian model may not be valid for cases with large spin-orbital coupling or samples in the gas phase. The spin Hamiltonian operator relates to the total energy of a spin system and consists of sums of interaction terms:

$$\hat{H} = \sum_i (\hat{H}_{ez,i} + \hat{H}_{zf,i}) + \sum_{i,j} \hat{H}_{ss,ij} + \sum_{i,k} \hat{H}_{hf,ik} + \sum_k (\hat{H}_{nz,i} + \hat{H}_{nq,i}). \tag{7}$$

for example, $\hat{H}_{ez}$ is a term for electron Zeeman interaction:

$$\hat{H}_{ez} = \beta \boldsymbol{B}^T \tilde{\boldsymbol{g}} \hat{\boldsymbol{S}} = \beta \left(g_{xx} B_x \hat{S}_x + g_{yy} B_y \hat{S}_y + g_{zz} B_z \hat{S}_z \right). \tag{8}$$

Other terms express Hamiltonian components for: zero-field splitting H_{zf}, spin-spin interaction H_{ss}, hyperfine splitting H_{hf}, nuclear Zeeman interaction H_{nz} and H_{nq} is the nuclear electric quadrupole.

$$\hat{H}_{zf} = \hat{\boldsymbol{S}}^T \boldsymbol{D} \hat{\boldsymbol{S}}\,, \qquad \hat{H}_{ss} = \hat{\boldsymbol{S}}_1^T \boldsymbol{J} \hat{\boldsymbol{S}}_2, \qquad \hat{H}_{hf} = \hat{\boldsymbol{S}}^T \boldsymbol{A} \hat{\boldsymbol{I}}, \qquad \hat{H}_{nq} = \hat{\boldsymbol{I}}^T \boldsymbol{Q} \hat{\boldsymbol{I}}. \tag{9}$$

Here $\hat{\boldsymbol{S}}$ is an operator of the electron spin, $\tilde{\boldsymbol{I}}$ is an operator of the nuclear spin, $\boldsymbol{J}$ is a coupling matrix, $\boldsymbol{D}$ is the zero-field tensor, $\boldsymbol{Q}$ is the traceless nuclear quadrupole tensor and $\boldsymbol{A}$ is the hyperfine coupling matrix. Calculation of total spin Hamiltonian might be very demanding. However, in some cases, it is possible to neglect some terms or use symmetry of matrixes. Further explanation of spin Hamiltonian can be found in the literature [17, 21, 22].

The reaction of a material to an applied magnetic field is described by its **magnetization**, which is a vector that represents the volume density of oriented magnetic dipole moments. In EPR spectroscopy, a component of magnetization along the axis of the static external magnetic field is related to the size of the spectral line. From the classical point of view, magnetization can be expressed by the equation:

$$\boldsymbol{M} = \frac{\boldsymbol{B}}{\mu_0} - \boldsymbol{H} = \mu_r\boldsymbol{H} - \boldsymbol{H} = (\mu_r - 1)\boldsymbol{H} = \chi\mathbf{H}\ [\mathrm{A \cdot m^{-1}}]. \tag{10}$$

where $\boldsymbol{H}$ is a vector of the magnetic field intensity, μ_r is the permeability of vacuum, μ_r is relative permeability and χ is the magnetic susceptibility of a material. Alternatively, magnetization can be expressed as a collection of N dipoles in a given volume V which results in a macroscopic moment:

$$\boldsymbol{M} = \frac{1}{V}\sum_{i=1}^{N}\boldsymbol{\mu}_i = \frac{d\boldsymbol{\mu}}{dV}\ [\mathrm{J \cdot T^{-1} m^{-3}}], \tag{11}$$

where $d\boldsymbol{\mu}$ is the elementary magnetic dipole moment and dV is a volume element. As the magnetization reflects a bulk response of a large number of spins, it can hide the detailed behavior of single spins but also allows to avoid a quantum mechanical treatment of the resonance phenomenon [17].

As mentioned above, if paramagnetic material is in the external magnetic field, energy levels for spin states -½ and +½ will split, and their energy difference is linearly proportional to the magnetic field. Because the potential energy for the spin states pointing antiparallel to the magnetic field is lower (in the case of the electron), we can expect a higher density of states at this energy level for thermodynamic equilibrium. According to Boltzmann distribution, the ratio between these states will be:

$$\frac{N_u}{N_l} = \exp\left(-\frac{\Delta E}{\mathrm{k_b} T_s}\right) = \exp\left(-\frac{g\beta_e B_0}{\mathrm{k_b} T_s}\right), \tag{12}$$

Where N_u and N_l are respectively the density of states in the upper and lower levels, ΔE is the energy difference of levels (3), $\mathrm{k_b}$ is a Boltzmann constant ($1.3806\cdot10^{-23}$ $\mathrm{J\cdot K^{-1}}$), and T_s is a parameter called spin temperature, that may be considered equal to surrounding temperature in case of thermodynamic equilibrium. In practice, this means that at room temperature the difference between states at the upper and lower level is usually very small. However, it will increase with lower temperature, which will reduce spontaneous transitions. Also, at the higher magnetic field, the ΔE will linearly increase. And that will consequently result in better sensitivity.

Radiation that meets the EPR condition by equation (4) will cause an excitation/transition of states from the lower level to the upper level. This leads to a change in the population of both energy levels and to distortion of thermodynamic equilibrium. The population change (caused by the absorption of photons) is proportional to the power of the radiation. Electron spins that are excited to higher energy levels tend to return to the state with lower potential energy by losing energy to the surroundings (by phonons and photons), to achieve thermodynamic equilibrium. This process is called spin relaxation. A loss of an excess energy follows an exponential decay:

$$\delta E = \delta E_0 \exp\left(-\frac{t-t_0}{\tau}\right), \tag{13}$$

where δE_0 is an excess energy at time t_0, and τ is the characteristic time for energy flow from the spin system into surroundings and is related to the mean lifetime of a given spin-orientation state (see Figure 3) [17]. If the power of the radiation is too large or the relaxation time is too long, the relaxation does not keep up, and the spin package/ensemble is saturated. Then, the change in population of energy levels is no longer proportional to radiation power.

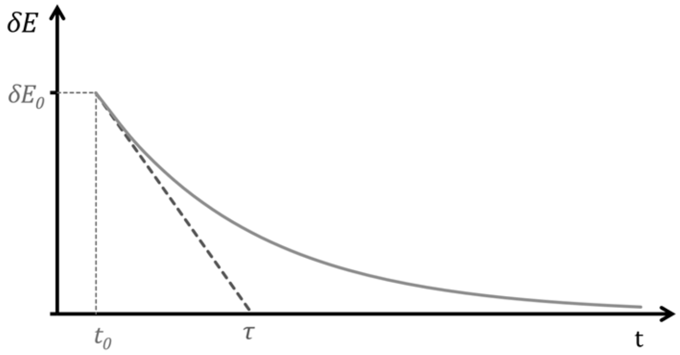

Figure 3: Exponential decay of excess energy.

Because the magnetization ***M*** along the externally applied magnetic field is proportional to the population difference in spin states, it is possible to use a macroscopic model of the spin relaxation to describe the time dependence of total spin magnetization vector ***M***. This mathematical tool is called **Bloch equations**. It is useful for the interpretation of the magnetic-resonance phenomenon in terms of vectors and torques, which helps to understand the effect of microwave pulses. It also simplifies the complexity of spin interaction with surroundings by using relaxation times τ_1 and τ_2 as empirical parameters. Explanation of absorption and dispersion concepts can also be obtained by the Bloch equations. They omit the quantum-mechanical behavior of individual spins without loss of generality. A form of the Bloch equations that consider the response of magnetization to sudden change of homogenous magnetic field is

$$\frac{dM_x}{dt} = \gamma_e B M_y - \frac{M_x}{\tau_2} \tag{14}$$

$$\frac{dM_y}{dt} = -\gamma_e B M_x - \frac{M_y}{\tau_2} \tag{15}$$

$$\frac{dM_z}{dt} = \frac{M_z^0 - M_z}{\tau_1} \quad . \tag{16}$$

Here indexes are used for individual components of magnetization vector ***M***, γ_e is the gyromagnetic ratio, τ_1 is (spin-lattice) relaxation time for longitudinal and τ_2 is (spin-spin) relaxation time for transversal components of ***M***. Irradiating by microwaves is equivalent to applying of an oscillating field $\boldsymbol{B_1}$ that in the case of EPR, corresponds to the magnetic component of radiation. Adding the oscillating field into Bloch equations will result in

$$\frac{dM_x}{dt} = \gamma_e\left(B_0 M_y - B_1 M_z \sin \omega t\right) - \frac{M_x}{\tau_2}, \tag{17}$$

$$\frac{dM_y}{dt} = \gamma_e(B_1 M_z \cos \omega t - B M_x) - \frac{M_y}{\tau_2}, \tag{18}$$

$$\frac{dM_z}{dt} = \gamma_e(B_1 M_x \sin \omega t - B_1 M_x \cos \omega t) + \frac{M_z^0 - M_z}{\tau_1}, \tag{19}$$

where ω is an angular frequency of oscillating magnetic field B_1. A more detailed explanation of Bloch equations, the concept of a rotating frame which simplifies their notation as well as their steady-state solution can be found in literature [17, 22, 23].

1.2 General EPR instrumentation

The progress in EPR spectroscopy is tied to the development of electronic components, materials, and fabrication technologies necessary for the assembly of a spectrometer. In this section, the main functional parts of EPR spectrometers will be described. The diagram in Figure 5 presents all the main parts of a usual continuous wave (CW) spectrometer. Continuous wave means that the sample is continuously irradiated by microwaves (m.w.) during the whole measurement. Another type is the pulse EPR spectrometer, which will be briefly introduced later. CW spectrometers are further categorized by the microwave band of their operation. A list of microwave bands used in EPR spectroscopy can be found in Table 1. These are no random frequencies but lay in the middle of so-called communication windows, in which absorption of microwaves by molecules in the air is the lowest (see Figure 4) [24].

Table 1: Field of resonance (B_{res}) for a g = 2 at chosen microwave frequencies [21]

Microwave band	Frequency [GHz]	Resonance field B_{RES} [T]
L	~ 1.1	0.0392
S	~ 3	0.1070
X	~ 9.5	0.3389
Q	~35	1.2485
W	~90	3.2152
J	~270	9.6458

Most EPR spectrometers operate in the X and Q band region because the magnetic field required for resonance is simply achievable by conventional electromagnets [25]. If the superconducting magnet is required, we are talking about a high frequency or high field (HFEPR) spectrometer. They usually use microwave radiation in the W band or above. More information on HFEPR spectrometers is revealed in the second chapter.

The main parts of the CW-EPR spectrometer are:

- **Microwave bridge** that includes a microwave source, waveguides, circulator, resonance cavity, and detector.
- **Electromagnets** with their power supply unit (and cooling system), Tesla meter (or Gauss meter).
- Finally, a **modulation circuit** that significantly improves the signal-to-noise ratio (SNR) by using a lock-in amplifier for phase-sensitive detection (PSD).

Of course, experiments are usually controlled by a PC which also serves for processing, analysis, and storing of measured data [19].

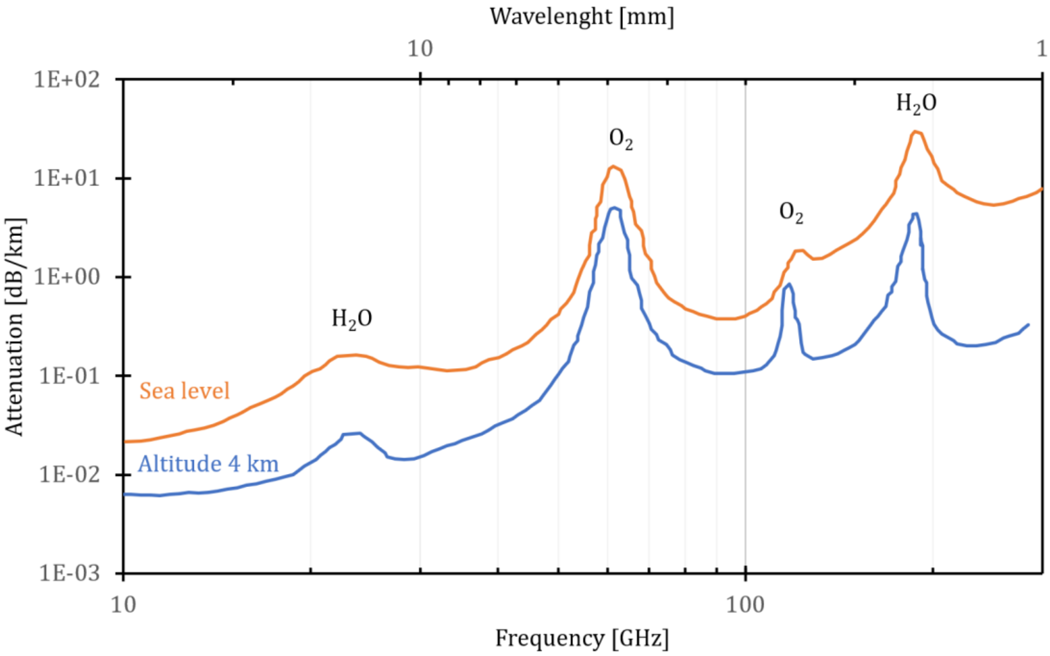

Figure 4: Atmospheric attenuation of microwaves in 10-300 GHz range. Curves were digitized from [24].

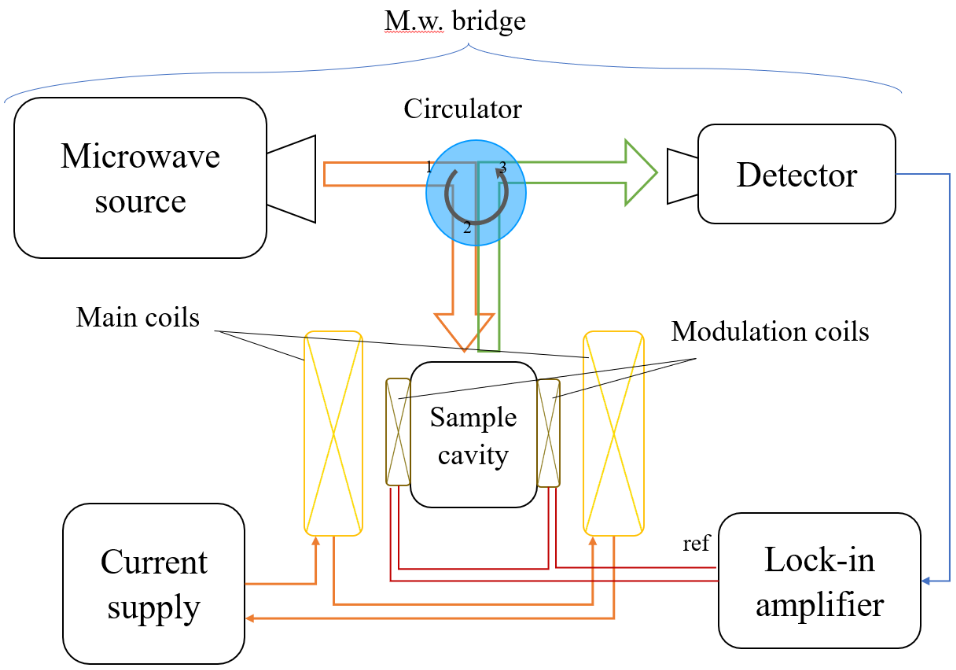

Figure 5: Functional diagram of ordinary continuous wave (CW) ESR spectrometer

The microwave bridge is a group of components that takes care of the generation, propagation, and detection of microwaves. As a source of microwaves, vacuum tubes called klystrons were commonly used in the past. Modern spectrometers mostly use sources based on solid-state electronics because of their small size, sufficient power, tunability, long life, and relatively low cost. Their disadvantages to vacuum tubes are higher white noise which is typical for a solid-state electronics and jitter that needs to be compensated by a phase-lock loop (PLL) to a reference signal. Other considerable sources of microwaves for EPR spectroscopy are YIG sphere, impact ionization avalanche transit-time (IMPATT) diode, backward wave oscillator (BWO), Oroton, and gyrotron [26]. Microwaves that enter the circulator (shown in Figure 5) at port 1, are transferred out through port 2 to the resonance cavity. When they return to the circulator through port 2, they are diverted to leave the circulator through port 3 to the detector, not back to the source. Waveguides are essentially rectangular metal tubes that serve to deliver microwaves from the source to the resonance cavity with a sample. Their dimensions determine modes and cut-off frequency that can be propagated through them[27]. A resonance cavity is usually just a metal box of cylindrical or rectangular shape in which the studied sample is placed. Resonance cavities are able to store microwave energy at a specific frequency, therefore no microwaves are reflected back. Electrical currents that are generated in its walls by microwaves result in heat losses. Along with resonance frequency, another important attribute of the cavity is quality factor Q which is expressed:

$$Q = \frac{2\pi \cdot (Energy\ stored)}{Energy\ disipated\ per\ cycle}\ [-] \qquad \text{or} \qquad Q = \frac{f_{res}}{\Delta f}\ [-]; \qquad (20)$$

where f_{res} is the resonance frequency and Δf is the bandwidth of the resonance cavity. Bandwidth can be easily estimated as a difference of frequencies at which reflected power decreases by half, or more exactly by -3 dB.

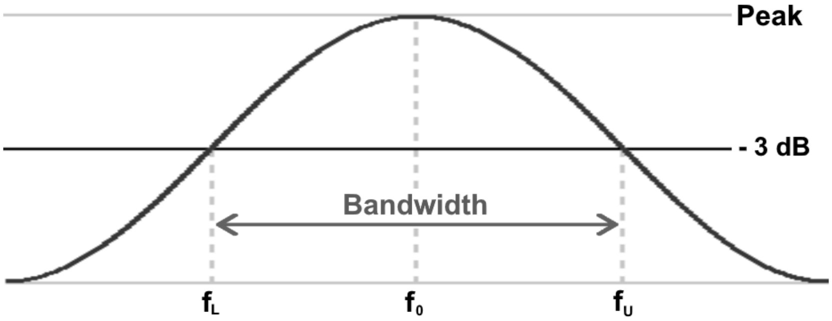

Figure 6: Illustration explaining definition of a bandwidth. Applicable also for a spectral line width (full width at half maximum - FWHM).

The resonance of the cavity causes a standing wave, that has magnetic and electric components exactly out of phase. Cavities are designed in such a way that the sample is placed on the spot where the amplitude of the magnetic field is maximum, and the electric field has its minimum (nodes). This reduces dielectric losses in a sample caused by an alternating electric field. Between the cavity and waveguide is an adjustable aperture called an iris. The function of the iris is to arrange impedance matching of the cavity with the waveguide. When the external magnetic field meets the condition for EPR at a given frequency, the sample absorbs microwave power which leads to a drop in Q factor and thus a change of cavity impedance. Therefore, part of microwave power is reflected back to a circulator and therefore to a detector [19]. As the detector of microwaves usually a properly pre-biased Schottky diode is used. The diode converts the power of microwave radiation to current. Without biasing, the diode would not operate in the linear region, but its current would be proportional to the square of microwave power. Modern integrated detectors have a feature of automated biasing [28].

The maximum achievable magnetic field is determined by the design of an electromagnet. An electromagnet may consist of a single solenoid, but more often is made of two identical coils, whose distance is the same as their middle radius. This arrangement is called a Helmholtz coil, in which center there is a homogenous magnetic field. The intensity of the produced magnetic field is proportional to the product of the electrical current and the number of turns. However, the inductance of a coil is proportional to the square of the number of turns. Therefore, the wiring of coils usually consists of several hundred turns and can sustain a few tens of amperes. For high-performance coils, isolated copper stripes are a good choice because they make full use of available space and have a good distribution of heat. Because a high current will cause high heating of the coil, there is a heatsink, sometimes bigger than the coil itself. Some electromagnets also use a cooling water circuit. To ensure that the same electrical current runs through both coils of the electromagnet, they need to be connected in series. Parallel connection may be an option if coils have so many turns that the resistance of their wiring is much higher than the output impedance of a power supply. The power supply for the electromagnet has to be chosen concerning the parameters of the coils. If their resistance is low, the power supply should be able to deliver a high current, but the voltage does not have to be so high. In many spectrometers, the amount of output current from the power supply follows a control signal (negative feedback), generated in a control unit. A good control unit also compensates nonlinearities of the electromagnet. To do this, the magnetic field is measured by a Teslameter with a Hall probe, that is connected to the control unit [19]. Some power supplies may have their own control unit and communication interface, so they can be controlled remotely by a computer.

The last important piece in a CW-EPR spectrometer is a phase-sensitive detection (PSD). Although this feature is not always essential for the function of the spectrometer, it significantly improves the quality of the EPR signal in terms of signal-to-noise ratio (SNR). An instrument that is used for PSD is called a lock-in amplifier. The basic principle of PSD in EPR is as follows: the magnetic field is slightly modulated by a sine signal at a reference frequency that is usually between 1–100 kHz. A higher frequency could cause unwanted heating of samples. A signal generator or a lock-in amplifier itself can provide the reference signal. This signal is amplified in an audio amplifier and subsequently is brought to the modulation coil (usually solenoid or Helmholtz coil).

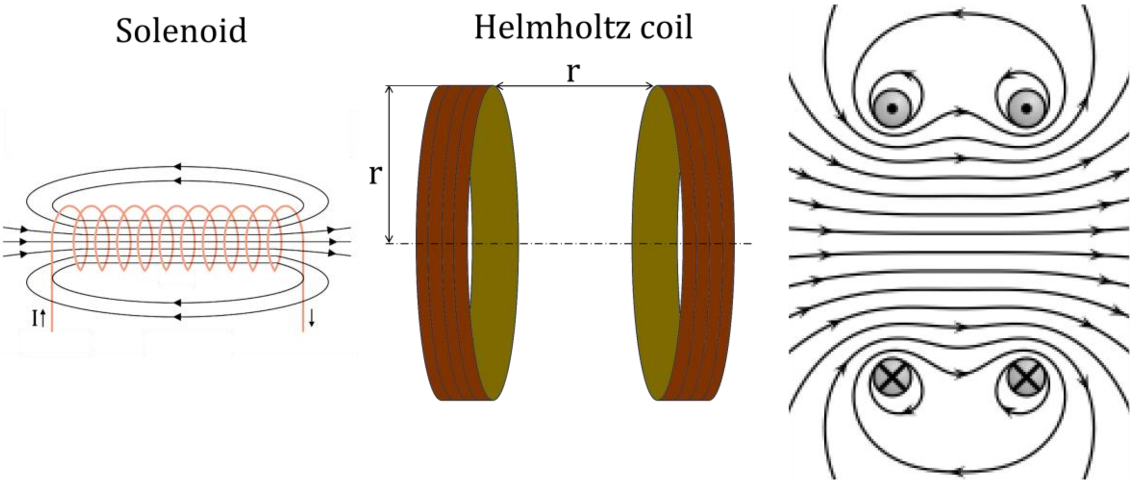

Figure 7: Solenoid (left) and Helmholtz coil (right) with homogenous magnetic field in its center. Distance between two coils equals their radius.

The amplifier should have low harmonic distortion and be powerful enough to adjust the amplitude of the magnetic field up to a few tens of Gauss (1 G = 0.1 mT). Applying modulation while sweeping of magnetic field will result in changes in reflected microwave power when absorption caused by EPR occurs. These changes will have the same frequency as the frequency of modulation. The amplitude of the detected signal will be proportional to the product of modulating field amplitude and slope of absorption peak as it is shown in Figure 8. In fact, the resulting EPR signal has the shape of the first derivative of the absorption line, amplitude-modulated on carrier signal with the same frequency as the reference signal (see Figure 8). In simple cases, the line width (FWHM) can be then determined as the distance between positive and negative maximum peaks. Finally, this signal is brought to the lock-in amplifier, where it is mixed with the reference signal. Mixing of two harmonic signals will create two components. One frequency will be the sum of these signals' frequency and another of their difference. But, because the EPR signal has the same frequency as the reference signal, the second component will result in a DC signal with amplitude:

$$\mathrm{V}_{psd} = \frac{1}{2} V_{sig} V_{ref} \cos\left(\varphi_{sig} - \varphi_{ref}\right). \tag{21}$$

Here *V* is a voltage amplitude, φ is a phase, suffix *sig* is used for the signal from detector and *ref* is used for the reference signal. In lock-in amplifier, this mixing is done twice. Second time is signal from detector mixed with 90° (π/2) shifted reference signal to prevent the case, when phase difference is zero. By applying a low pass filter, the higher frequency components are removed. If the two remaining DC signals are geometrically summed, their result is a recovered EPR signal. In digital lock-in amplifiers, this signal is directly recorded and sent to a computer for processing into EPR spectrum [29].

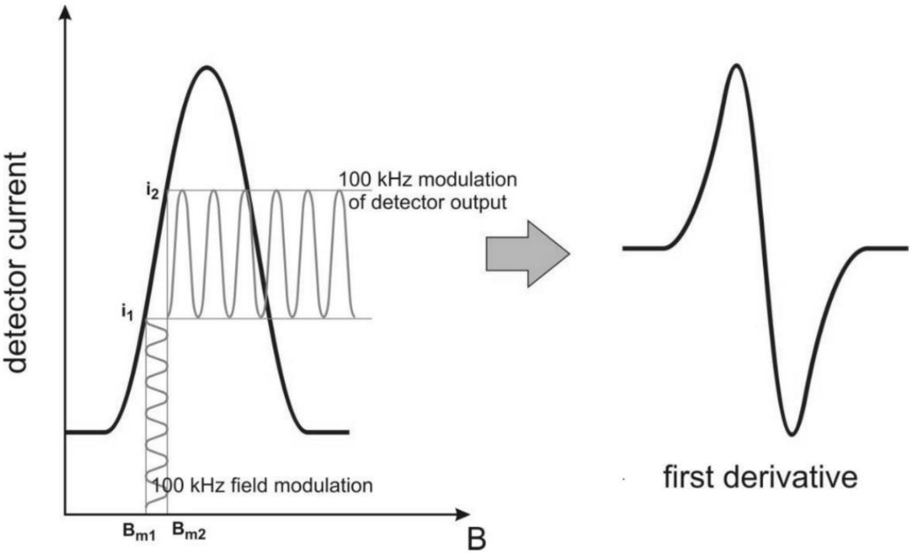

Figure 8: Effect of modulation on absorption EPR spectral line. Taken from [25]

Three examples of EPR spectra are provided in Figure 9. Just from the shape of the spectra, some properties of the samples can be assumed. For example, it is obvious that in human hair there is only one type of paramagnetic center in the examined area. In vitamin C, there is a nucleus with spin I = 1/2 near the unpaired electron, which causes hyperfine splitting. In vitamin E, there are many sources of hyperfine splitting, and some lines could be too close to be clearly distinguished. Measurement at higher field and frequency could help in this case by providing results with higher spectral resolution [21].

Figure 9: Examples of various EPR spectra of ordinary things. Taken from [2].

In Figure 10, there is a photo of an actual X-band spectrometer. This spectrometer was designed to operate also in the Q-band, however, a current source is not powerful enough to reach the required magnetic field. On the left of the photo is the power supply for the electromagnet, on which the top is placed a frequency counter that is connected to the microwave bridge and displays the actual frequency of microwaves. Next to the power supply is an electromagnet. Inside of two cylinders are hidden coils with a heatsink and water-cooling system. On top of the electromagnet are two benches. The left one carries a microwave bridge, equipped with a microwave splitter, circulator, a few waveguides, a gun diode as the source of microwaves, and a Schottky diode as the detector. The microwave bridge is connected to the microwave controller whose task is to measure the output power of the microwave source and proper biasing of the detector. The above microwave controller is an EPR control unit that contains a source of the reference signal and amplifier for modulation, a lock-in amplifier for demodulation, and a regulator of the magnetic field. A Teslameter is used for feedback to the magnetic field regulator. The EPR control unit is connected to the computer by a serial port. In a computer, measured data is processed, plotted in a graph, and analyzed by scientists in various ways.

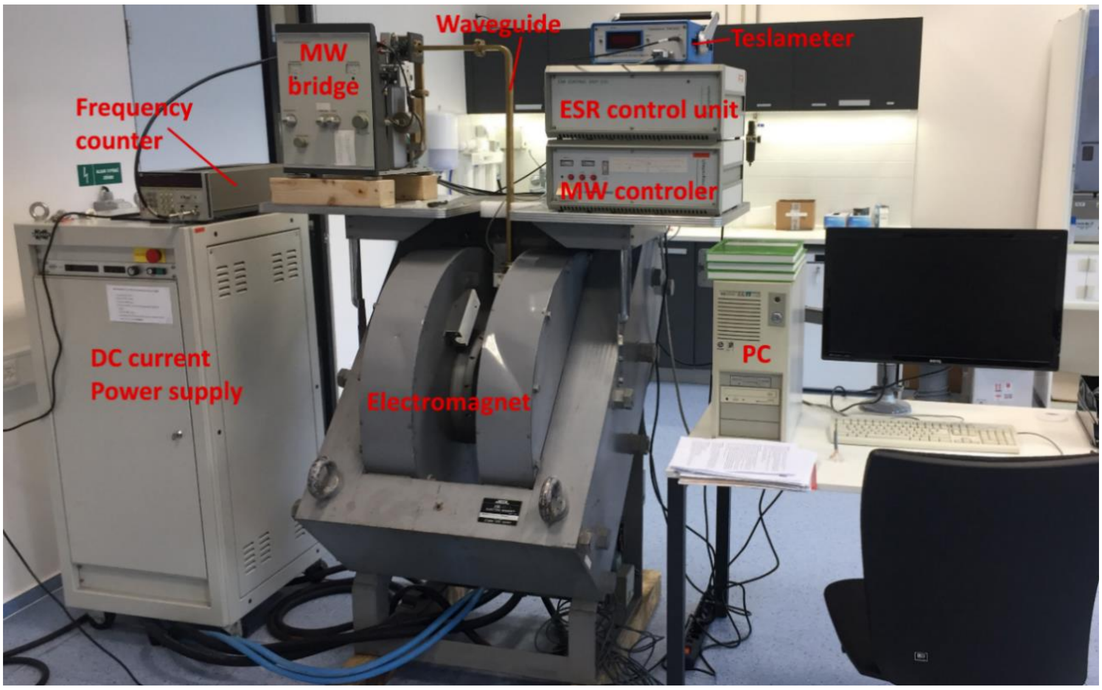

Figure 10: X-band EPR spectrometer in laboratory of EPR spectroscopy at CEITEC BUT.

1.3 Pulse EPR spectroscopy

Similarly, as in NMR, pulsed EPR experiments are currently preferred in the biological research field [30, 31]. They can decouple certain interactions to spotlight only desired ones which allows to access information that cannot be obtained by the CW-EPR. However, it is more expensive and technologically challenging. In some cases, the pulse EPR experiments can take longer than the CW-EPR. One of the capabilities of pulsed

EPR is looking at spin systems via probing of spin-lattice (longitudinal) relaxation time τ_1 and spin-spin (transverse) relaxation time τ_2. The τ_1 quantifies the rate at which the magnetization component parallel to the magnetic field returns to its equilibrium after the pulse is applied. It is related to the transfer of energy from the spin system to neighboring atoms and molecules through spin-orbit coupling. The τ_2 then quantifies the rate at which the component of magnetization in the plane perpendicular to the magnetic field decays and spin orientations become randomized (see Bloch equations at page 9). The idea is to probe spin systems via their magnetization response to a short but strong microwave pulse (~10 ns, ~100 W). The pulse will excite transitions in a spin system at multiple resonance frequencies at once. The spin system then relaxes to equilibrium while generating a free induction decay (FID) signal (exponentially decaying oscillations of magnetization). In standard pulsed EPR measurements, sequences of pulses are applied and responses in the form of electron spin echoes (two mirrored FIDs) are recorded and usually Fourier-transformed into frequency spectra [32]. Various pulse sequences are summarized in Figure 11.

When hyperfine and quadrupole splitting is too small and cannot be resolved in CW-EPR spectra, because of the line broadening, the electron-spin echo envelope modulation (ESEEM) can be used to recover this information by measuring the nuclear frequencies. here are several ESEEM methods, that can be sorted by the number of microwave pulses. The two-pulse method is simple and fast; however, the spectrum also contains the sum and difference of the basic nuclear frequencies, and several drawbacks such as sensitivity to experimental conditions, lower SNR, and lack of accessible information, may limit its use. The first microwave pulse will flip the magnetization vector by 90° ($\pi/2$) into the Z-plain. During the time between pulses, individual spins will diverge. Another pulse (180° or π) will cause spins to converge together again. This pulse can be either twice as long or double in power as the first pulse. After the same time interval that has passed between the pulses, spins will be oriented in the same direction and the echo signal will reach its maximum. The signal from this point further is called a free induction decay (FID)[23]. In the three-pulse method the first two $\pi/2$-pulses separated by the τ, create nuclear coherences and the third $\pi/2$-pulse leads to the formation of spin-echo. Obtaining the spectrum by the three-pulse method is more time-consuming, however, the spectrum is simpler and with narrower lines. Anyway, it is still a one-dimensional experiment in which an overlap of signals occurs. Hyperfine Sublevel Correlation Spectroscopy (HYSCORE) is based on three-pulse ESEEM, with π-pulse inserted before the last $\pi/2$-pulse. The π-pulse is separated from other pulses with two-time intervals (t_1 and t_2), which can be varied. That makes it a two-dimensional experiment, in which the echo intensity is recorded as a function of time between pulses t_1 (first dimension) and t_2 (second dimension). The time domain spectra are transformed to the frequency domain via 2D Fourier transformation. [33, 34]

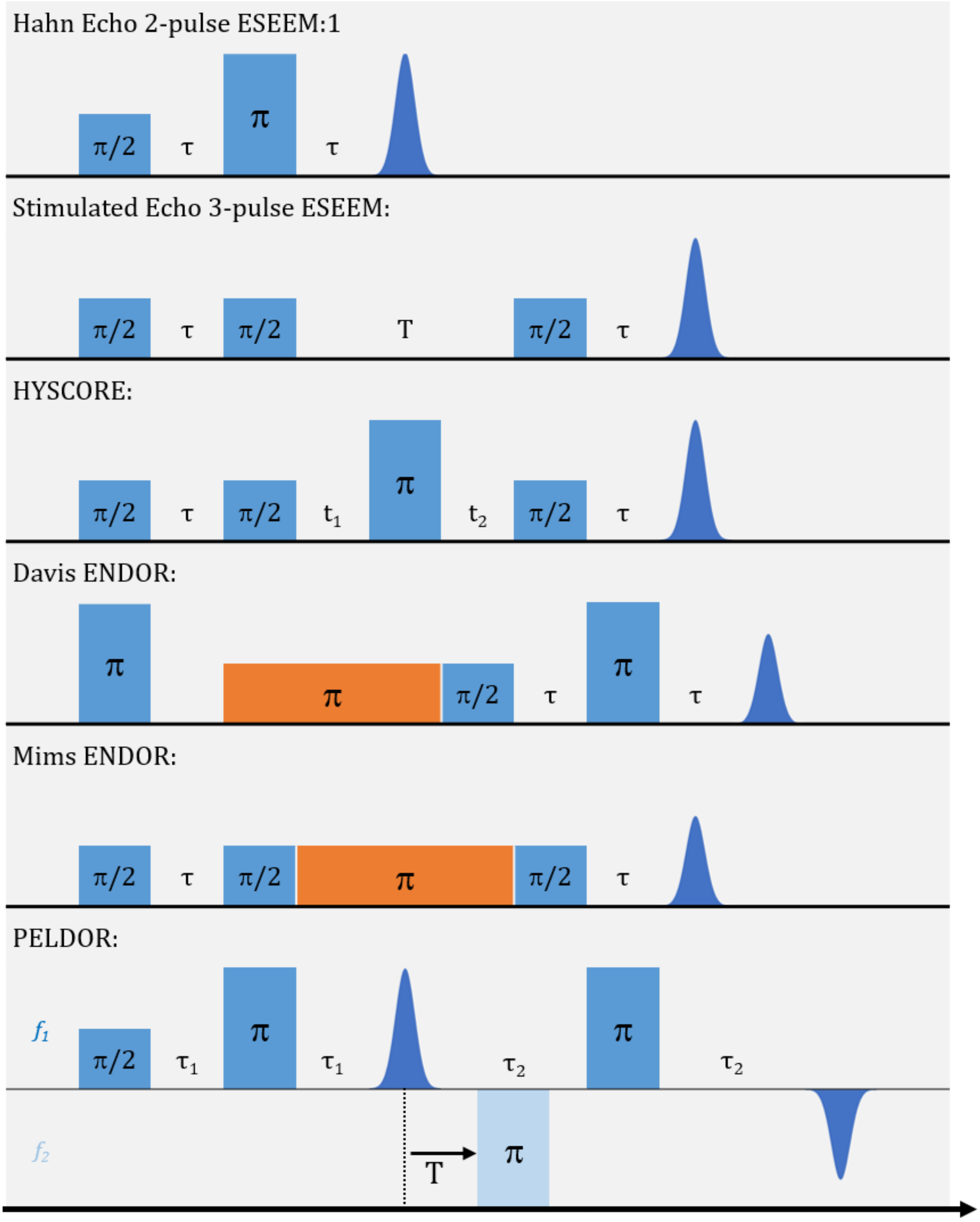

Figure 11: Pulse sequences of various type of experiments. Blue and orange color denotes microwave (EPR) and radio wave (NMR) pulses respectively. Inspired by [31]

Another pulsed EPR method that clarifies hyperfine coupling of unpaired electrons with surrounding nuclei is an electron-nuclear double resonance (ENDOR) which is a complementary method to ESEEM. This information can be used to indirectly determine the distances and orientation (spatial distribution) of nuclei in the vicinity of the unpaired electrons. While CW ENDOR also exists, the pulsed ENDOR provides insight into the relaxation times of the system, has better resolution, and allows observation of weakly coupled nuclei. It is also less prone to artifacts and does not require adjusting RF power to relaxation times such as the CW technique. Figure 12 depicts the processing of ENDOR signals. There is also a technique called pulsed electron-electron double resonance (PELDOR), also known as double electron-electron resonance (DEER), that excites two paramagnetic centers at different frequencies and observes electron-electron spin-spin coupling [23]. Depending on a sample type, the PELDOR can be sensitive to distances up to about 10 nm, which makes it a suitable tool for studying of topology of large protein complexes.

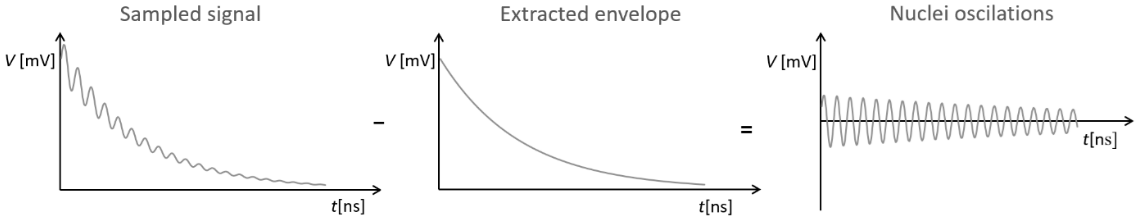

Figure 12: Signals in pulsed ENDOR experiment.

While pulsed EPR can deliver new information that is hard or not even possible to obtain via CW-EPR, it is also technically more demanding. First, a powerful microwave source is necessary. This source must be able to create extremely short pulses that are about 10 ns long, with up to 1 kW of microwave power, and about 1 μs repetition time. This leads to several modifications of the microwave bridge. The first one is a microwave-forming unit (MWFU) that produces low-power pulses. A key element for the creation of short pulses is a PIN diode switch, that is controlled by biasing voltage. Another important component is a microwave amplifier. Commonly a trawling wave tube (TWT) is used to amplify short low power pulses. Finally, an attenuator is used to adjust an output power and consequently the excitation field B_1. The Q factor of the resonance cavity has to be significantly lower (<500), in order to achieve a broader frequency band and a shorter ring-down time that leads to faster dissipation of high-power pulse. But then, a detected echo signal is very low, therefore it has to go through a preamplifier. This preamplifier has to be protected by another PIN diode switch from the high-power microwave pulses, and also during so-called dead time, which depends on the ring-down time of the resonator. After amplification, a signal goes to a quadrature detector where is down-converted by mixing with a reference signal. An intermediate frequency signal is then sampled by a digitizer and processed via Fourier transformation into absorption spectra. In the Figure 13, there is a simplified timing diagram that describes the sequence of events that are executed by a control unit [32].

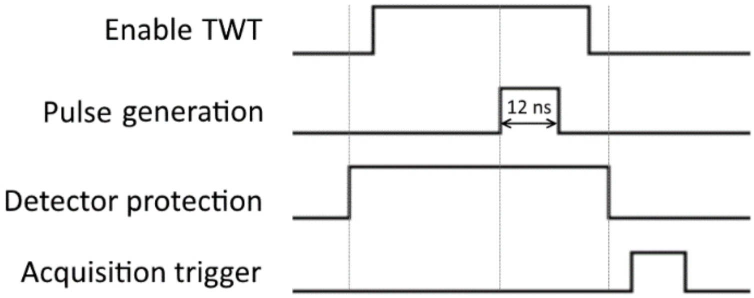

Figure 13: A timing diagram of events in pulsed experiment [32]

Because of the technical obstacles mentioned above, it is difficult to use pulsed EPR to quickly acquire a broad spectrum with a short dead time (<100 ns). Therefore, obtaining EPR spectra of paramagnetic species with very short spin relaxation time is challenging. Also, the acquisition of broader spectra is time-consuming because data has to be accumulated from repeated measurements. But that does not allow us to study fast chemical and biological processes. One way to overcome these limitations is using chirp pulses, which have broader excitation frequency spectra while keeping microwave power relatively low. Another way is to apply a rapid scan method described in the next section.

1.4 Rapid scan

Rapid-scan (RS) EPR is technique in which magnetic field or frequency of radiation is swept so fast that, time interval of a scan through spectral line is comparable to electron spin relaxation time. For example, if spectral line has a full width at half maximum (FWHM) 1 mT (28 MHz in frequency domain if g= 2), and the spin relaxation time is 1 μs, then scan rate above 1 kT/s (respectively 28 THz/s) is required. Generally, relation between sweep rate and relaxation time is:

$$\gamma\left(\frac{dB}{dt}\right) \geq \frac{1}{{\tau_2}^2} \quad or \quad \left(\frac{d\omega}{dt}\right) \geq \frac{1}{{\tau_2}^2}, \tag{22}$$

where a γ is gyromagnetic ratio, B is the applied magnetic field, ω is microwave angular frequency, and τ_2 is a spin-spin (transverse) relaxation time [35]. In such scans a passage effect appears which causes an induction response of the spin system that manifests to FID-like oscillations in detected signal (see Figure 14). However, these oscillations have an increasing frequency. In case of magnetic field scans, it is caused by continuously changing external magnetic field B_0 that affects the spin system and changes its precession (Larmore) frequency while it is decaying. In case of frequency scans, the frequency swept microwave signal is mixed with FID emitted by the spin system while Larmore frequency is constant. Either way, the rapid scan signal can be described by the convolution operation:

$$r(t) = s(t) * d(t) = \int_{-\infty}^{+\infty} s(\tau)d(t-\tau)d\tau, \tag{23}$$

or by multiplication in a Fourier space:

$$R(\omega) = FT|s(t)| \cdot FT|d(t)|, \tag{24}$$

where *FT* denotes Fourier transformation, *r(t)* is the rapid scan signal, *s(t)* is the FID signal, and *d(t)* is the driving function that describes the rapid scan excitation profile [35]. In order to recover the CW-EPR spectrum, the detected rapid scan signal must be deconvoluted. This is simply done in Fourier space as division. But, because in the field scan experiments Lamour frequency is not constant, the signal must be first transformed to reference frame by multiplication with the driving function before its Fourier transformation. A comprehensive derivation of solution for the rapid scan EPR deconvolution was described by Mark Tseytlin [36].

In addition, from the decay of rapid scan signal is possible to extract spin-spin relaxation time via fitting the measured spectrum to a spectrum simulated by modified Bloch equations expressed in rotating frame with B_1 field coordinate system $\{u, v, z\}$:

$$\begin{aligned}
\frac{dM_u}{dt} &= -\frac{M_u}{T_2} - [\Delta\Omega + \omega(t)]\, M_v, \\
\frac{dM_v}{dt} &= [\Delta\Omega + \omega(t)]\, M_u - \frac{M_v}{T_2} - \gamma B_1 M_z, \\
\frac{dM_z}{dt} &= \frac{M_0}{T_1} + \gamma B_1 M_v - \frac{M_z}{T_1},
\end{aligned} \tag{25}$$

where M_u, M_v and M_z are projections of the total magnetization M_0, $\Delta\Omega$ is the offset of the resonance line from the canter of the sweep $\omega(t)$, and B_1 is the magnitude of the magnetic component of the microwaves [35].

However, this approach is valid only in case of homogenously broadened resonance line(s). When inhomogeneous broadening is present (unresolved hyperfine structure, g-factor anisotropy, strains, non-uniform magnetic field distribution over the sample), it would result in new relaxation time T_2^*, that is less than T_2. Approach to dealing with this problem is described in [35].

In contrast to CW-EPR, in the rapid scan EPR experiments the phase sensitive detection is not applied, and a direct detection is used. Signal to noise ratio (SNR) is then improved simply by accumulating data from repeated experiments. Because scans are very fast (for example less than one millisecond) data accumulation from hundreds, or even thousands of scans can be collected in a fraction of second. Because the spin system is at resonance for a very short time, the rapid scan avoids saturation effect, and it is possible to use a higher microwave power for the further improvement.

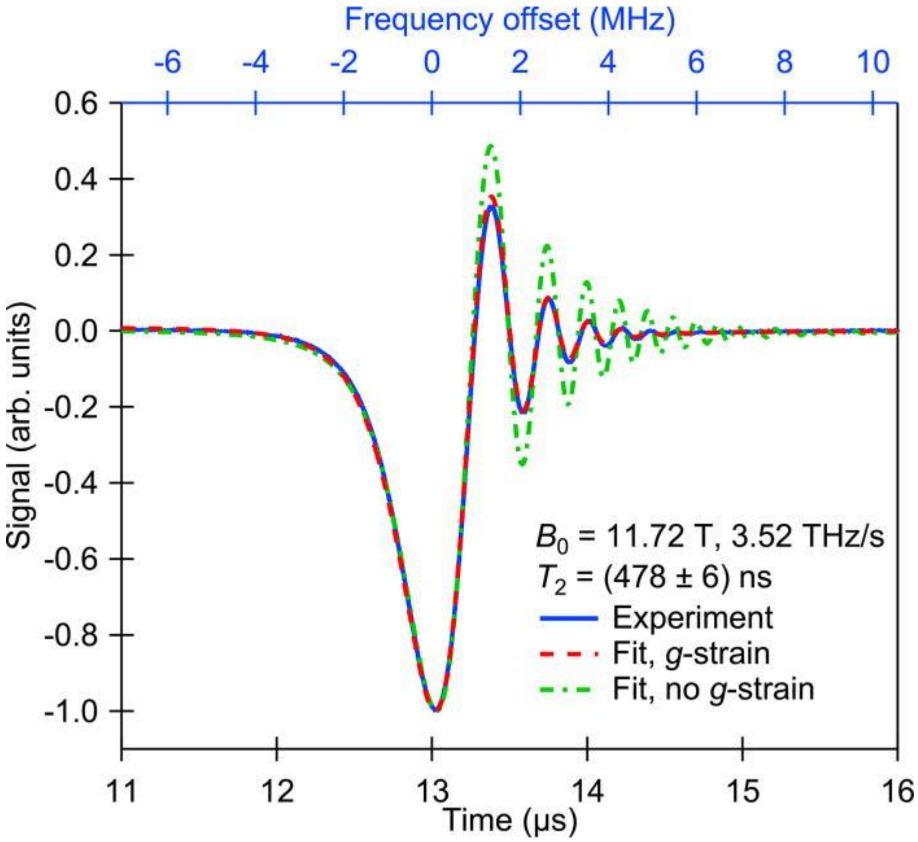

Figure 14: An example of frequency rapid scan ESR acquired on a single micro-crystal of lithium phthalocyanine (LiPc) fitted by simulation with homogeneous and inhomogeneous broadening models. Incident microwave power is 1 mW, 104 averages, and the total acquisition time is 5 s. Taken from [35].

A standard CW-EPR spectrometer that operates in L or S band can be relatively easily modified to operate in magnetic mode of rapid scan. Modulation coil needs to be replaced by a scanning coil, which can scan in a wider range and achieve high tesla per second rate (time derivative of magnetic field). It naturally generates more excess heat than modulation coil and require water cooling circuit. The coil is powered by a driver (basically a high-power audio amplifier) that is capable to operate at frequency of several kilohertz and provide sufficient power required for a fast change of a current via the coil. A triangular [16] or sinusoidal [37] scanning pattern can be used, but the later one is preferred for specimens with a short relaxation time, because it offers a higher ramp rate and is not that demanding to a driver that can simply excite the coil resonantly with a matching capacitor. External static magnetic field is normally pre-set to around level that meets a resonance condition before a measurement is started. It is recommended to use amplitude of alternating (scanning) magnetic field that is ten times larger than width of EPR spectrum. Resonance then occurs when magnetic field passes through quasi-linear area in middle of sine, where change of the field is the steepest. Signal is not acquired by a lock-in amplifier, but rather by instrument with a high sampling rate and memory for accumulation of data such as oscilloscope. Fourier deconvolution is then used to recover slow-scan spectra.

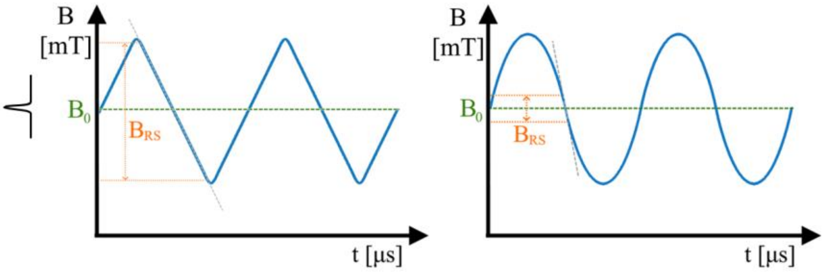

Figure 15: Comparison of triangular and sinusoidal scan profiles. B_0 is resonance field, and B_{RS} is a field range with quasilinear ramp rate. The sinusoidal scan can around resonance field achieve a π-times higher ramp rate than the triangular scan.

In case of HFEPR it is important to consider that amplitude and frequency of alternating magnetic field has to proportionally increase with a static magnetic field. This is not only technically challenging, but also it would cause an excessive heating of a sample. Even though nowadays are available non-destructive pulsed magnets that could provide sufficient ramp rates [38, 39], their low repetition rate is limited by charging of capacitor banks. The charging can take several hours, which is unpractical for use in the rapid scan EPR. Therefore, scanning of microwave frequency appears as more suitable approach [35, 40]. However, modifying a HFEPR spectrometer for frequency rapid scan is not a trivial task, many obstacles can be avoided if this is included in requirements during a design of the spectrometer. In subchapter 3.5 there are further technical details describing upgrade of HFEPR spectrometer. Basically, the spectrometer has to operate in broad range. For this reason, waveguides are not as practical as a propagation through a free space via quasi-optics. A microwave source must allow fast frequency sweeps. Currently, use of arbitrary waveform generators for this is preferred. Then, a microwave detector must have a short response time, comparable to a spin-relaxation time. Because bolometers usually have a relatively slow response, they are replaced for example by a Schottky diode mixers.

The arbitrary waveform generator makes possible to use a trapezoidal scan and acquire the rapid scan signal in area where driving function is constant (as it is shown on Figure 16). For this, the scan range must be comparable with linewidth and rising/falling time must be negligible to spin relaxation time. Then the rapid scan signal becomes an FID which processing is simpler.

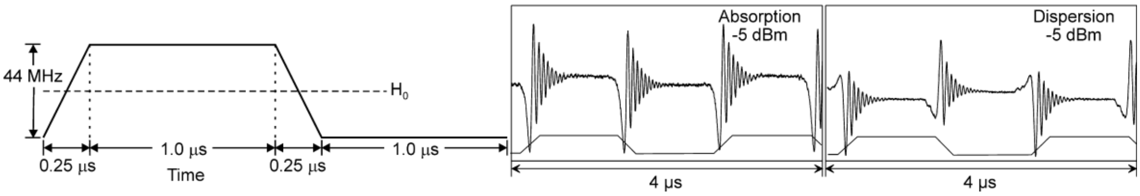

Figure 16: Trapezoidal driving function (left) and example of frequency rapid scan signal (right) of a 0.5mM TEMPONE sample. Taken from[40]. *The sweep rate is 176 THz/s, which is equivalent to 3.8 kT/s.*

1.5 Current software solutions for EPR spectroscopy

Companies such as Bruker BioSpin, JEOL and ADANI Systems (LINEV Group) are well known producers of scientific instruments including EPR spectrometers. They also provide not only the software necessary for operation of spectrometers, but also applications for simulation and evaluation of measured data.

To control EPR spectrometers, Bruker offers a few options. One that runs on Windows platform is WinEPR. It is designated to operate spectrometers of EMX series. Tuning of a microwave bridge and calibration of a resonator is easy with intuitive interface of WinEPR, that is based on a Windows Forms. Experiments focused on effects of temperature, sample orientation, power saturation are supported by automation of measurement routines.

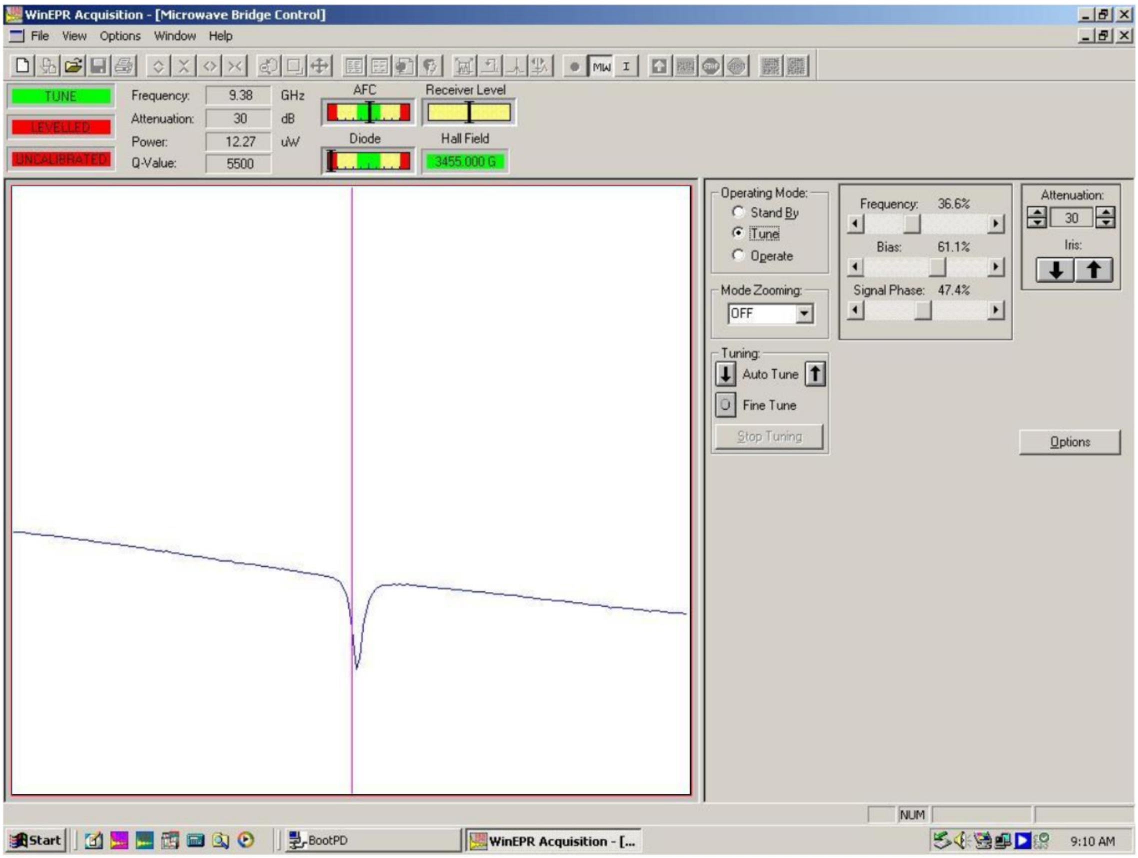

Frequency: 9.38 GHz
Attenuation: 30 dB
Power: 12.27 uW
Q-Value: 5500
Hall Field: 3455.000 G
Operating Mode: ○ Stand By ● Tune ○ Operate
Mode Zooming: OFF
Frequency: 36.6%
Bias: 61.1%
Signal Phase: 47.4%
Attenuation: 30

Figure 17: Screenshot of WinEPR during microwave cavity and bridge tuning process. Taken from [25].

A utility called SimFonia runs on a Windows platform and is capable of simulating a CW-EPR spectra of solution and powder samples, thanks to a fast algorithm based on the perturbation theory. On the Figure 18 is screenshot from SimFonia. Another utility is a SpinFit. This module helps with identifying of radical adducts from a spin trapping experiments. It includes a database with parameters of common radical adducts. It can be also used to simulate and fit powder spectra. Results of simulation can be imported into SpinCount, that is another software module from Bruker. The purpose of the SpinCount is to determinate concentration and total number of spins in a sample. This can be done even without reference sample if the spectrometer is properly calibrated.

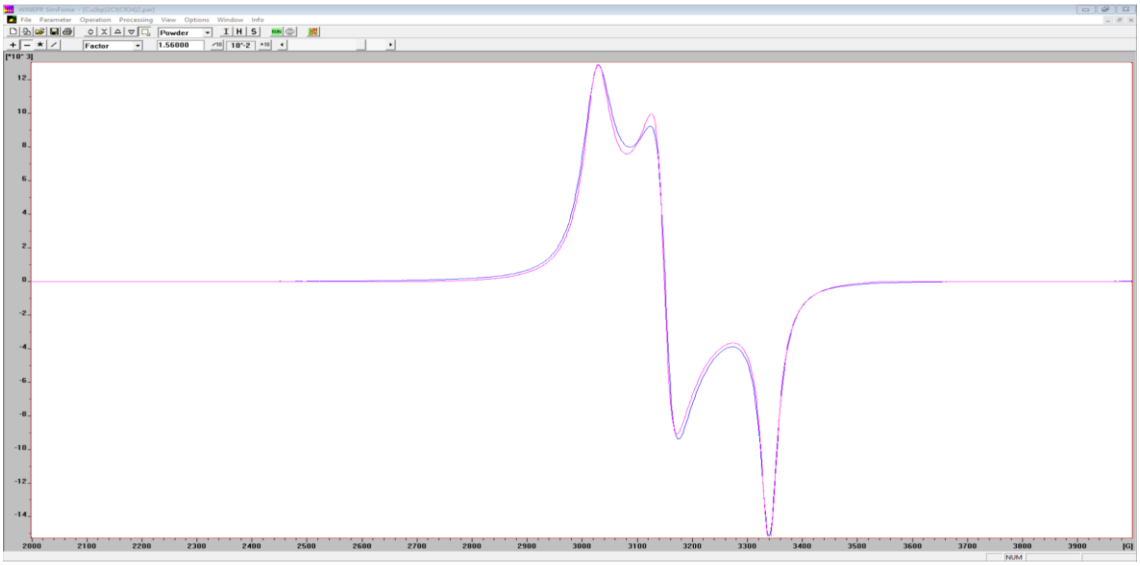

Figure 18: SimFonia simulating spectra of Cu(bp)$_2$(ClO$_4$)$_2$. Taken from Bruker's training presentation of SimFonia [41]

A newer and more powerful solution for EMX spectrometers is Xenon software. This software package reflects a need for reliable and reproducible acquisition and processing of EPR data. It runs on LINUX platform and integrates several modules including the SpinFit and SpinCount. Xenon has a sibling called Xepr that is designated for spectrometers of ELEXSYS series and it also runs on LINUX. Additionally, it supports pulsed operation of spectrometers [23, 42]. User interfaces of the Xeon and the Xepr are shown on the Figure 19 and on the Figure 20 respectively.

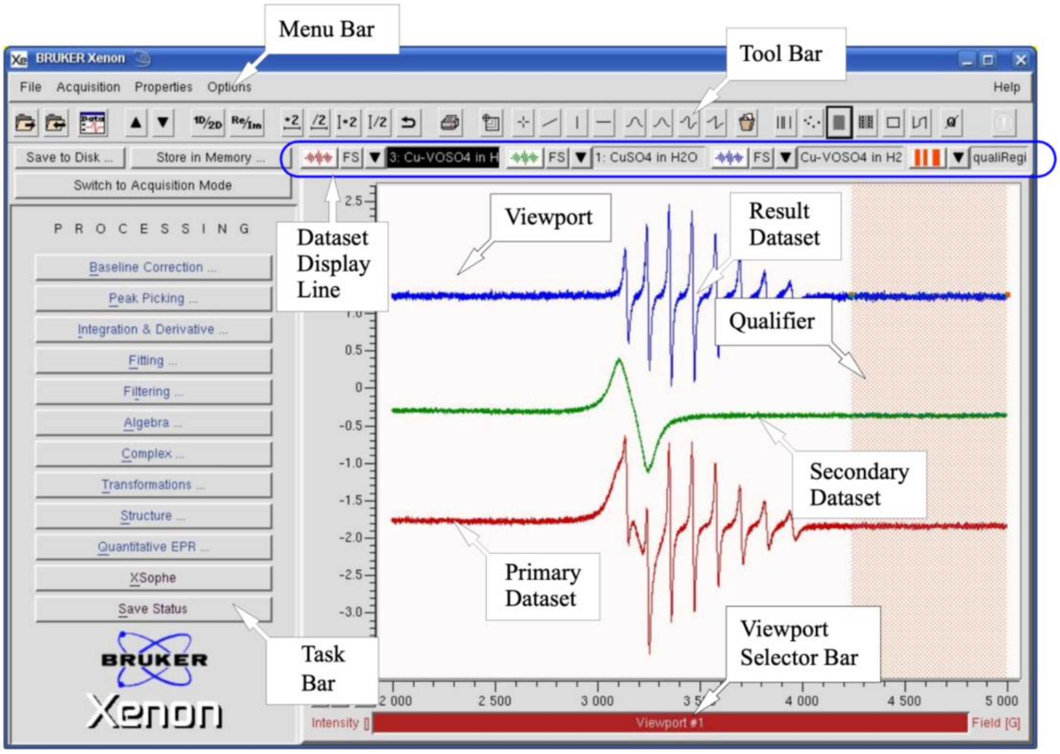

Figure 19: User interface of Xeon in processing mode. Taken from Xeon Data Processing Reference [43].

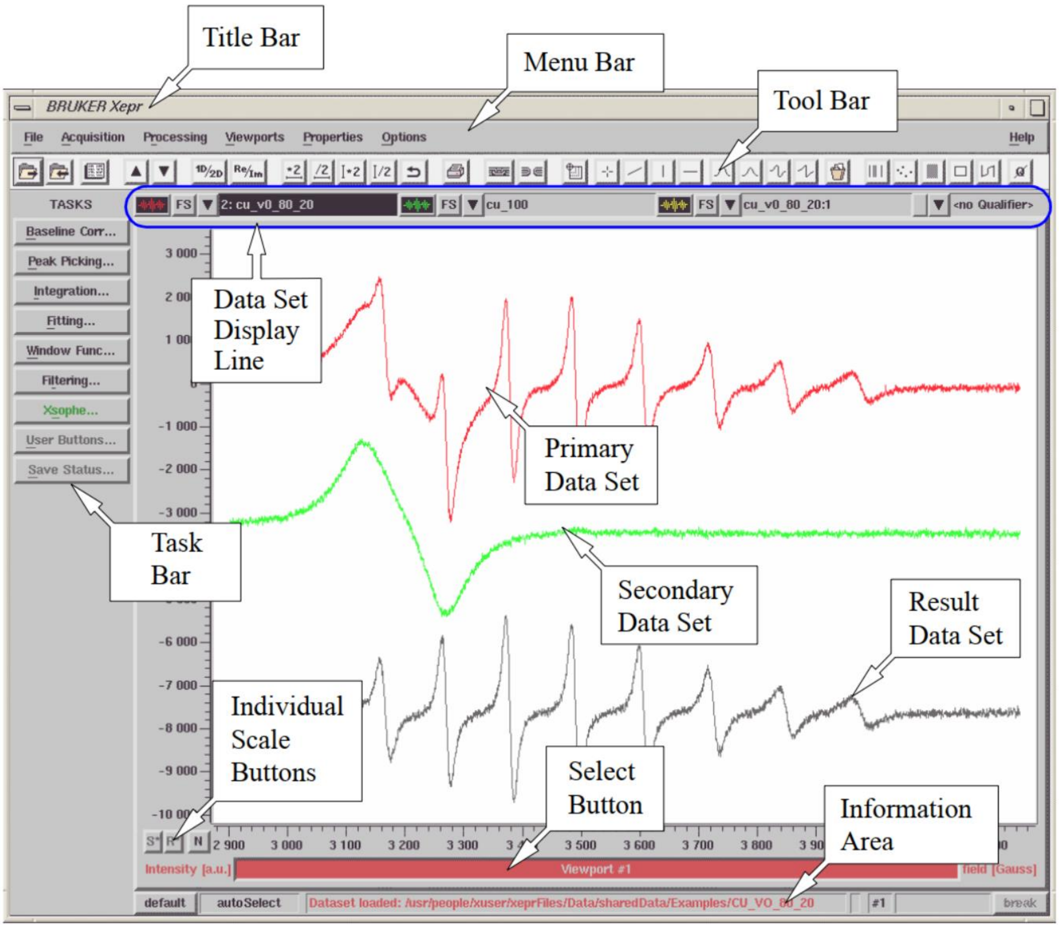

Figure 20: User interface of Xepr. Taken from User's manual to ELEXYS E500 [44].

However, there are also alternative software solutions to control EPR spectrometers. One example is a SpecMan4EPR (Spectrometer manager) developed by a Boris Epel (FeMi Instruments, LLC) since 2002. It aims mainly to custom-made spectrometers that can include many optional hardware components. It was created in a development environment called C++ Builder. SpecMan4EPR is based on a Client-Server architecture. The server is responsible for execution of code that manages a hardware. The client on the other hand just provides a graphical user interface (GUI) to control experiment. Currently it is capable to execute experiments for CW and pulsed EPR, ENDOR, ELDOR, ESEEM and dynamic nuclear polarization (DNP) [45, 46].

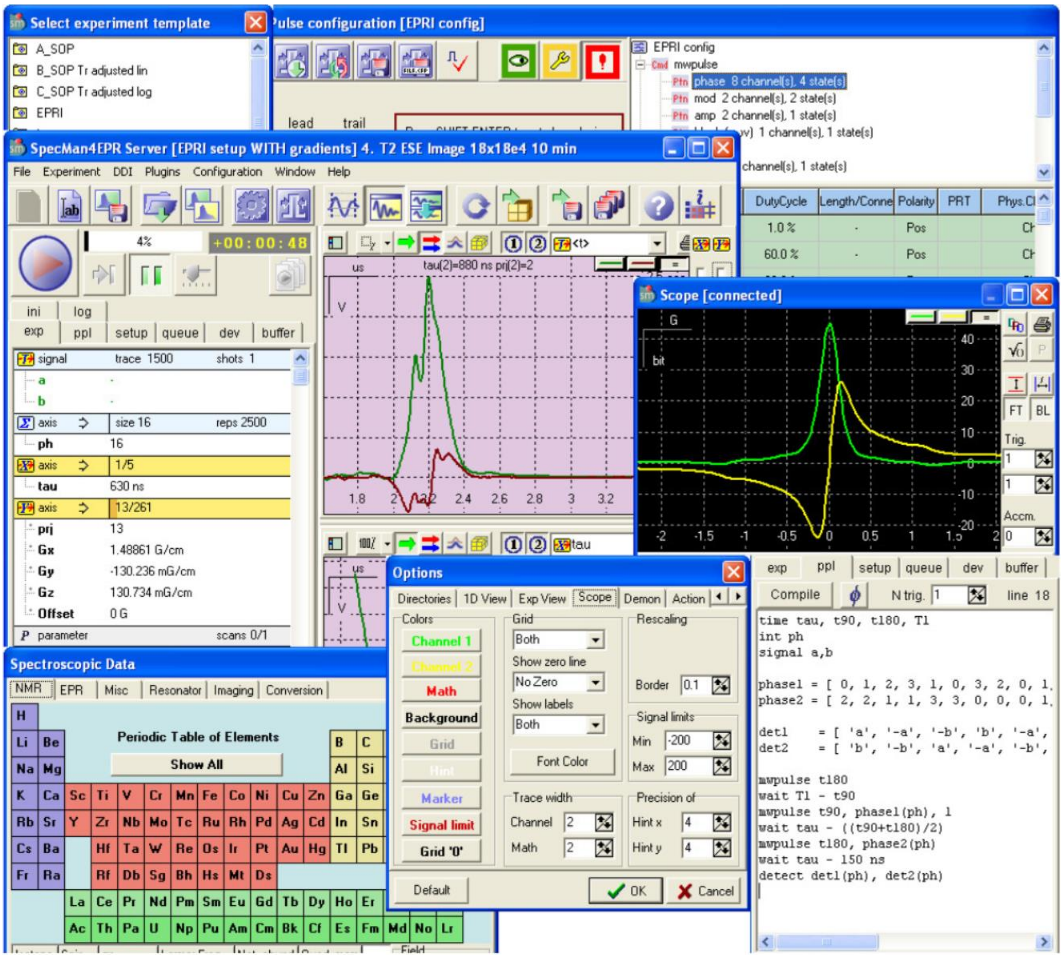

signal	trace 1500	shots 1
axis	size 16	reps 2500
ph	16	
axis	1/5	
tau	630 ns	
axis	13/261	
prj	13	
Gx	1.48861 G/cm	
Gy	-130.236 mG/cm	
Gz	130.734 mG/cm	
Offset	0 G	
parameter	scans 0/1	

```
time tau, t90, t180, T1
int ph
signal a,b

phase1 = [ 0, 1, 2, 3, 1, 0, 3, 2, 0, 1
phase2 = [ 2, 2, 1, 1, 3, 3, 0, 0, 0, 1

det1    = [ 'a', '-a', '-b', 'b', '-a',
det2    = [ 'b', '-b', 'a', '-a', '-b',

mwpulse t180
wait T1 - t90
mwpulse t90, phase1(ph), 1
wait tau - ((t90+t180)/2)
mwpulse t180, phase2(ph)
wait tau - 150 ns
detect det1(ph), det2(ph)
```

Figure 21: Various windows of SpecMan4EPR GUI. Taken from poster of Boris Epel and Reef Morse [45].

One of the mostly used freeware software for EPR spectroscopy is an EasySpin. It is a comprehensive MATLAB toolbox for simulating and fitting of EPR spectra [47]. Stefan Stoll initiated its development and still extends and maintains it [48]. This computational EPR package uses concept of the Spin Hamiltonian for simulating of various EPR spectra. It contains several core functions that can be combined to create a flexible simulation for various cases. There are also few general and robust high-level functions for the CW-EPR spectra simulations of liquid, an isotropic and anisotropic solid state samples, and also the CW and pulse ENDOR spectra. Beside this, the EasySpin can load spectra measured by Bruker spectrometers and fit them by varying parameters of experiment and the simulated spin system. For the fitting there is several algorithms as Monte Carlo, particle swarm, genetic, grid search.

2 Equipment for HFEPR spectroscopy

To investigate materials containing more paramagnetic species that have similar *g*-factor, instruments (EPR spectrometers) with a higher spectral resolution are required. A simple approach to this is to go for a higher excitation frequency. EPR spectroscopy that is done with excitation frequencies above 90 GHz (W-band) or in the magnetic field that exceeds 3 T is usually considered to be a high-field/high-frequency EPR (HFEPR). To operate at such high frequencies and fields, a few modifications in the spectrometer configuration are required. In the past, the main obstacle in the development of HFEPR spectrometers was the state of microwave technologies and the inability to create a high magnetic field. However, the capabilities of HFEPR have been explored already for a few decades, and currently, new technologies bring new possibilities [49]. Further text will focus on instrumentational aspects of HFEPR.

2.1 Electromagnets and superconducting magnets

To accomplish the HFEPR requirement for a magnetic field above 3 T, resistive electromagnets that use classical conductors such as copper become inefficient. Therefore, in many applications superconducting magnets are preferred. They use a superconducting property of some alloys as NbTi and Nb_3Sn, for wirings of solenoid. However, these are superconducting only under certain conditions. A current density, magnetic field, and temperature cannot go above their critical values, otherwise the superconductivity is lost. Therefore, a coil has to be designed to stay within these boundaries in a full range of required magnetic fields [50]. In 2019 was achieved a world record in the maximum magnetic field made by a hybrid magnet (superconductive magnet inside resistive magnet), which was 45.5 T [51]. And recently reported high-temperature superconducting magnets have only 3 cm diameter and can reach 12 T [52]. Moreover, the same group recently performed experiment in which they achieved magnetic field about 47 T using the similar approach [53]. However, temperatures required by most superconductors are extremely low, about 3–7 K, and device called cryostat is used to keep them cool. The cryostat is in principle a huge vacuum flask that is filled with liquid helium. A simple diagram of the cryostat is drawn in Figure 22. A multilayer thermal isolation prevents ambient heat to from reaching helium bath. Often one of the inner layers is filled with a liquid nitrogen that reduces the transfer of heat through radiation.

Because it is not possible to fully avoid slow warming up, some of the helium (and nitrogen) evaporates over time. Therefore, a cryostat should contain a sensor for the measurement of a liquid helium level. Occasionally it is needed to refill the baths, while residual helium gas can be flashed out into a recovery line to be liquified again. Overpressure valves are installed to prevent hazardous overpressure which can grow from evaporation of helium. Because the price of liquid helium is rising (about 20-35 USD in

2020) [54] and not all facilities have built the recovery line infrastructure, some cryostats use a so-called cryogen-free system. It is a closed helium circuit of helium bath, compressor, and cryocooler. A helium gas is exhaust from the helium bath into the compressor, where it is pressed and subsequently liquefied in the cryocooler head [55, 56]. However, cryogen-free systems may add acoustic noise and mechanical vibrations. A facility in which a cryogen-free magnet (CFM) is placed, has to supply the compressors with a cooling water and a notable amount of electrical energy. Ideally, the compressors should be placed in separate technical room to reduce acoustic noise in the laboratory.

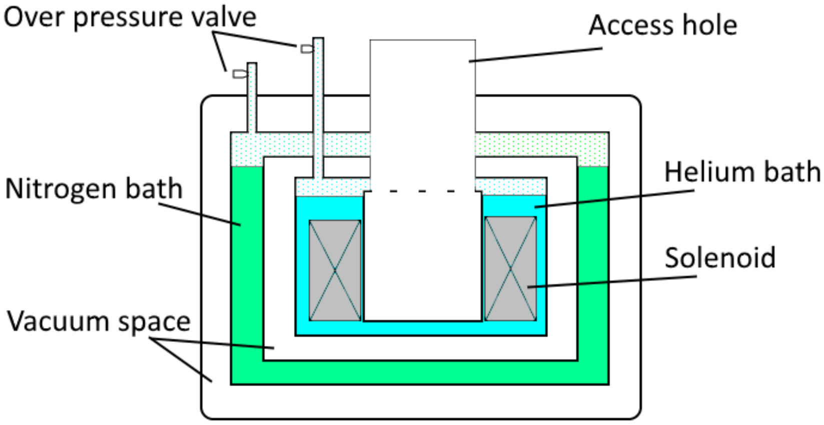

Figure 22:A diagram of a cryostat for a superconducting magnet.

A superconducting magnet coil design must balance between many variable parameters. A wire must be thick enough to sustain forces induced by a magnetic field and electrical current density. On the other side, too thick wire and the physical dimensions of the magnet would limit the maximum number of turns of a coil. But too many turns cause superconducting magnets can have an inductance of a few hundred Henry. Large inductance causes that coil resist to a change in electrical current, which limits the charging speed. Superconducting wires are coated with a thin layer of copper to enhance their robustness and to keep some degree of conductivity in case of a sudden loss of superconductive properties by exceeding the critical temperature, the field, or the current density. Such an event is called a quench. Because the current that usually runs through the coil is in order of tens amperes (or more), it means that there is a lot of energy stored in the magnetic field of the coil. In case of the quench event, this energy is dissipated in the form of heat. That leads to sudden evaporation of helium, and consequently overpressure in the cryostat. In addition, the coil is under sudden mechanical stress and the voltage on its terminals will rise in response to rapid change of the current. For a good distribution of heat in the coil and its mechanical reinforcement, superconducting wires are encapsulated by epoxide resin [50].

The representation of internal circuitry is in Figure 23. On the left side is a current power supply I with its shunt resistance R_i which is usually made of a high-power resistor of a few Ohms (e.g. 4.7 Ω). It limits a current to run through a coil when it is not superconductive (e.g. at room temperature) and helps to dissipate excess energy during the quench event. R_W represents the resistance of leads between the power supply and the magnet. It can be for example a thick silver-plated copper wire. L is the inductance of a superconducting coil. Ty is a thyristor that in case of reaching a voltage limit will switch into an ON state and will remain ON until the electric current drops below a holding threshold. That works as overvoltage protection, which limits the voltage induced during the quench. The inductive reactance of the coil (X_L) is proportional to its inductance and the ramp rate at which it is energized. Once the magnet is energized and the magnetic field is steady the reactance is practically zero Ohms, the superconductive magnet consumes a minimum amount of power.

The part on the right side is an optional accessory that allows a switching magnet between ramping and persistent operation mode. The switch is made of a superconducting wire sensitive to a change of temperature and thermally coupled with a heater R_H. When the switch is warmed up, it becomes resistive, and current from the source runs only through the coil. The magnet is in ramping mode in which the magnetic field is proportional to the supplied current. When the heater is turned off, the terminals of the coil are shorted by the superconducting switch, and electrical current runs through a superconductive loop made of the coil and the switch. The persistent mode is usually used in NMR because it allows disconnection of a power supply and preserves a very stable magnetic field. However, it is important to notice, that before heating the switch, one has to be sure that there is equality of current that runs through a coil and the power supply, otherwise quench may occur. It is also a good practice to have a power backup system in case of a power outage [50], to keep the system controlled, and be able to safely discharge the magnet if needed.

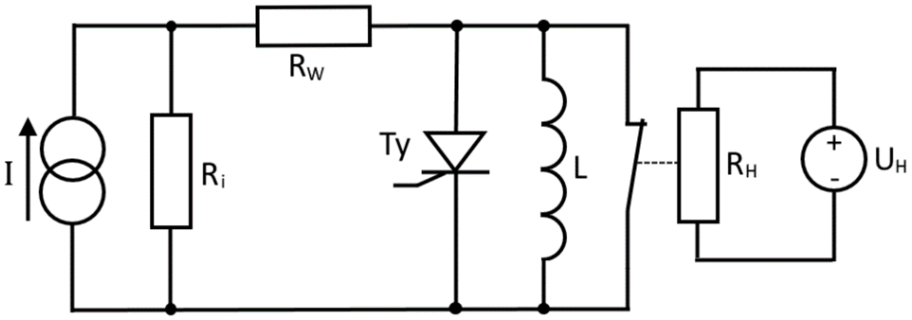

Figure 23: Internal circuitry of system with superconducting coil.

2.2 Millimeter and submillimeter wave sources

Although nowadays there are many different kinds of microwave and infra-red sources, it is very challenging to create a powerful, compact, tunable, and stable source with narrow band output in the range of one decade below and above 1 THz, so this region is known as a terahertz gap (see Figure 24). Whereas in the terahertz gap region can be found many rotational and vibrational frequencies of molecules, it attracted the attention to develop spectroscopic and imaging applications in fields such as astronomy, biomedical diagnosis, security, and chemical analysis. This development was possible thanks to the simultaneous advances in terahertz technology [57]. However, not all currently available sources are suitable for all applications in HFEPR spectroscopy. This section contains just a brief overview of millimeter and submillimeter microwave sources. More information can be found in the literature [26].

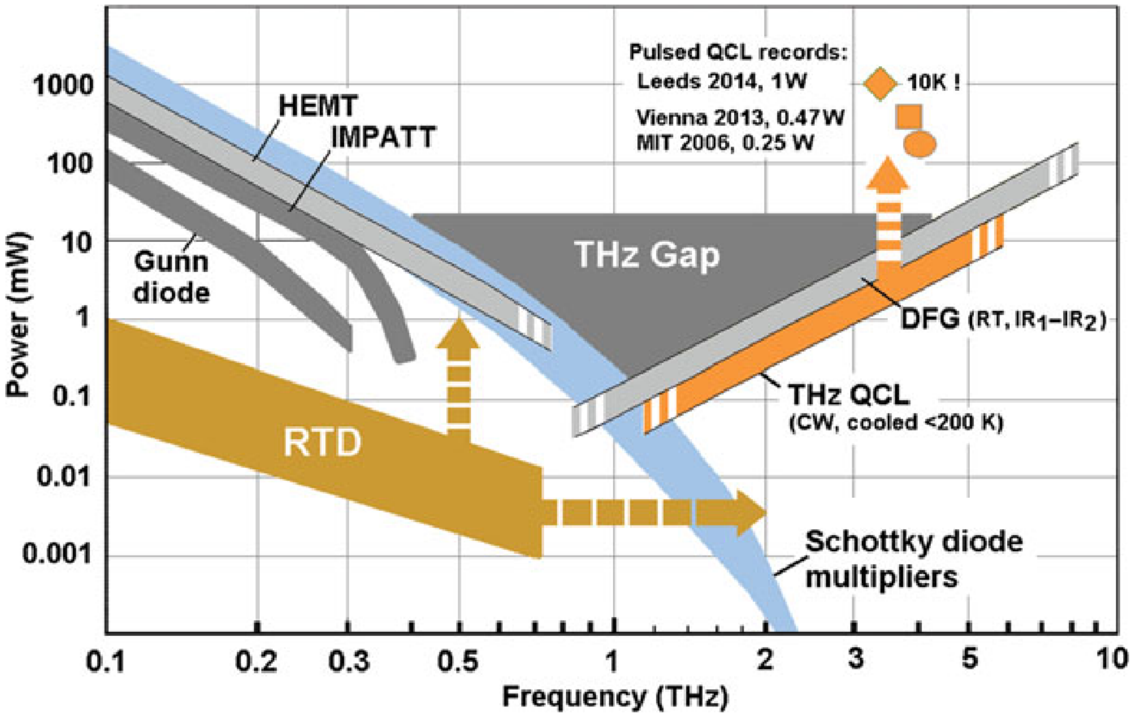

Figure 24: Overview of solid-state THz sources in 2017. Taken from [57]

For a CW-EPR at frequencies up to 150 GHz oscillators based on Klystron or Gunn diodes are applicable. However, they are overcome by newer technologies, especially in pulsed EPR. More convenient for pulsed HFEPR is to use an impact ionization avalanche transit time diode (IMPATT) oscillator with a frequency limit of about 400 GHz. Its main drawbacks are poor noise properties. They generate a shot noise due to a high operating current. They also have a higher spurious noise compared to the Klystron and Gunn diode. That makes IMPATT diodes not suitable for the CW-EPR. Also, their reactance needs to be properly compensated. A good candidate for a high-frequency source could be also BWO. It can provide sufficient power at several hundred GHz and tunability along with theoretically good noise properties. However, because BWO is controlled by a high voltage, of which stability is troublesome, it is being less used at present [26]. Besides klystron and BWO there are other wave tube devices such as Oroton [58] and Gyrotron. For applications that require high power, a gyrotron might be the first suitable choice. It is another maser (microwave amplification by stimulated emission of radiation) device that is successfully used in EPR, NMR, and DNP. In 2001 a gyrotron with an output power of 100 W at frequency 460 GHz was built at MIT [59]. Recent progress in resonant tunneling diodes (RTD) indicates that these devices have the potential to fill the THz gap

[57]. Another technology that already fills a THz gap, but from the side of high frequencies, is the quantum cascade laser (QCL). However, QCL has to be kept at cryogenic temperatures to maximize their output power [60]. Attempts to use far-infra-red lasers as sources that could cover a wide range of frequencies at relatively high power showed up as a dead end because of their poor stability in terms of output power [49]. The free electron lasers have the advantage of high power and broad tunability [61], but they have the size of a building and high energy demands. Finally, there are microwave multipliers. These devices consist of nonlinear circuits that cause distortions of input signal. Consequently, higher harmonic frequencies are produced, and the bandpass filter selects only a desired harmonic and suppresses other harmonics as well as the fundamental frequency. Traditionally, a GaAs Schottky diode was and still is used as a nonlinear device. It belongs to a group of passive multipliers that have a broad bandwidth. An ideal efficiency of such a frequency multiplier is $1/n^2$, where n is the harmonic number. For example, if the frequency is multiplied nine times, the amplitude will be more than eighty-one times attenuated. This can be compensated via a set of amplifiers. Another passive frequency multiplication element is the heterostructure barrier varactor (HBV) also known as varicap. It can convert a second harmonic with higher efficiency than Schottky diode multipliers. However, for HBV it is harder to get higher harmonics and it cannot cover such broad bandwidths. There are also active frequency multipliers whose core is a high electron mobility transistor (HEMT). Their advantage is that the output signal is intrinsically amplified. But, in their design is made a trade-off between gain, bandwidth, and maximum power. Stabilization of their operation point can be also challenging. Overall, the most convenient approach for small laboratories is using compact THz sources such as passive multipliers with a set of amplifiers [62, 63].

2.3 Detectors in Terahertz region

The Schottky diodes can also be used in EPR as detectors of electromagnetic radiation at terahertz frequencies. They have a good responsivity (<1μs) at room temperature for radiation even above 0.6 THz. Modern processes allow creation of structures with a very high cut-off frequency of up to 4.4 THz [64]. They suffer mainly from thermal noise, and because most EPR measurements deal with a low signal, techniques that suppress the noise have to be applied. Usually a heterodyne detection is used, in which the diode serves also as a mixer. At the output of the detector is therefore a signal of intermediate frequency. This signal is usually amplified by a low-noise amplifier [49].

Another commonly used type of detector for THz radiation is bolometer. They are mainly used in astronomy because of their unrivaled sensitivity, relatively low noise-equivalent power (NEP), and wide frequency range (0.15–20 THz). The working principle of bolometers is in the heating of the sensing element by incident radiation, which leads to a change in its resistance. The main drawback of bolometers is their relatively slow response, which depends on the heat capacity of the sensing element. Another disadvantage is that they have to operate at cryogenic temperatures of around 4 K, thus needing to be cooled by liquid helium. For example, the fastest InSb hot electron bolometers cooled by liquid helium have an electrical sensitivity >4V/mW, NEP below 800pW/√Hz, frequency response up to 600 kHz, and bandwidth of 60–1500 GHz [65]. They can be also used as a mixer for homodyne detection and therefore are suitable for a CW-HFEPR [49]. Development of new graphene-based bolometers is currently in progress and can lead to even faster and more sensitive detectors [66].

2.4 Quasi optics

Because microwaves above 100 GHz have a corresponding wavelength below 3 mm, it becomes difficult to fabricate along waveguides suitable for higher frequencies. They would also have considerable losses. It is more convenient to use quasi-optical (QO) components and propagate mm and sub-mm waves as a Gaussian beam [27, 49, 67]. The only necessary waveguides in HFEPR are corrugated feedhorns. They are used to transmit a Gaussian beam from the microwave source into free space and collect the beam from free space into a detector [56, 68].

Probably the most used QO component is an elliptical mirror [69]. Its purpose is to change the direction of the beam (by 90°) and to refocus the beam. A tiny galvanic layer of noble metal on a surface protects the mirror from corrosion and enhances the reflection of waves. Another component that can focus the beam is the dielectric lens. Usually, it is made of PTFE. However, these lenses have to be very thin to reduce their losses that rise at frequencies above 400 GHz [70]. To split and polarize radiation a wire-grid polarizer is placed at 45° angle into the path of the beam. A wave with an electrical component parallel to the wires is reflected and the one with a perpendicular electric component passes through the grid structure. A precise lithographical process is used to etch a fine wire grid with spacing and thickness of wires that is smaller than a wavelength of radiation. Another QO element that allows manipulation with polarization is the Faraday rotator. This device is made of hard ferrite whose magnetic field is aligned along the axis of the beam propagation. An interaction of radiation and field results in the Faraday rotation of polarization. A shift of polarization angle depends on the properties of ferrite material and its thickness, but a little to wavelength. Above mentioned components can be used to create a broadband QO circulator [67].

3 FRaScan HFEPR spectrometer

This chapter introduces the HFEPR FRaScan spectrometer built in the EPR laboratory at the CEITEC BUT. The spectrometer was designed mainly to utilize a Frequency rapid-scan method (development was supported by ERC Starting grant AN714850), but it is also capable of CW-EPR, and frequency swept (FS-EPR) measurements. Another advantage of the spectrometer is in variety of samples that can be studied thanks to a rich palette of developed sample holders [71, 72]. At last, a software solution for computer-controlled experiments was developed in LabVIEW [73, 74]. A brief description of the spectrometer is given in this chapter and further description can be found in the Appendix A.

3.1 Description of spectrometer

The spectrometer was built from parts supplied by different companies. A cryogenic system from Cryogenic Limited includes a cryogen-free superconducting magnet (CFM) whose maximum achievable magnetic field is 16 T, and variable temperature insertion (VTI) subsystem to regulate the temperature of a sample space in the range from 2 to 325 K. Another important part of the spectrometer are microwave sources (synthesizers with amplification-multiplication chain) and detectors (Schottky diode mixers), which were bought from Virginia Diodes Incorporated. To propagate microwaves from sources to samples and then to detectors a quasi-optical setup that covers a frequency range of 80 – 1100 GHz was manufactured by Thomas Keating Limited. To implement the PSD, a middle-frequency lock-in amplifier (MFLI) from Zurich Instruments AG was used. Most parts of mechanical construction (for example strut profiles and servo motors) were supplied by Bosch Rexroth AG.

The superconducting magnet needs to be maintained at an operating temperature of about 4 K. This is carried by a main helium cooling circuit consisting of a cryostat (made by Cryogenics Ltd.), a pair of Compressors (Sumitomo F-70H) and a pair of pulse tube cryocoolers (Sumitomo RP 082). The cryostat serves as a thermally isolated case for the magnet. Each compressor pumps helium via a pair of hoses in and out of cold heads of cryocoolers installed on top of the cryostat. The operation of the cryocoolers is driven by the compressors via four-wire cables. The cryostat dimensions and cross-section are in supplementary documentation in Figure S-1. A temperature monitor model 218 (Lake Shore Cryotronics, Inc.) tracks temperatures at functional parts of the CFM system. It is connected to a PC via a serial port. The monitored parts of CFM are the first and second stages of both cryocoolers, the inner and outer superconducting coil of the magnet, the persistence mode switch, and the supporting plate (temperatures are listed in Table S-1 in the supplementary documentation). The cryostat, the cryocoolers, and the temperature monitor are labeled in Figure 25.

To achieve a homogenous magnetic field in a sample space, the magnet was made as a solenoid. Because superconductor has an extremely low resistance, a power supply for the magnet has to be able to supply a large amount of electric current, while its output voltage can be relatively low. In this case, CFM is powered by SMS120C with a reversing switch option that can change the direction of electric current to make the magnetic field of negative polarity. The firmware of SMS120C ensures that CFM is de-energized before the polarity is flipped. Otherwise, the sudden change of electric current could cause a quench of the magnet. A similar scenario may happen in case of a short power outage, therefore the SMS120C is backed-up via uninterruptible power supply (UPS) Sentinel Pro (from RPS Spa - Riello Elettronica Group). Despite that, a longer power outage leads to overheating and a quench of the magnet as a consequence of the helium cooling system failure. When the magnet is at 16 T, the electric current through the coil is 107.3 A and stored energy is about 600 kJ ($E_m=½\cdot L\cdot I^2$). At the quench, the energy in the magnet immediately dissipates in form of the heat that distributes to the coil, a resistor in a cryostat (passive protection), and a bi-directional thyristor protection circuit built in the power supply, with a trigger voltage of 12V. The CFM also has a superconducting shunt (switch) for switching between a ramping and a persistent mode of operation by heating (and cooling) the shunt above (and below) a critical temperature (see Table S-1). A heater of the shunt is powered via an auxiliary output of SMS120C. A simplified scheme of CFM and SMS120C connection is in Figure S-2.

The VTI subsystem is crucial for temperature dependency measurements. It uses a secondary cooling circuit (schematically depicted in Figure S-3 in Appendix A) to adjust the temperature in a sample space (VTI bore). The flow of the helium is maintained by a sealed scroll pump, that draws the helium out of the sample space. The flow rate of the helium returning to the sample space is controlled by a needle valve. A pressure gauge located on a side of the sample space is used to monitor the flow rate that should be proportional to the pressure. The secondary circuit is thermally coupled with the primary cooling circuit that provides sufficient cooling power for liquification of the helium before it is exhausted into the sample space. A desired temperature in the sample space is achieved by a balance in helium flow, cooling power, and a preheating of the helium. A heater and a temperature sensor are placed at the exhaust of helium into the sample space. Both are connected to a Model 350 Temperature controller, which regulates the heating of the helium, and monitors the temperature of charcoal trap (traps impurities in helium gas), and helium pot. The VTI bore is sealed on its top with a gate valve. An airlock on top of the gate valve enables the insertion of an EPR probe without exposing the VTI subsystem to air contamination. The airlock is evacuated by another scroll pump. The scroll pump, the airlock, the EPR probe, and the temperature controller are labelled in Figure 25.

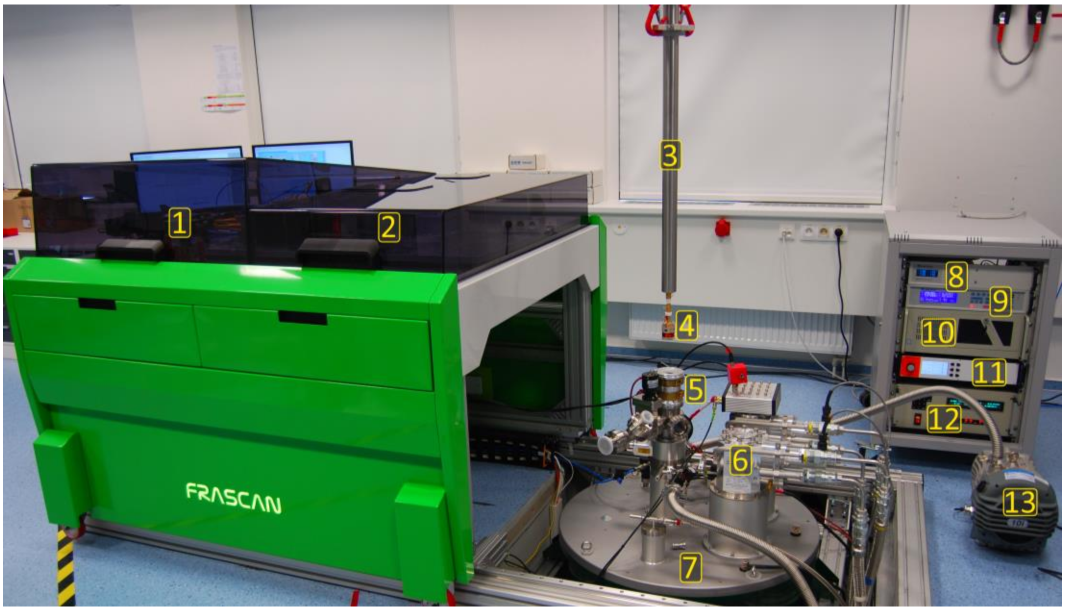

Figure 25: HFEPR FRaScan spectrometer. 1) Cover above terahertz sources, 2) Cover above QO components, 3) EPR probe, 4) Sample holder, 5) Airlock, 6) Cryocooler head, 7) Cryostat of CFM, 8) Temperature monitor, 9) Temperature controller, 10) PC, 11) Piezo-controller, 12) Power supply for CFM, 13) Scroll pump for Airlock.

The spectrometer implements a heterodyne detection technique to receive EPR signals from terahertz waves. For this purpose, it has a pair of terahertz wave sources, which can be seen in Figure 27. One generates a wave for the excitation of the sample (RF) and another one serves as a local oscillator (LO). Both sources consist of a microwave synthesizer and amplification and multiplication chain (AMC) with an input range of 9 – 14 GHz. Additional doublers and triplers can be used to cover the range 82 – 1020 GHz via several subsequent subranges listed in Table S-2. The LO synthesizer is locked to the RF synthesizer and generates a signal whose frequency is lifted by the desired intermediate frequency (IF) portion (divided by multiplication factor). Then even when RF synthesizers generate frequency-swept signals, the IF is kept constant. To control output power a pair of adjustable attenuators is attached to feedhorns from which both terahertz waves are transmitted to the quasi-optical system.

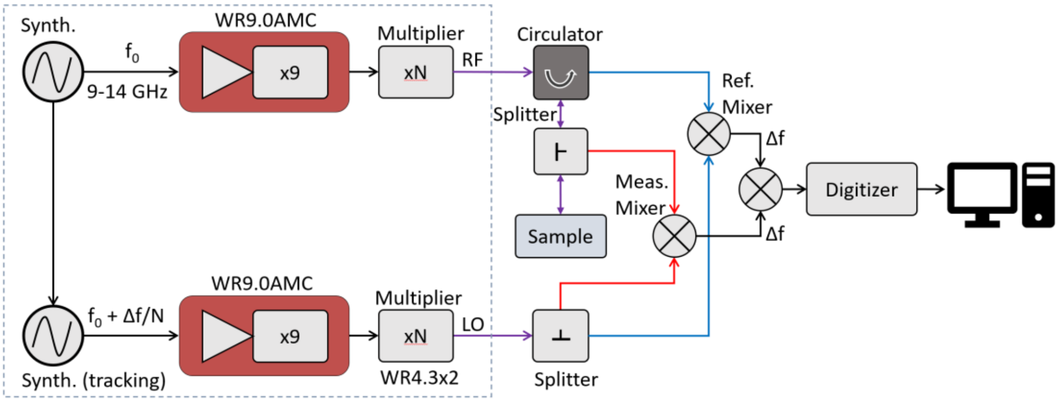

Figure 26: A terahertz generation and detection scheme used in the FRaScan HFEPR spectrometer. The dashed rectangle denotes terahertz sources. In CW-EPR measurements, the digitizer is replaced by a lock-in amplifier.

In the quasi-optical (QO) system, the wave generated by the RF source is first guided to a circulator made of several polarizers and a Faraday rotator. Then it passes through a window on top of the EPR probe head, where it enters a corrugated waveguide. The wave propagates further through a waveguide in a sample holder passes through a sample, reflects from a mirror, and on the way back passes again through the sample. As the wave interacts with the sample (is absorbed), the polarization of the wave changes. Then in the circulator, a component of the same polarization as the original wave is directed to a reference (co-polar) mixer. On the other hand, the component of different polarization is diverted to the measuring (cross-polar) mixer. In the case of the wave from the LO source, the situation is much simpler. The wave is split on a wire grid polarizer and one component is directed to the reference mixer and the other component is directed to the measuring mixer. The QO setup was designed to match the distance of both LO pathways and both pathways of the wave that returns from the probe. The distance matching ensures that waves hit the detectors with the same phase. Signals at an intermediate frequency from both detectors are amplified and brought into another down-converting mixer. The resulting signal is then brought to a high-speed digitizer in case of FRaScan experiments or into a Lock-in amplifier in case of CW-EPR and FS-EPR experiments. A top view of the QO system is in Figure 27 and its complementary diagram of pathways is in Figure S-5. Additional information on the QO system can be found in the thesis of Antonin Sojka [75]. Even though the QO system is passive, its coupling to the waveguide of the EPR probe is crucial. The coupling is adjusted via precise positioning of the QO table by servomotors.

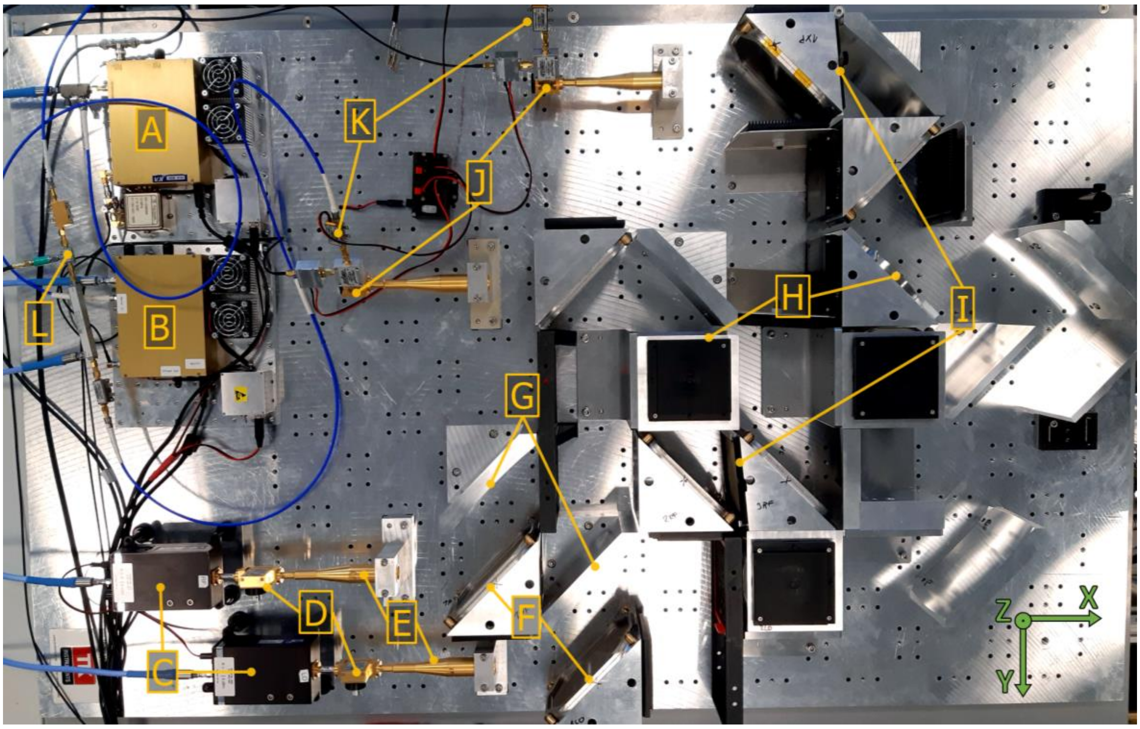

Figure 27: Terahertz system. A) Main synthesizer, B) Following synthesizer, C) AMCs, D) Attenuators, E) Feed horns, F) Polarization grids, G) Focusing mirrors, H) Adjustable polarizers, I) Faraday rotators, J) Terahertz mixers, K) Microwave amplifiers L) Microwave mixer

In CW-EPR and FS-EPR experiments a modulation of EPR signal via low frequency (~1 kHz) magnetic field, and later demodulation of detected signal in a lock-in amplifier is used to improve a signal-to-noise ratio. Theoretical basics for this approach can be found in the Chapter 1.2. A higher modulation frequency (>10 kHz) can be achieved by connecting a resonance capacitor in series with a modulation coil wind up on a sample holder. However, at higher frequencies, an eddy current induced in the waveguide suppresses and deforms the alternating magnetic field around a sample. A modulation subsystem scheme is in Figure S-7. The digitized and demodulated EPR signal is transferred, to a PC. In the case of Frequency Rapid-Scan (FRaScan) measurements, the modulation is not used, but the signal is enhanced by many accumulations from repeated scans. For this, the data are acquired via digitizer ADQ7 from Teledyne SP Devices. To remove a background, the coil on the sample holder can be driven by a positive and negative direct electrical current from the source meter unit, that would lift the magnetic field in and out of resonance. However, this can be done only in a limited range of current, that the coil can withstand.

The servomotors that control the position of the QO table are driven by five IndraDrive compact converters HCS01. The converters are supplied via a secondary switchboard (see Figure S-4) that contains a 100mA residual-current device, EMC filter, 24V DC power supply for the converters, and timer relay that delays a 230V AC supply for Y- and Z-axis converters by one second to reduce a current spike. Servomotors are equipped with a brake that prevents unwanted movement and an encoder with a battery that prevents loss of actual position. The converters are connected with a PC via an ethernet chain, that starts with an X-axis converter. For safe operation, the maximum limits for speed, acceleration, torque, and position were set and are controlled by the firmware of the converters.

The above-described FRaScan Spectrometer compose of several functional parts, that are summarized in Table 2.

Table 2: Summary of the spectrometer's functional parts

Part	**Function and brief description**	**Placement**
Superconducting magnet	Creates strong magnetic field necessary for experiment.	Inside of the cryostat
Compressors (F-70)	Pumping of the helium in a closed circuit.	In technical room
Cryocooler	Cooling of the system by liquefaction of pumped helium from compressors.	Cryostat
Magnet power supply (SMS120C)	Supply a DC current to superconducting magnet to control magnetic field.	In the control rack console
Cryostat	Thermally isolate superconducting coil to keep it at temperature of liquid helium	Pit in the lab floor
VTI space	Thermally separated space for a sample with adjustable temperature.	Inside of the superconducting coil
VTI pump	A sealed oil-free scroll pump nXDS10i that circulates helium in VTI system.	Pit in the lab floor

Needle valve	Regulates a flow of helium into the VTI space.	Cryostat
Control rack console	Carry a PC, temperature monitor (model 218), temperature controller (model 350), needle valve and VTI pump controller, piezo controller (ANC 350), power supply unit for superconducting magnet (SMS120C).	Corner of the lab
Base frame	Provide a mechanical support for cryostat, carry a table frame.	On the lab floor
Servo motor converters (HCS01)	To make QO table remotely movable and adjustable.	In chassis and frame
PXI chassis		In table frame
Uninterruptable power supply	Function of SMS and control PC is sustained at power outage event, for safe discharge of superconducting magnet.	Behind the control rack console
Table frame	Carry QO table, provide a space for additional instruments	On the base frame
EPR probe	Possesses a waveguide, a guiding tube, hermetic electrical connectors with wiring to a sample holder.	Axis of a magnetic field
Air lock	Provide hermetic isolation of VTI space during insertion of the EPR probe.	On top of the cryostat
Sample holder	Loading of a sample, prevents contamination of VTI space by a sample, carries a sample. Several variants. Contains a short waveguide, a modulation coil, a heater, temperature sensor (CX-1050) and a hall (magnetic field) sensor (HGCA-3020).	Attached at the end of the waveguide
Modulation coil	Modulates static magnetic field by AC component to enhance sensitivity to an EPR signal	Sample holder
Source meter unit (Keithley 2450)	For VA characteristic of materials sensitive to a high field irradiation by microwaves, to drive the Hall sensor and modulation coil to lift a magnetic field in the rapid scan.	Control rack console
MW synthesizer	Generate microwave signal at desired frequency (before multiplication).	Quasi-optical table
Amplification-multiplication chain	Amplify a microwave signal from synthesizer and multiply its frequency.	Quasi-optical table
QO table	Transmission of terahertz waves by desired pathways.	On top of table frame
Power supply (HMP 4040)	Supplies a MW synthesizers and AMCs.	In the table frame
Multimeter (AimTTi 1908)	Measure current flowing through modulation coil.	In the table frame
Piezo motor driver	Control carousel sample holder.	Table frame
Lock-in amplifier (MFLI)	Drive modulation coil and demodulate signal form the microwave detector. Acquisition of signal.	Table frame
Digitizer (ADQ7)	Fast acquisition of signal form FRaScan experiment.	PXI chassis

3.2 EPR probes and sample holders

The role of an EPR probe is to place a sample holder with a sample in the center of the magnetic field and bring the terahertz waves there. A waveguide is commonly used to transmit the terahertz waves in restricted space. It is a central part of the EPR probe. It must be made of well-electrically conductive material for good transmitting properties and at the same time a poor thermal conductor to minimize a transfer of heat from the outside of the cryostat into the sample holder. For the FRaScan HFEPR spectrometer two corrugated cylindrical oversized waveguides were made by Thomas Keating Ltd. from alpaca (aka German silver), one optimized for a lower frequency of about 110 GHz and the second one optimized for a higher frequency of about 420 GHz. Each waveguide is equipped with a feed horn at the bottom and mounted to a probe head on its top. The feed horn makes an interface between the waveguide of the EPR probe and the waveguide of a sample holder. The probe head provides a mechanical fastening of the waveguide. It also has several ports to hermetic connectors for electrical signals (Fischer Connectors SA) shown in Figure 28, and a window for the terahertz waves. The window is usually made of a Teflon (PTFE) plate. To reduce unwanted reflections window can be covered by an antireflection finishing layer on its surface or shaped into a cone. However, in this case, a simple Mylar (PET) sheet was used because of its simplicity and sufficient dielectric and mechanical properties. Besides the probes for the FRaScan HFEPR spectrometer, two probes were made to use the magnet with Fourier-transform infrared (FTIR) spectrometer Bruker Vertex 80v [76]. One more probe optimized to achieve very low temperature was made to calibrate temperature sensors, but it can be also used for other electrical measurements.

Around the probes is an outer nonmagnetic steel tube that protects the probe and keeps hermetic encapsulation when the probe is loaded via an airlock. Between the outer tube and waveguide are several copper plates, used as a radiation shield. These reduce thermal radiation from the probe head, which is at room temperature, down to a sample holder, whose temperature can reach ~4 K. They also help to keep the waveguide centered in the axis of the VTI bore. At the bottom of the feed horn is a bayonet mounting mechanism with custom-made electrical connectors for a quick mounting of sample holders.

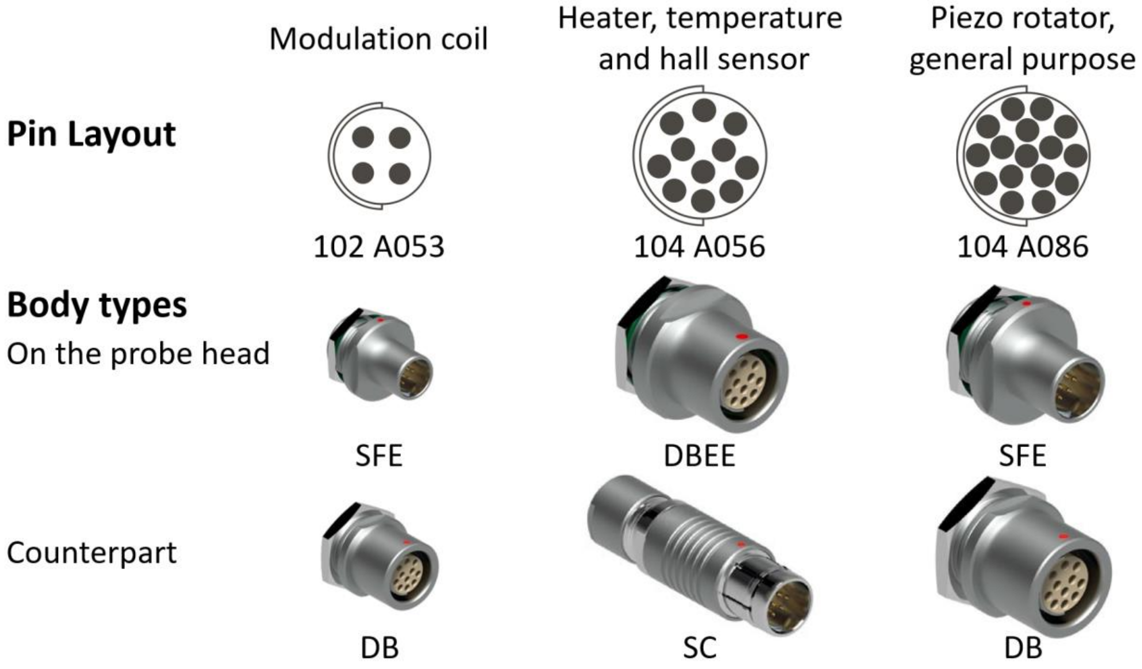

Figure 28: Connectors on EPR probe head for electrical signals.

A set of sample holders was fabricated to cover a variety of sample forms (powder, crystal, liquid, electronic devices, air sensitive). All sample holders implement the common bayonet mounting mechanism, have the same outer diameter and connectors for electrical signals, and are designed to keep the same position of a sample relative to the superconducting magnet. The body of all sample holders is made of polyether ether ketone (PEEK). A modulation coil is made of a copper wire (AWG 26) enameled by polyimide (a.k.a. Kapton) winded up as a solenoid or in Helmholtz configuration. Inside the body is a temperature sensor (Cernox CX-1050) to monitor temperature near a sample. Currently, it is possible to also add a heater for better temperature control and a magnetic field sensor (HGCA-3020) if needed. An aluminum (and later nonmagnetic steel) tube serves as a waveguide. The last part that is common for all sample holders is a metalized silicon mirror which reflects microwaves and on which a sample is usually placed [71].

The first made sample holder was a simple sample holder (SSH) which is shown in Figure 29. It is used for solid-state samples such as crystals, or powders which are either pressed into a pellet or encapsulated in a polystyrene resin. Compared to other sample holders the SSH is the most robust and carries the modulation coil with the highest inductance and field-to-current ratio. Another advantage of the SSH is a trivial manipulation. The SSH consists of two parts, a body, and a base. The body has a modulation coil, waveguide, and a single connector for the electrical signals, On the bottom of the body is an opening with thread for insertion of a base part. The base carries the mirror. A sample is loaded by placing it on the mirror and screwing the base into the body of SSH. Holes in the base allow helium to flow through the SSH. The temperature sensor is fixed to the waveguide, about a half-centimeter above the sample. The magnetic field sensor can be inserted from the bottom into the base, and the heater can be fixed to the waveguide or the base.

By a simple modification of the SSH, a liquid sample holder (LSH) was made. This sample holder contains a sapphire window which hermetically seals a liquid sample, to prevent its evaporation due to a low pressure. The window introduces a small attenuation of terahertz waves, but it is at an acceptable level. Manipulation with the LSH is easy but must be done with caution because of the window. Using a glove box with a controlled atmosphere for loading a sample is advised.

To study the anisotropic properties of crystal samples, a rotating sample holder (RSH) was made by implementing a piezoelectric rotator ANRv51 from Attocube Systems AG. It can rotate at 360°, but the encoder has a blind region of about 45°. As can be seen in Figure 29, the rotator is mounted on a base platform of the RSH. A sapphire rod mounted to a little PEEK platform that is attached to the rotator is used to place a sample about 2 millimeters above a silicon mirror. The mirror is on top of an outcrop from the base platform. The outcrop is hollow from the bottom which makes a place for a hall sensor. The whole base platform is connected to a rotatable part with a thread, that can be screwed into a body part of RSH. In the body is a waveguide with a cutout, for the rotator rod with a sample. The cutout in the waveguide causes a considerable loss of terahertz signal and sensitivity. Because the sample holder is inside mostly hollow, helium can flow around the sample and very low temperatures are easily achievable. However, there is just a little thermal coupling between the temperature sensor and the sample.

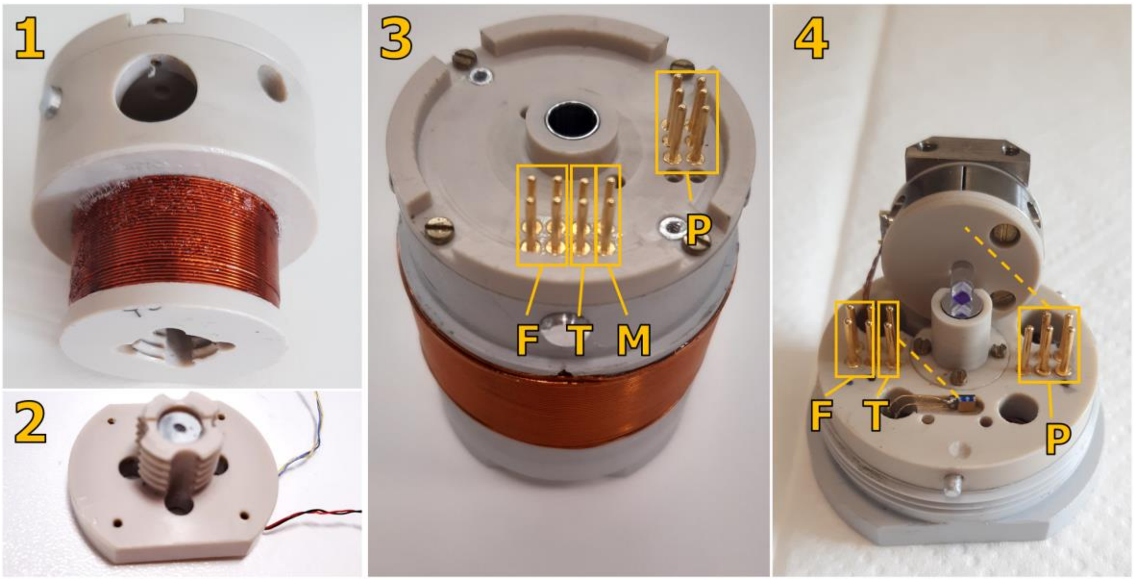

Figure 29: Sample holders. 1) Body of the SSH, 2) Base of the SSH with mirror and sample, 3) Body of the RSH (pins: F- for magnetic field sensor, T- for the temperature sensor, P- to piezo rotator), 4) Base of RSH with a sapphire rod.

Besides mentioned, three other sample holders were made. A chip-sample holder (ChSH) dedicated to electron-transport measurements. It can use up to 16 pins for the connection of electronic devices (transistors, bolometers, solar cells) to measure their properties at low temperatures, high magnetic fields, and under microwave irradiation [77, 78]. Then there is a carousel sample holder (CSH) in which up to 6 samples can be loaded at once. This saves the time needed for change of the samples (hours for a low temperature). Samples are placed in cells on a rotary platform with a reflective surface and a resistive encoder underneath. A piezo motor rotates with the platform to move samples right below the end of the aluminum waveguide. The CSH can be also used for quantitative EPR measurements if one of the cells contains a reference sample. So far mentioned sample holders are well described in published results [71]. The last sample holder was made by Artur Solodovnyk for electrically detected magnetic resonance (EDMR) measurements [72]. It was made to measure variations in the electrical resistance of semiconductors under the electron magnetic resonance. This method allows to detection of even a small quantity of dopants or impurities. The EDMR sample holder is also equipped with optical components for light excitation.

3.3 Modes of operation

The spectrometer utilizes several types of EPR measurement methods. The simplest one is a CW-EPR (theory in chapter 1.2.). In this mode, main synthesizer operates at constant frequency in a selected range and magnetic field is ramped from starting value till the end value at desired ramp rate. Because power supply has a reversing switch, it can also ramp through a negative magnetic field as well. A ramp rate is usually set in range 0.5 to 3 mT/s. The limiting factor is mainly residual heat created during the charging of the magnet, and this heat has to be balanced by the cooling power of the cryocoolers. The frequency range of microwaves is constrained by a set of terahertz components (AMCs, multipliers, feedhorns, faraday rotators, and mixers) that can be exchanged if needed. Because each set has relatively broad operating range, measurements can be easily repeated for a several frequencies without any manual action of operator. This is useful for example to distinguish EPR lines of paramagnetic centers that have a different g-factor. For a good experimental result, it is crucial to choose an appropriate setting of lock-in amplifier, specifically modulation frequency, modulation amplitude, and a time constant (or a cutoff frequency) of a low pass filter. To do this, one must consider an expected width of lines, their intensity, and the ramp rate of the magnetic field. Modulation amplitude should be about a quarter of line width. The time constant should be ten times lower than scan time through the EPR line [18]. A higher modulation frequency should generally lead to a higher sensitivity, but it can also distort lines. An eddy currents induced in a waveguide may lead to heating and inhibit a modulating field to penetrate to a sample (skin effect). The modulation frequency between 1–20 kHz was empirically found as suitable in this setup. Using of CW-EPR method is the most time demanding, but is also reliable, easy to use, and brings good results in terms of signal-to-noise ratio.

Another type of measurement that can be done with the spectrometer is frequency-swept EPR (FS-EPR). This method contrasts with the previous one in the sense that now the magnet is set to persistent mode which keeps the field constant, while the frequency of microwaves is swept. A sweep rate is no longer limited by the induction of the magnet; therefore, a single scan can be done in about one second. On the other hand, it usually works well only in a narrow frequency range (<1 GHz). In a broader span, several effects ruin the quality of results. The most significant are standing waves, caused by unwanted reflection of microwaves at quasi-optical components. Because scans are fast a time constant has to be much smaller than in CW-EPR and the modulation frequency needs to be higher. A signal-to-noise ratio can be improved by an accumulation of data from several scans. The effect of standing waves can be suppressed by subtraction of the background obtained by measuring at different magnetic fields. The FS-EPR mode is mostly used for samples in which the EPR signal gives narrow and intense lines. It can be also used in cases when distortion of lines is acceptable. One example of its practical use is searching for optimal alignment of the quasi-optical table. Because a single scan is done within one second, the intensity of an EPR signal can be evaluated while servo drives move the table to another position.

By combining of previous two approaches, it is possible to obtain the so-called Zeeman diagram. Simply, several hundred (or thousand) frequency scans are done during a single scan of the magnetic field. Data from such an experiment shows how a microwave frequency that excites a spin transition depends on a magnetic field. Because in this case, a partial corruption of EPR lines is acceptable, frequency scans can be about 10 GHz broad, and a field scan can be a few Teslas wide. By repeating measurements in another neighboring frequency ranges, an obtained data can be concatenated to create a large-scale Zeeman diagram. Moreover, CW-EPR spectra of sufficient quality can be extracted for any frequency (shown later in the Figure 49).

3.4 Software solution

For an effective use of all the spectrometer's components, a custom software solution was developed. It was an integral piece for a practical part of this thesis. To speed up the software development process a LabVIEW was used to implement CW-EPR, FS-EPR, and a two-dimensional (2D-EPR) mapping (Zeeman diagram) measurement. These three programs were grouped in a main software solution which is described in this section. For frequency rapid-scan measurements only a prototype of software was developed in MATLAB so far. Implementation in LabVIEW is subject to further extension, however, missing native support for an essential digitizer card makes it challenging. In this chapter brief information about software solution will be provided, while further details are in Appendix B.

An object-oriented design was partially applied in the main software solution. In this sense software solution was split into modules to encapsulate code of related tasks. For example, modules that will be further referred to as submodules, are responsible for remote control over hardware subsystems of the spectrometer such as magnet, microwave sources, VTI, lock-in amplifier (later also for field sensor, sample rotator, and carousel). These submodules operate above an instrument driver as a higher abstraction layer and can be reused and optionally modified in projects that require control over the same instruments. Each module implements a queued message handler (QMH) design pattern. It is a well well-known design pattern for LabVIEW applications [79, 80] and is also a backbone in popular framework Delacor Queued Message Handler (DQMH) [81]. The QMH uses a queue (FIFO buffer) to exchange messages between parts of the program which runs asynchronously (in other threads). This allows submodules to run independently of each other, and exchange status properties or receive commands from a commanding (or supervising) module. To generalize the exchange of messages among modules, a variant datatype was used as a basic element for queues. The variant is a datatype specific for LabVIEW and can be used as a universal data container for a complex datatype such as nested structures. Each instrument controlling submodule waits till a message occurs in the incoming queue. The message is then converted from a variant into a structure specific to the module (example shown in Figure 30) which contains a command in the form of Enum and data in the form of a variant. If the command is valid, the module further converts the variant with data into an appropriate datatype (bool, double, string, array, structure) and executes the required action. The action can be for example a setting of a new parameter value or obtaining some data from an instrument. After successful execution, a response message is sent to an outgoing queue, and the module waits for another message.

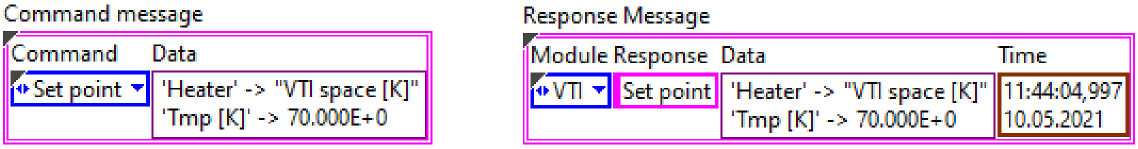

Command message

Command: Set point
Data: 'Heater' -> "VTI space [K]" 'Tmp [K]' -> 70.000E+0

Response Message

Module Response: VTI
Set point
Data: 'Heater' -> "VTI space [K]" 'Tmp [K]' -> 70.000E+0
Time: 11:44:04,997 10.05.2021

Figure 30: Structure of message clusters. At left is message containing a command for the VTI control module, at right is a message after successful execution of requested action.

Further submodules were developed to enable the basic functionality of the spectrometer:

A magnet module controls cryogen free magnet (CFM) subsystem that is responsible for setting of static external magnetic field in the sample area at the desired ramp rate. For the basic operation of CFM, control over the power supply unit (PSU) and the temperature monitor is necessary. Because negotiation with PSU is rather slow and temperature is a relatively slowly changing parameter, both instruments are queried in a two-second interval for a periodic update of their status. The submodule evaluates temperature readings from the temperature monitor, and if some part of CFM exceeds the threshold temperature for a safe operation, it prevents ramping up the magnet or ramps down the magnet if it is necessary.

The temperature controller module manages the operations of the temperature controller that adjusts the temperature of helium in the VTI circuit (secondary cryostat). It can also control a heater in a sample holder when it is connected. It also checks the temperature at four parts inside the VTI circuit: charcoal trap, helium pot, sample holder, and helium temperature at exhaust to sample space. Currently, the submodule does not have the functionality to remotely change the calibration curve for a sensor in a sample holder.

Terahertz source module controls both microwave synthesizers. The submodule gets a single data cluster that contains all parameters for setting the synthesizers: start frequency, end frequency (is ignored in CW measurements), sweep time (is 0 in CW measurements), and an offset frequency that projects into an intermediate frequency between *terahertz sources*. A frequency multiplication factor has to be taken into account in the higher software layer (supervising or commanding module).

The Lock-in module is dedicated to control the MFLI for the modulation and demodulation of the EPR signal. The demodulator's data can be read point-by-point every 100 ms (in CW experiments), or as a set of data points (in FS-EPR and 2D-EPR mapping). The module was extended to measure the electrical current that runs through the modulation coil by multimeter, for accurate setting of modulation amplitude.

The s*ervo drive module* controls the movement of the QO system in all three axes X, Y, and Z.

The rotator module controls the piezo rotator driver for setting the orientation of crystal samples.

S*ource-meter module* is mostly used to drive a hall sensor to measure the actual magnetic field but can be also used to measure the I–V curve of electronic elements sensitive to microwaves.

Further instrument submodules are planned to extend functionalities of the software:

Power monitor to monitor the status of UPS. *PiezoMotor controller* that would allow full integration of carousel sample holder. Development of a LabVIEW driver is in progress, and subsequent implementation of the submodule should be then trivial. *Digitizer module* to integrate the acquisition of rapid-scan signal *and Waveform generator module* to generate arbitrary waveforms.

For each subsystem control module, a simple prototype of supervising (commanding) module was made, just to test its functionality. The supervising module was based on a design pattern combination of a state machine (SM) and event handler. A state machine is in LabVIEW implemented as a while loop with an Enum shift register that gives a current state and obtains a next state. Within the loop is a case structure that executes a portion of code depending on the current state and outputs a decision upon the next state. The state machine starts with an initialization state, then follows a finite number of states in which particular tasks are executed, such as queue message handling, or event handling, and at the end is an application closing state. In the state that covers event handling is implemented code for actions on the user interface. For example, if a user changes the value of the desired sample temperature an event structure handles the user action, and a command to change the temperature setpoint is sent to the VTI control module. The supervising module waits for a response message for 50 ms, then checks the event structure if there is some event pending to be handled. If not, the supervising module waits another 50 ms, and so on. After the VTI control module negotiates with the instrument (temperature controller) a new temperature setpoint, a response message is sent to the supervising module, where it is processed in a message-handling state and displayed on the indicator. Additionally, a simple timing loop periodically sends a command to the VTI control module to obtain actual temperature readings.

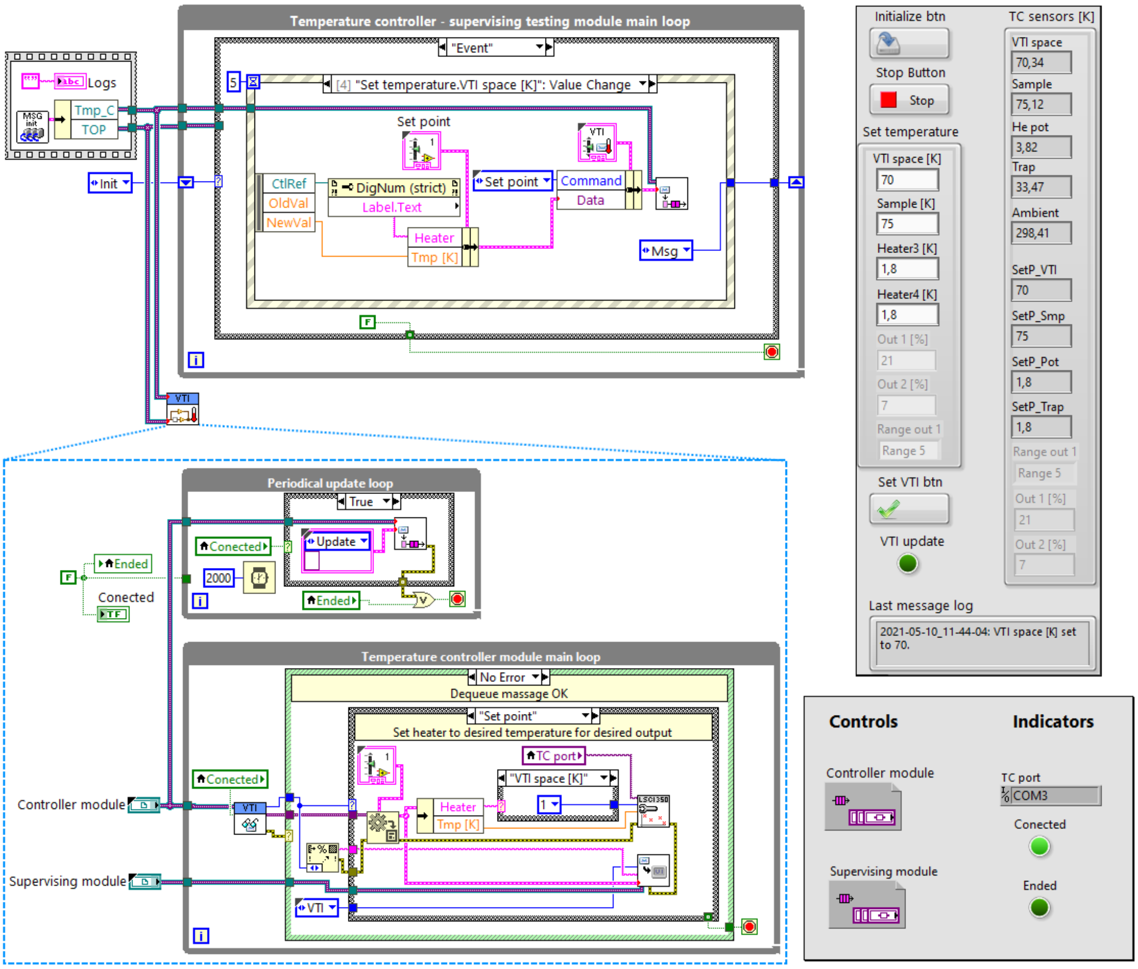

VTI space [K] 70
Sample [K] 75
Heater3 [K] 1,8
Heater4 [K] 1,8
Out 1 [%] 21
Out 2 [%] 7
Range out 1 Range 5

VTI space 70,34
Sample 75,12
He pot 3,82
Trap 33,47
Ambient 298,41
SetP_VTI 70
SetP_Smp 75
SetP_Pot 1,8
SetP_Trap 1,8
Range out 1 Range 5
Out 1 [%] 21
Out 2 [%] 7

Last message log

```
2021-05-10_11-44-04: VTI space [K] set to 70.
```

TC port COM3

Figure 31: Block diagram and front panel examples. Left top - Block diagram of simple supervising module, which front panel is at top right. Down left - a block diagram of temperature controller module with a front panel at down right.

By derivation from the supervising module, three commanding modules were made, one for each type of measurement (CW-EPR, FS-EPR, and a 2D-EPR mapping). Unlike simple supervising modules, they are able to manage multiple instrument control modules and contain execution logic for measurement routines. A state in which the queue of incoming messages is handled contains a further case structure dedicated to managing various instrument control modules. For example, the program for CW-EPR measurements is connected to all necessary modules (magnet power supply, VTI, microwave sources, lock-in amplifier) and several optional modules (sample rotator, servo drivers, source meter). Also, a code for a state that handles user actions is more complex because GUI contains a large number of elements. The GUI of a program is divided by a tab control, into several parts for a different purpose.

The *Status* tab shown in Figure 32 displays the status of connected instruments. The status of instruments is updated at periodic intervals. Two buttons allow to connection or disconnect of any software submodule from the instrument of the particular subsystem. Most important events are logged in a text file and displayed in a circular text array. An example of a log file is in the Appendix B, section Files.

The tab also contains a history chart made of temperature readings from the whole cryogenic system for monitoring temperatures. The temperature records are logged in a separate text file. A folder common for saving both log files and the location of a configuration file can be selected before the application is started. Both path controls are disabled during application runtime.

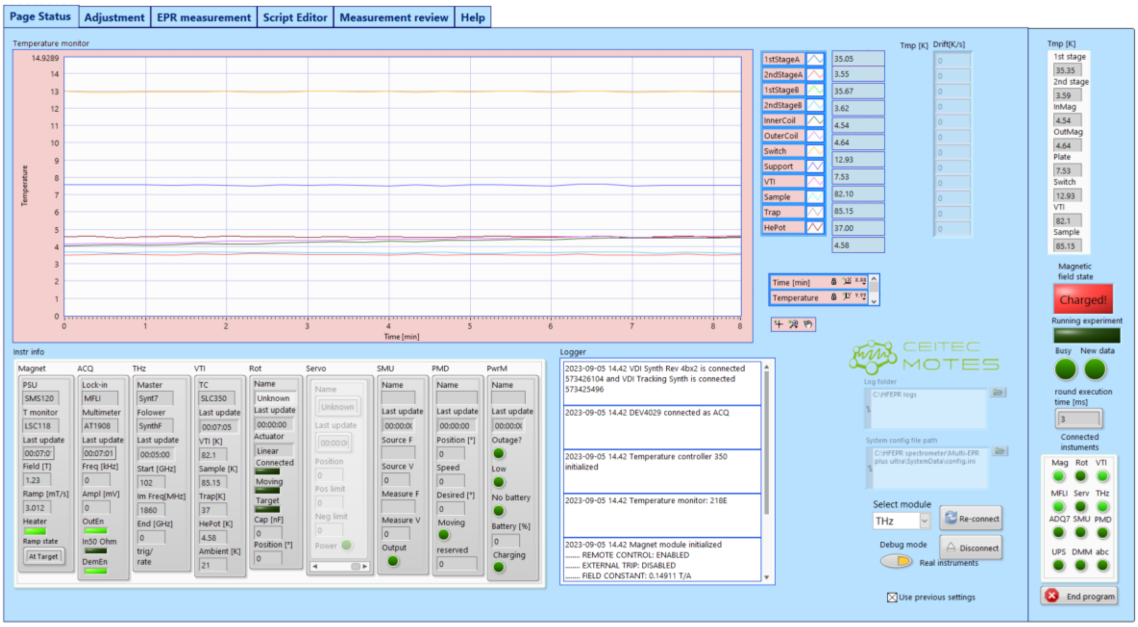

```
2023-09-05 14.42 VDI Synth Rev 4bx2 is connected 573426104 and VDI Tracking Synth is connected 573425496
2023-09-05 14.42 DEV4029 connected as ACQ
2023-09-05 14.42 Temperature controller 350 initialized
2023-09-05 14.42 Temperature monitor: 218E
2023-09-05 14.42 Magnet module initialized
........ REMOTE CONTROL: ENABLED
........ EXTERNAL TRIP: DISABLED
........ FIELD CONSTANT: 0.14911 T/A
```

Figure 32: GUI of the status tab when program is running, and essential submodules are successfully connected to hardware subsystems.

The *Adjustment* shown in Figure 33 serves to directly control individual parameters and actions of instruments. It contains clusters with control elements for the superconducting magnet, microwave sources, servo motors of the quasi-optical table, the lock-in amplifier, temperature controller, sample piezo-rotator (goniometer), and source meter unit. These clusters are normally disabled during measurement to prevent an operator an unwanted change of measurement parameters, but it can be overridden by an administrative password. The magnet control cluster allows the operator to control the power supply for the superconducting magnet and therefore set the desired magnetic field, ramp rate, persistent/ramping mode of operation, and positive/negative direction of electric current. VDI/THz control cluster serves to set up microwave sources, mainly the sweep range, intermediate frequency, and sweep time. The third control cluster is dedicated to servo drives. The operator can simply send the spectrometer to the predefined measurement position, or to the eject position for taking out the EPR probe. In addition, servo motors in the X and the Y axis can move by the desired step, and the motors in the Z-axis can individually move by half of a millimeter steps. The fourth control cluster allows the operator to set up the most important parameters of the lock-in amplifier such as the order and time constant of the low pass filter, modulation frequency, and amplitude. Because the modulation coil is affected by the change of an external magnetic field, optional autoregulation of alternating current through the coil was later added. A variety of sample holders led to different designs of modulation coil, thus the operator has to manually select which sample holder is currently used, so the software can apply a proper conversion constant to calculate the amplitude of the modulation field from an electric current. The last necessary control cluster provides a simple interface to set up the desired temperature of the VTI system and a sample area. Two additional control clusters allow the operator to set up the controller of the piezo rotator (position, step amplitude, and frequency) and source meter unit used to feed a hall sensor by direct current and measure its generated voltage to determine the external magnetic field in a sample area.

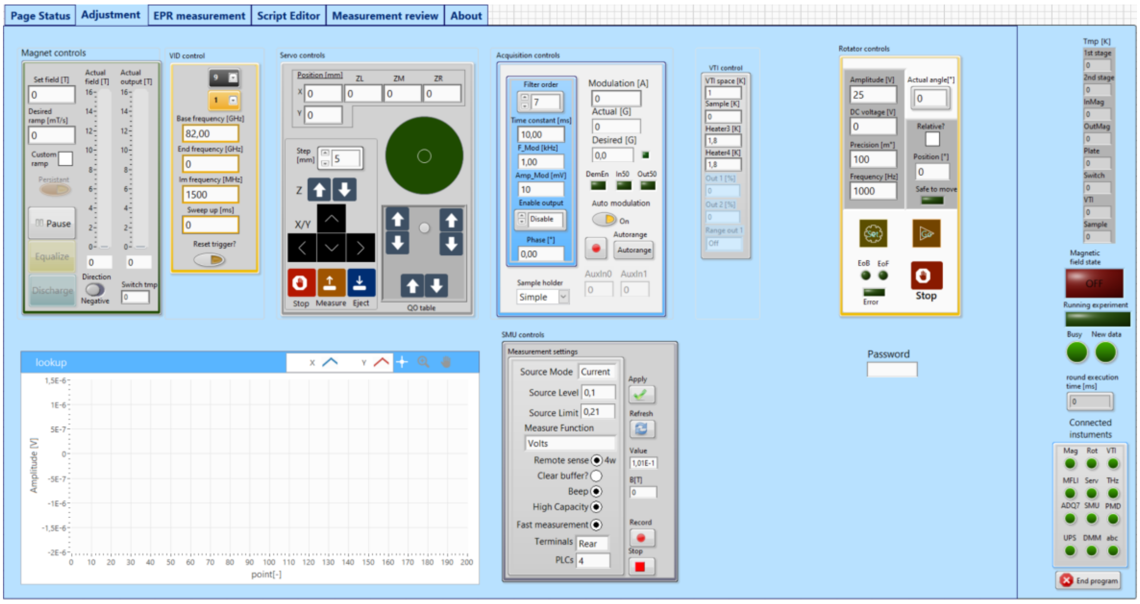

Figure 33: GUI of Adjustment tab. During measurements, controls on this tab are disabled and greyed out, unless password is written.

The *Measurement* tab shown in Figure 34 used the most. It contains options to set, measurements via an automation script, which is made as an array of clusters. The operator can select a destination of a data file, write a sample name that will be included in the name of the file, and write a short note that will be included in the header of the file. A *Run script* button triggers an automated measurement sequence. Figure 36 is a block diagram describing the handling of this user action. The first executable line of the script is loaded, a new data file is created and commands to set starting conditions for the measurement are sent to instruments. From this point, the application regularly enters another state that carries the execution of measurement. When the starting conditions are met, the measurement is started and acquired data are written in the file. The data file of CW measurement is a text file that has a header part and a data part, separated by a single line of underscores. This format was chosen because it can be opened even with a basic text editor and the data can be simply imported into any data analysis software. The header contains the name of the operator, the operator's commentaries, the name of the used sample holder, date and time when the measurement started. Furthermore, there are measurement parameters: range of magnetic field, ramp rate of the magnetic field, frequency of microwaves, temperature setpoint for VTI, stabilization delay, modulation amplitude, modulation frequency, the time constant of a low pass filter in a lock-in amplifier, position of rotator and position of the carousel sample holder. The data part is written regularly during the measurement, every 100 ms (periodical query from the lock-in amplifier). It is organized in columns separated by a tab character and contains signals from both the demodulator's channels (X and Y) of the lock-in amplifier, temperature of the sample, VTI temperature, modulation current, and magnetic field readings. The first line contains the names of the channels, in the second line contains units and data values starting from the third line. Values are in scientific format with six decimal places. Depending on the magnetic field range and ramp rate, the size of the file is typically about 1 to 10 MB. A structure of the data file with example values is in the Table S-3.

At the left bottom corner is a cluster that displays information about currently running measurements. There is also a graph of an EPR signal, obtained by a lock-in amplifier, which is plotted in real time. When a particular measurement is done, the data file is closed and next executable line is selected and the procedure automatically repeats, until there are no more executable lines in the script. This sequence for execution of scripted measurement bathes is described by the flowchart in Figure 35. The script can be also loaded from another tab called a *Script editor*.

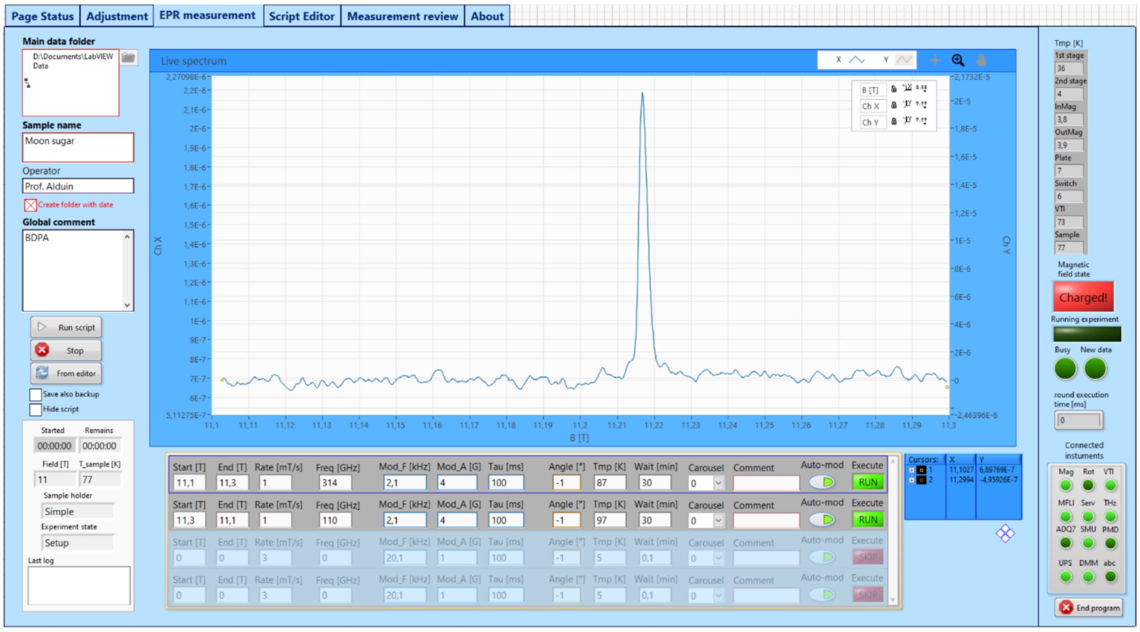

Main data folder: D:\Documents\LabVIEW Data

Sample name: Moon sugar

Operator: Prof. Alduin

☒ Create folder with date

Global comment: BDPA

☐ Save also backup

☐ Hide script

Started: 00:00:00 Remains: 00:00:00

Field [T]: 11 T_sample [K]: 77

Sample holder: Simple

Experiment state: Setup

Last log:

Start [T]	End [T]	Rate [mT/s]	Freq [GHz]	Mod_F [kHz]	Mod_A [G]	Tau [ms]	Angle [°]	Tmp [K]	Wait [min]	Carousel	Comment	Execute
11,1	11,3	1	314	2,1	4	100	-1	87	30	0		RUN
11,3	11,1	1	110	2,1	4	100	-1	97	30	0		RUN
0	0	3	0	20,1	1	100	-1	5	0,1	0		SKIP
0	0	3	0	20,1	1	100	-1	5	0,1	0		SKIP

Cursors:	X	Y
1	11,1027	6,89769E-7
2	11,2994	-4,95926E-7

Tmp [K]
1st stage: 36
2nd stage: 4
InMag: 3,8
OutMag: 3,9
Plate: 7
Switch: 6
VTI: 73
Sample: 77

Magnetic field state: Charged!

Running experiment

Busy ● New data ●

round execution time [ms]: 0

Connected instuments: Mag ● Rot ● VTI ● MFLI ● Serv ● THz ● ADQ7 ● SMU ● PMD ● UPS ● DMM ● abc ●

Figure 34: GUI of main program for CW-EPR measurements. On the top-left are controls to specify data file path. At the bottom part is a measurement script for automated batch of measurements.

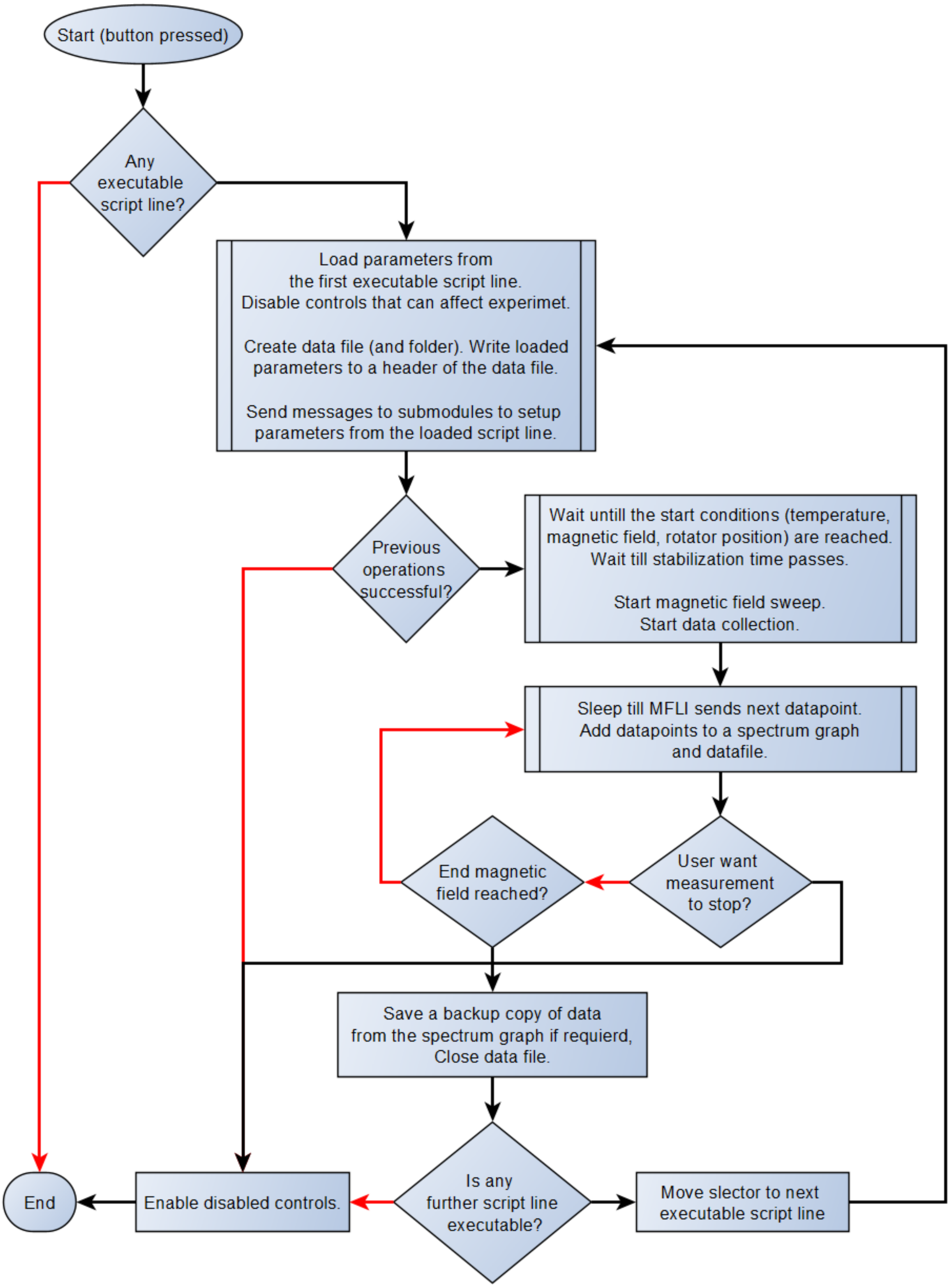

Figure 35: Flow chart of a CW measurement sequence.

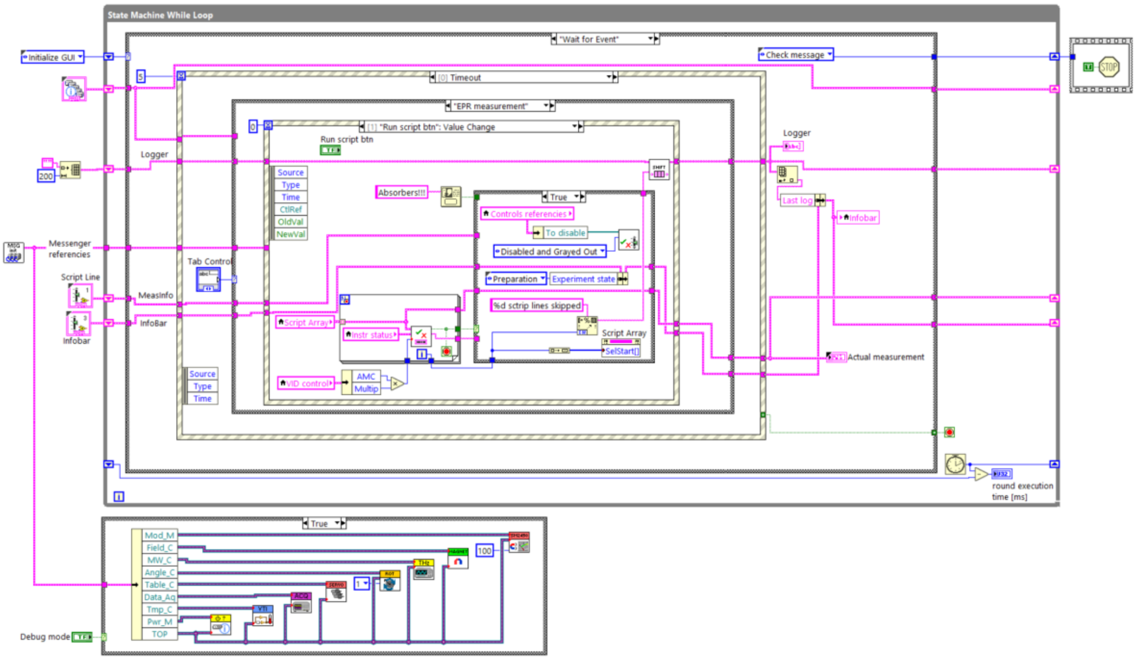

Figure 36: A screenshot of a block diagram for event case that handles user action to run the measurement script.

The *Script editor* tab (Figure 37) is intended to manipulate the script for automated measurements (generate, modify, save, and load). The operator can load a script from the *Measurement tab* and edit it manually. It is also possible to generate the script from a prototype line and step parameters, which is useful mainly for frequency, temperature, or angular dependency measurements. The generated script can be rewritten or appended to the current script. The current script can be saved as a structured text file (example in Appendix B, section Files) and later loaded in the *Script editor*.

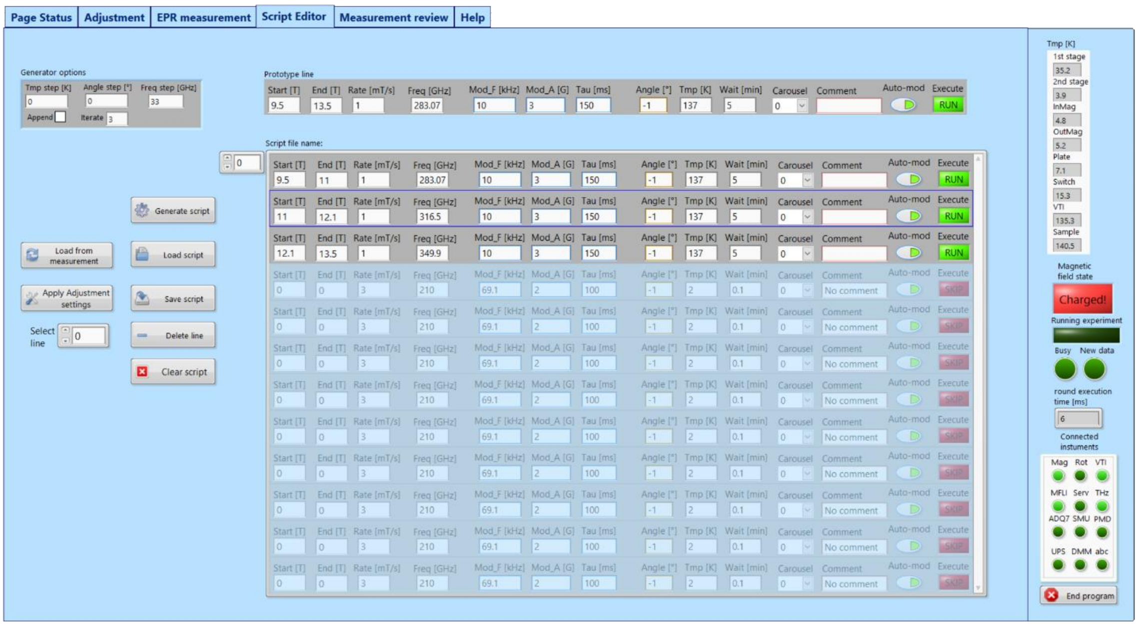

Generator options

Tmp step [K]: 0
Angle step [°]: 0
Freq step [GHz]: 33
Append ☐
Iterate: 3

Select line: 0

Prototype line

Start [T]	End [T]	Rate [mT/s]	Freq [GHz]	Mod_F [kHz]	Mod_A [G]	Tau [ms]	Angle [°]	Tmp [K]	Wait [min]	Carousel	Comment	Auto-mod	Execute
9.5	13.5	1	283.07	10	3	150	-1	137	5	0			RUN

Script file name:

0

Start [T]	End [T]	Rate [mT/s]	Freq [GHz]	Mod_F [kHz]	Mod_A [G]	Tau [ms]	Angle [°]	Tmp [K]	Wait [min]	Carousel	Comment	Auto-mod	Execute
9.5	11	1	283.07	10	3	150	-1	137	5	0			RUN
11	12.1	1	316.5	10	3	150	-1	137	5	0			RUN
12.1	13.5	1	349.9	10	3	150	-1	137	5	0			RUN
0	0	3	210	69.1	2	100	-1	2	0.1	0	No comment		SKIP
0	0	3	210	69.1	2	100	-1	2	0.1	0	No comment		SKIP
0	0	3	210	69.1	2	100	-1	2	0.1	0	No comment		SKIP
0	0	3	210	69.1	2	100	-1	2	0.1	0	No comment		SKIP
0	0	3	210	69.1	2	100	-1	2	0.1	0	No comment		SKIP
0	0	3	210	69.1	2	100	-1	2	0.1	0	No comment		SKIP
0	0	3	210	69.1	2	100	-1	2	0.1	0	No comment		SKIP
0	0	3	210	69.1	2	100	-1	2	0.1	0	No comment		SKIP
0	0	3	210	69.1	2	100	-1	2	0.1	0	No comment		SKIP

Tmp [K]
1st stage: 35.2
2nd stage: 3.9
InMag: 4.8
OutMag: 5.2
Plate: 7.1
Switch: 15.3
VTI: 135.3
Sample: 140.5

round execution time [ms]: 6

Figure 37: GUI of a Script Editor tab. Script can be written manually, generated according to prototype line and generator options, or can be loaded from previously saved script (text file).

In the *Measurement review* tab (Figure 38) data from finished measurements can be displayed, reviewed, and compared. Post-processing utilities (baseline correction, magnetic field lag correction, smoothing, peak detection, data crop) are not yet implemented.

The last *About* tab contains only basic information about the program and a brief guide for using it.

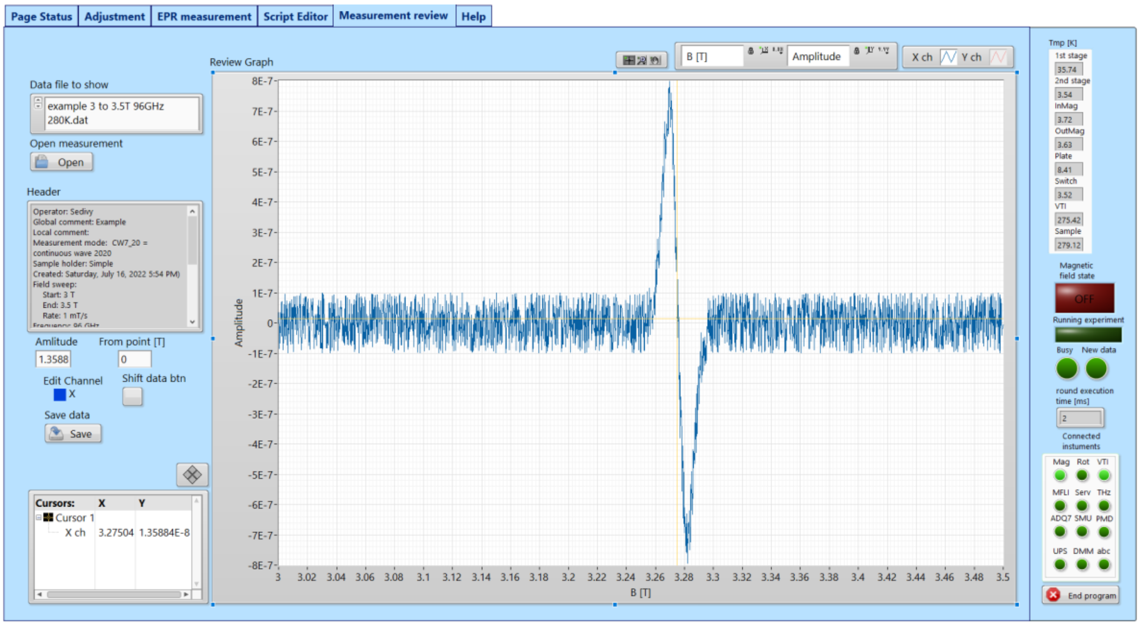

Data file to show: example 3 to 3.5T 96GHz 280K.dat

Header:
Operator: Sedivy
Global comment: Example
Local comment:
Measurement mode: CW7_20 = continuous wave 2020
Sample holder: Simple
Created: Saturday, July 16, 2022 5:54 PM)
Field sweep:
Start: 3 T
End: 3.5 T
Rate: 1 mT/s
Frequency: 96 GHz

Amlitude: 1.3588
From point [T]: 0
Edit Channel: X

Cursors:	X	Y
Cursor 1		
X ch	3.27504	1.35884E-8

Tmp [K]
1st stage: 35.74
2nd stage: 3.54
InMag: 3.72
OutMag: 3.63
Plate: 8.41
Switch: 3.52
VTI: 275.42
Sample: 279.12

round execution time [ms]: 2

Figure 38: GUI of Measurement review tab. Saved data files of CW measurements can be loaded and closely reviewed. A post-processing utilities are not implemented.

The other two commanding modules (for the FS-EPR and the 2D-EPR mapping), have a similar GUI as the one for CW-EPR. The main difference is in the *Measurement tab*. In the case of FS-EPR (Figure 39) are different parameters in the automation script. Also, real-time data are displayed in two graphs, one displays accumulated FS-EPR spectra, and the second displays a current single sweep FS-EPR spectra. In the case of 2D-EPR mapping (Figure 40) the script is replaced by a single measurement option, and real-time data are displayed in an intensity graph a current single sweep FS-EPR spectra are displayed in an auxiliary graph.

The FS-EPR and 2D-EPR mapping can easily create large datasets (about 100 MB collected in a minute). Storing data in a text format would not be efficient anymore, therefore the NI TDMS (technical data management streaming) file format was used [82]. LabVIEW has built-in native support for the TDMS files, which can be otherwise accessed by using packages (libraries) for MATLAB, C, and Python. A few data analysis software such as Origin Pro can also import them and there is also an extension for Microsoft Excel. The advantage of TDMS is that numerical data is stored in binary form and is usually organized as a 1D array in channels (columns) with assigned properties, and the *channels* can be further organized in *groups* (pages). In the case of FS-EPR measurements, *properties* are used to save parameters of measurements, and *channels* are used to contain measured data (spectra). *Groups* are used to separate data from several subsequent measurements if the automation script contains multiple lines. In 2D-EPR mapping experiments, *groups* separate auxiliary data (temperature, magnetic field, modulation amplitude, etc.) and data from X and Y channels.

Folder path: D:\Documents\LabVIEW Data

Sample: 4H-SiC+V

Round: 0

Line: 0

Save data option: ■ Accumulated

Started: 11:35:04
Remains: 00:00:00
Field [T]: 6.8
T_sample [K]: 59.48
Sample holder: Simple
Experiment state: Setup
Last log: Measurement has finished at 11:20:43

F_start [GHz]	F_end [GHz]	Field [T]	Points [-]	Sampling Rate	ModA [G]	ModF [kHz]	Time const [ms]	Auto-mod	Angle [°]	Tmp [K]	Wait [min]	Repeat [-]	Comment
180	196	6.8	8000	7.32 kS/s	4	40.1	0.5		-1	55	5	127	example comment
380	400	0	4096	1.83 kS/s	1	10	1		-1	295	0	0	
380	400	0	4096	1.83 kS/s	1	10	1		-1	295	0	0	

Tmp [K]
1st stage: 34.4
2nd stage: 3.82
InMag: 4.12
OutMag: 4.31
Plate: 7.68
Switch: 8.53
VTI: 55.04
Sample: 59.48

Magnetic field state: Charged!

1 round time: 0

Figure 39: GUI of controlling module for FS-EPR measurements.

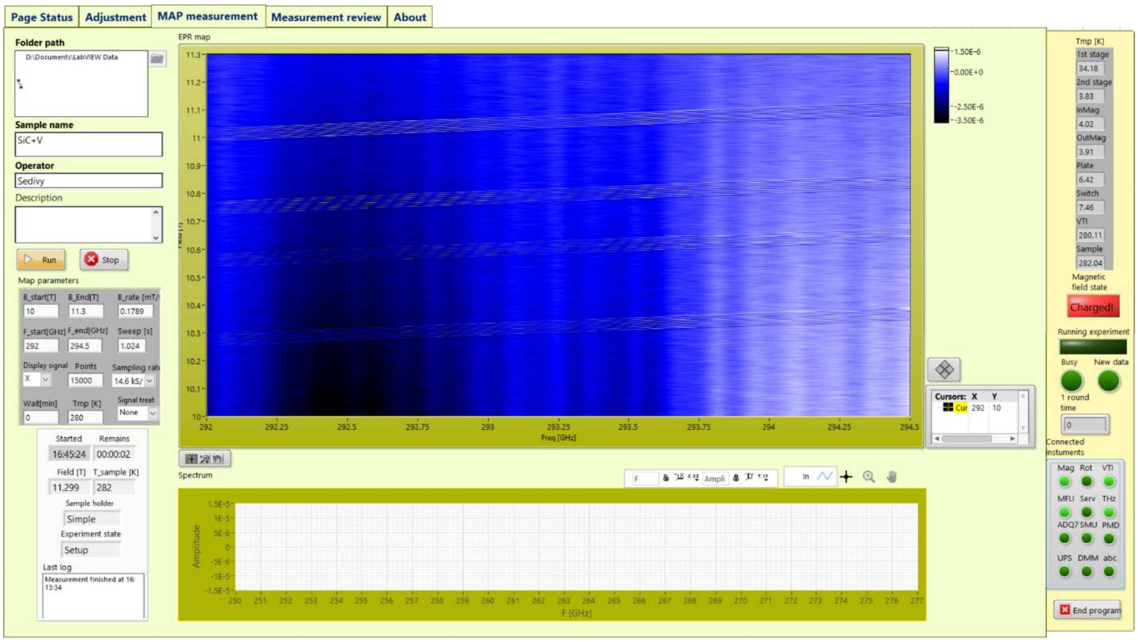

Folder path: D:\Documents\LabVIEW Data

Sample name: SiC+V

Operator: Sedivy

Description:

Map parameters
B_start[T]: 10
B_End[T]: 11.3
B_rate [mT/: 0.1789
F_start[GHz]: 292
F_end[GHz]: 294.5
Sweep [s]: 1.024
Display signal: X
Points: 15000
Sampling rat: 14.6 kS/
Wait[min]: 0
Tmp [K]: 280
Signal treat: None

Started: 16:45:24
Remains: 00:00:02
Field [T]: 11.299
T_sample [K]: 282
Sample holder: Simple
Experiment state: Setup
Last log: Measurement finished at 16:13:34

Cursors: X 292 Y 10

Tmp [K]
1st stage: 34.18
2nd stage: 3.83
InMag: 4.02
OutMag: 3.91
Plate: 6.42
Switch: 7.46
VTI: 280.11
Sample: 282.04

Magnetic field state: Charged!

1 round time: 0

Figure 40:GUI of controlling module for 2D-EPR mapping measurements.

The developed software solution is a working prototype, and it is expected that it will be improved by further development. So far it complies with the main tasks: to control the instrumentation of the FRaScan HFEPR spectrometer and to perform automated measurement routines. During the development, several requirements changed or were added. A few unexpected inconveniences made it difficult to implement for example a carousel holder and the frequency rapid-scan in a current solution. However, potential ways for their implementation have already been explored. In the case of the carousel holder, the control of the piezo motor will require finishing work on its LabVIEW driver. The incompatibility issue of API to digitizer ADQ7 with LabVIEW can be workaround via a wrapper library written in C, or by using the *LabVIEW memory manager* functions that can perform low-level operations such as dynamically allocating, manipulating, and releasing memory. The *power monitor* can be implemented by reading status signals on a serial line (RS-232) adapter. According to *the Riello Sentinel Pro* manual, pins 9 and 8 indicate *operation on battery* and *low battery* respectively. Some UPS equipped with a USB port behave as a plug-and-play device that is recognized by the operating system as a battery. Then reading of *system power status* bits through a kernel of an operating system provides sufficient information about the status of UPS for evaluation of next operations. The architecture of the software may be also reformed. In the ideal case, the commanding module shall be divided into several modules: a Top GUI, a Measurement executor, an Instrument server, an Event logger, and a Data logger. The Top GUI should only present data to the user and handle user actions. The Measurement executor should only manage measurement procedures. The Instrument server would receive commands from the Top GUI or Measurement executor and interpret them to the submodules responsible for the operation of individual instruments or subsystems. Also, it should process data from submodules and interpret them to the Top GUI or Measurement executioner. The submodules that control the actual instruments can be implemented with multiple abstraction layers to decrease the coupling between the Instrument server and particular instrument.

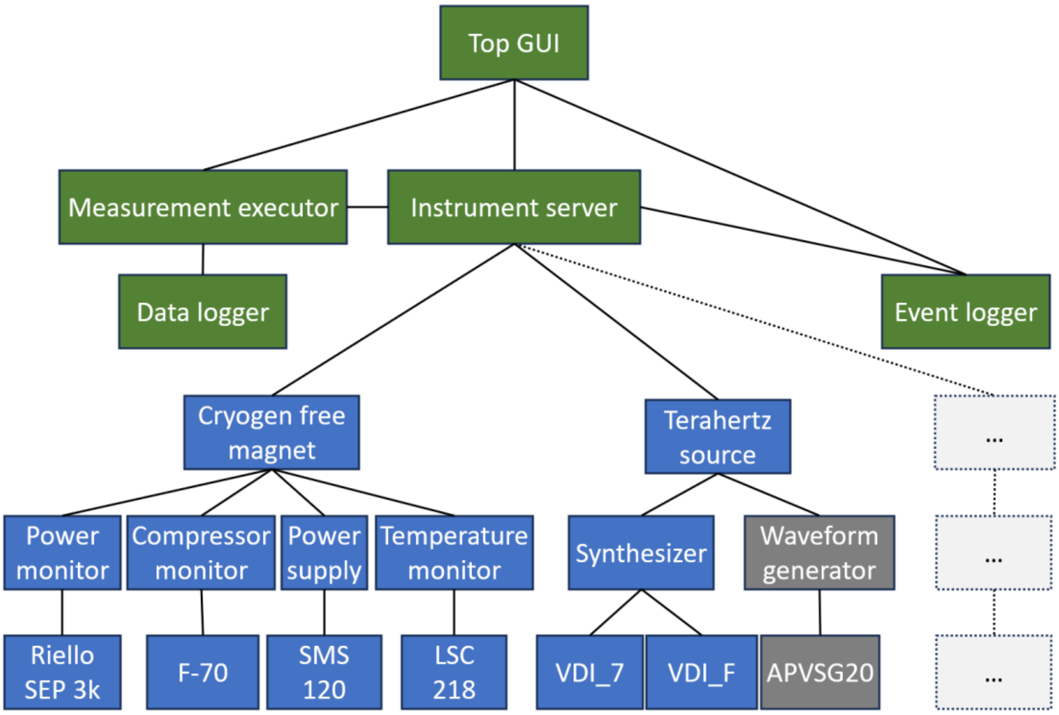

Figure 41: Suggested architecture of improved software solution.

Besides the presented software solution for control of the FRaScan HFEPR spectrometer, an application for the collection of the FTIR spectra in the field domain was made. In its development, the *magnet module* for control of the superconducting magnet was re-used. Then a prototype application that can measure calibration curves of temperature sensors was made by using a *temperature controller* module and *source-meter* module. Another prototype application was made for control of the carousel sample holder. Also, for simple post-processing of 2D-EPR maps (data decimation, background subtraction, extraction of CW/FS-EPR spectra) a simple *Map viewer* application was made. Screenshots of front panels from all mentioned micro applications can be found in the Appendix B subsection *Other micro applications.*

3.5 Implementation of frequency rapid scan

While the quasi-optical system and the terahertz system allow the spectrometer to operate in a broad frequency range and obtain EPR spectra by frequency sweeping, to enable the frequency rapid scan operation, several modifications must be done. First, an acquisition system does not need to support a phase-sensitive detection but must be able to pick up a fast change in a rapid-scan signal that can happen on a nanosecond scale. For this, an oscilloscope, with a sampling rate above 1 GS/s, or a high-speed digitizer is more suitable. Even though the used MFLI has an option to operate as an oscilloscope, its sampling rate is not sufficient. Second, the sweep rate of microwave sources has to be fast enough to cause rapid-scan oscillations. The sources from VDI are able to 2.5 THz/s sweep rates in the 325-500 GHz range (after 36x frequency multiplication), which is merely sufficient for paramagnetic species that have relaxation time of about 10 microseconds and their spectra have a linewidth of about 1 G. A faster sweep rates can be achieved with a voltage-controlled oscillator (VCO) or arbitrary waveform generator (AWG). At last, the EPR signal from frequency rapid-scan can be relatively small compared to the background caused by frequency-dependent properties of the quasi-optical and the terahertz system, absorption in the air, or standing waves. If the same experiment is repeated, but just a static magnetic field shifted in such a way that the resonance condition is not met during the whole frequency sweep, a pure background signal is obtained, which can be subtracted to clean the EPR signal. For a narrow spectrum (~1 mT) a small field step can be done by applying a DC electrical current on the coil that was originally meant for a field modulation by an AC electrical current. Third, the magnet has to create a strong and constant magnetic field during the whole data accumulation.

Since the microwave bridge was originally designed for operation in a broad frequency range, it is suitable for rapid scans as it is. Only microwave synthesizers have a relatively slow sweep rate that limits their use. They can be used for CW-EPR, FS-EPR (slow scan), and rapid scan on the samples with a long spin relaxation time and narrow EPR lines. This is for example case of lithium phthalocyanine (LiPc).

To be able to perform frequency rapid scan (FRaScan) measurements on various samples, a vector signal generator APVSG20 from AnaPico AG (Switzerland, Glattbrugg) was added. It can generate a signal of arbitrary profile in the frequency range 0.01 – 20 GHz, with 1 mHz resolution. Output power is adjustable from -20 dBm to +17 dBm with 0.01 dB resolution, however in practice, this is set to a constant value during the whole measurement. The arbitrary waveform can have a maximum length of 334 million samples (when marker signals are active), with a 16-bit resolution. A warm-up time after which it has a stable performance is 5 minutes, and power consumption is below 400 W. On the front panel, it has two outputs, which are connected to inputs of both AMCs (RF and LO). An auxiliary output at the rear panel is used for a marker which is a signal that triggers data acquisition at the desired moment from the start of the waveform. The generator is controlled via an application provided by AnaPico, but waveform data are generated by a MATLAB script.

In CW-EPR a phase-sensitive detection is applied by using a field modulation and lock-in amplifier to significantly improve an SNR. But, in a rapid scan, an EPR signal changes are so fast, that field modulation is not applicable, and instead direct detection is used. But, directly detected EPR signal from a single frequency scan has a such low SNR, that it is often buried in the noise. The SNR can be improved by repeating the rapid scan and averaging the detected signal. A random noise then cancels itself out and SNR is improved proportionally to the square root of repetitions (100 measurements increase SNR 10 times). Considering all the mentioned requirements for the acquisition of an EPR signal in a rapid scan, a high-frequency oscilloscope could be an ideal instrument. However, its price would be unnecessarily inflated by several firmware and hardware options and features that are not needed for the rapid scan. Also, fast oscilloscopes have usually only about 8-bit native vertical resolution, and the firmware can limit the maximum number of averages. A more flexible and cost-effective are digitizers.

Digitizers are devices that use analog-to-digital converters (ADC) to sample an analog signal into digital values and simply store them in a memory buffer. Usually, a signal conditioning circuit adjusts gain and an offset before the signal is converted, and likewise, a digital signal processor treats the signal (digital filtering e.g.) before it is stored in the memory. More sophisticated models have several ADCs per channel to multiply a sampling rate. Timing and triggering circuits are then also crucial. Finally, a controller manages whole data acquisition, as well as data exchange with a computer. The firmware of a digitizer is usually capable of only trivial signal processing such as filtering, averaging, segmentation, decimation, etc. therefore further processing needs to be done by computer.

To upgrade a signal acquisition in the built HFEPR spectrometer by needs of a frequency rapid scan operation, an ADQ7 digitizer from Teledyne SP devices, with an optional advanced time-domain firmware (FWATD) and PXIe form factor, was used. It has input bandwidth DC - 3 GHz with a sampling rate of 10 GS/s in single-channel mode, or 5 GS/s in dual-channel mode. With a 14-bit resolution and 4 GB DRAM, it can store waveform up to the length of ~$2 \cdot 10^9$ samples. Moreover, it has a user-programable FIR filter. Because of the PXIe form factor, it needs to be installed in the PXIe chassis, which is then connected to the PCIe bus of a PC via the MXI interface. Alternatively, the ADQ7DC can be connected to a PC via internal USB, but still needs power from the PXIe chassis The FWATD modifies the behavior of the ADQ7. It adds a digital baseline stabilization (DBS), an algorithm for non-linear noise suppression, and the waveform averaging (accumulation). The length of the waveform is reduced to $32 - 2^{21}$ (~2 million) samples with granulation of 32 samples (in the single-channel mode), but it can perform up to 260 thousand (2^{18}) accumulations.

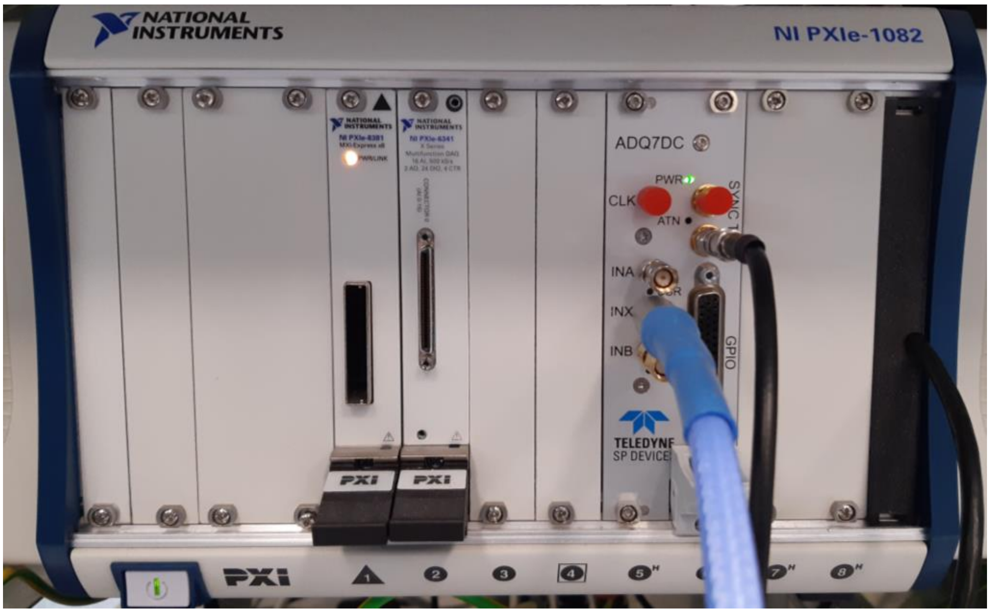

Figure 42: PXIe chassis with ADQ7DC in a single channel mode. The digitizer is connected to PC via USB3.0 on the right side of the chassis. (MXI and GPIO cards are currently not used.)

The ADQ7 was supplied with a software development kit (SDK) that includes comprehensive documentation, USB and PCIe drivers, several command line tools for maintenance and debugging along with their GUI called *ADQAssist* (for firmware updates), an application for simple control of digitizers from the Teledyne SP devices *ADCaptureLab* and its successor *DigitizerStudio*, and an application programming interface (ADQAPI, 32 and 64-bit DLL) with examples for *C*, *C++*, *C#*, *VB*, *MATLAB* and *Python* along with a few helpers for a high-level programming languages. Unfortunately, a LabVIEW driver is not part of the SDK, but with some workarounds, it is possible to create a custom driver by calling functions from *ADQAPI.dll*. In order to do so, several approaches were tried. The first approach was using the LabVIEW tool *Import Shared Library Wizard*. This tool loads the library file and guides a user through the import of desired functions, into a collection of wrapper VIs that uses *Call Library Function Node*. The ADQAPI contains about a thousand functions, and many are not necessary because they are dedicated to other devices or service and maintenance purposes, so only those functions that were valid for ADQ7 (based on a reference manual) were selected (list is in *Appendix B*). But some of those functions work with pointers to nested data structures and the wizard tool cannot import them automatically. Their wrapper VIs must be manually modified. Also, in some cases, functions require pre-allocated space for the data. That requires the use of *Memory Manager* functions. This seems to be the most straightforward solution. However, NI does not recommend using these functions if they can be avoided. The way how to avoid this is to code and compile own wrapper DLL above ADQAPI in C or C++, which would contain functions at a higher abstraction layer, which would include memory allocation/deallocation commands. This could be time-consuming and similarly challenging as using the *Memory Manager* functions in LabVIEW. The third option is to use the .NET assembly of ADQAPI, which can be called in LabVIEW. This path was explored, but poor performance was achieved, which limits real-time data processing. Also, it was not compatible with FWATD. Due to this obstacle, the Digitizer module was not fully implemented in the main software solution and the rapid scan experiments were done using a MATLAB script written by Oleksii Laguta.

The developed sample holders are equipped with a modulation coil that is not used in a frequency rapid scan for a field modulation, but to add an offset to the external magnetic field around a sample. This is done to acquire rapid scan EPR spectra when the field is set in the resonance, and background signal when it is out of the resonance conditions. The background signal is caused by the frequency-dependent behavior of all components in the path of the microwave signal. The modulation coil can under normal conditions sustain an electrical current of about 360 mA without significant heating (2 A is a short-term maximum), which in the case of the SSH creates a magnetic field of ~25 mT. Such magnetic field offset is in many cases sufficient to overcome spectral linewidth. But, because during an experiment the sample holder is partially thermally isolated (plastic body and a low pressure in VTI space), the direct current that flows through the coil slightly heats the whole sample holder and the sample and temperature would be different after the electrical current is turned ON and OFF. Because this would cause a change of conditions, it must be avoided. An easy solution is to just change the polarity of the electrical current. An additional advantage of this approach is that the double offset of the magnetic field is achieved. However, not all laboratory power supplies have a such feature. In our case, the source meter unit Keithley 2450 was used for this purpose. The source meter has triaxial output connectors at its rear panel. A pair of adapters and standard 50Ω coaxial cables were used for the connection of leads between the source meter and the probe head, which minimized external interference.

4 Solid state materials studied by HF-EPR

The solid-state paramagnetic species provides information about site symmetry, electronic configuration, and neighboring atoms. The complexity arises from anisotropies that needs to be included to the spin Hamiltonian to describe the spin system.

Among many applications of EPR is research of defects in solid state materials that has potential for improvement of quality assessment in semiconductor industry, progress in development of spintronic devices and quantum computing [5]. In further subsections of this chapter will be shown measured spectra of selected paramagnetic species in semiconductors obtained by the developed HFEPR FRaScan spectrometer. Other published results which includes data from the spectrometer are: EDMR spectra of nitrogen-doped 15R SiC, [72, 83], HFEPR spectra of SIMs based on Co(II) complexes [84, 85], EPR maps of copper acetate hydrate [86], FS-EPR spectra of ^{14}N-TEMPOL and CW-EPR spectra of iron(II) phthalocyanine (FePc) [71], rapid scan spectra of LiPc [35] and EPR maps of $Mn_{12}Ac$ [87], all of which were performed using the software developed in this thesis.

4.1 Qubits in SiC substrate

Silicon carbide occurs in nature very rarely as the mineral Moissanite (named after Henri Moissan who found it in a meteorite in 1905) [88]. However, it can be mass-produced and is commonly used as an abrasive in sandpaper and polishing agents for its hardness (~9.5 of Mosh). This is because of strong covalent bonds between atoms of carbon and silicon. As a semiconductor, the SiC has a wide bandgap which makes it transparent in the visible spectrum and shifts the threshold for dominance of intrinsic conductivity to higher temperatures. It also allows to production of electronic components with a high breakdown voltage compared to silicon. It also has a higher thermal conductivity and saturation drift velocity than silicon, which makes it superior for high-power and high-frequency electronics. However, its high melting temperature, mechanical hardness, and chemical resistance as well as undeveloped technological processes for mass production of high-quality crystals were a drawback for the wide application of electronic components based on SiC. in the last century. With technological advancement, SiC Schottky diodes and SiC MOSFETs became more common [88, 89].

Elementary building blocks of SiC crystals are tetragons made of Si atoms surrounded by four C atoms (and vice versa). These can form a variety of crystal structures (polytypes), that differ in a stacking sequence of close-packed spheres, where each plane of spheres represents a Si-C biplane (see Figure 43). Most commonly made are 3C, 4H, 6H, and 15R polytypes of SiC [88, 89]. Table 3 lists properties of SiC polytypes from Figure 43, and shows that each polytype has different properties. Several types of defects in the crystal lattice of the SiC introduce paramagnetic centers that can be considered as qubits. Applications of quantum systems based on the SiC are reviewed in this recently published paper [90].

Table 3: Comparison of properties for intrinsic Si and common polytypes of SiC [88, 89].

Property	Si	3C-SiC	4H-SiC	6H-SiC
Bandgap [eV]	1.11	2.39	3.26	3.02
Electron mobility [cm^{2}V^{-1}s^{-1}]	1 400	1 000	1 020	450
Hole mobility [cm^{2}V^{-1}s^{-1}]	600	100	120	100
Lattice constants [Å]	5.43	4.36	3.08 10.08	3.08 15.12
Melting point [°C]	1 410		~2 830	
Thermal conductivity [Wm^{-1}K^{-1}]	150	360	370	490

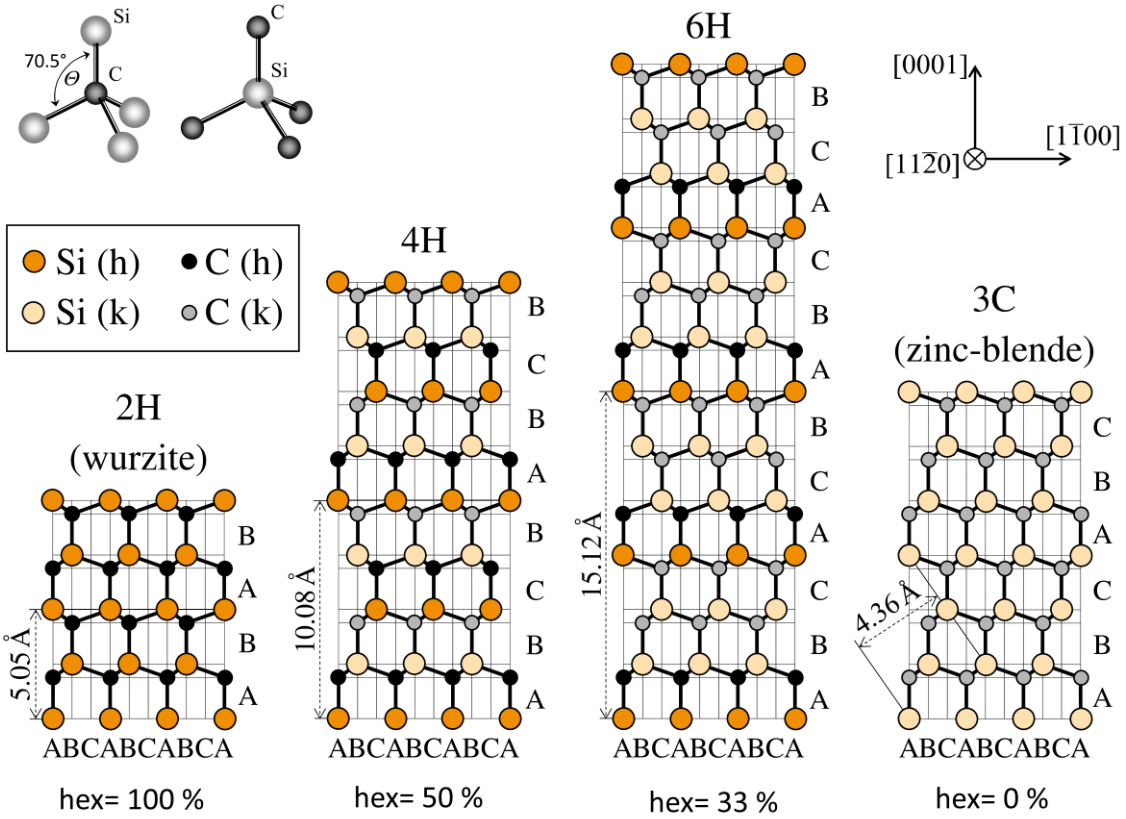

Figure 43: Elementary structure (tetrahedrons) and stacking sequences for several polytypes of SiC, with the ratio of hexagonal sites. Figure was taken and edited from [89].

4.2 HF-EPR study of SiC doped by Vanadium

In this chapter, HFEPR measurements and analysis of chosen crystal materials will be described. The first chosen sample is a 4H-SiC doped by Vanadium (SiC:V). The vanadium substitutes Si atoms in the SiC lattice in one of three charge states and behaves as an amphoteric impurity. In the charge state V^{4+} the vanadium acts neutral, while in V^{3+} and V^{5+} it acts as an acceptor or donor respectively [91]. Therefore, it compensates for residual impurities that are commonly present in grown SiC crystals, and its amphoteric behavior is used for the fabrication of semi-insulating substrates in high-power microwave electronics [92].

With the assumption that the residual impurity is for example a nitrogen (donor), the oxidation state of the vanadium dopant regardless of the site is V^{3+} with a spin $S = 1$ [92]. The vanadium then creates two inequivalent paramagnetic centers with different properties (listed in Table 4), one in the quasicubic site and the second in the hexagonal site of the SiC crystal. Spectra of the both paramagnetic centers will be split due to the zero-field interaction since S=1. Furthermore, the naturally predominant isotope 51V with a natural abundance of 99.75 % has nuclear spin $I = 7/2$, and therefore each EPR absorption peak displays $2I+1 = 8$ lines arising from the hyperfine splitting. This means that the four mentioned absorption peaks further split into 8 hyperfine lines. The EPR spectra of 4H-SiC:V then shall contain four groups of 8 lines, while the four groups originate from a zero-field splitting (D) and two possible lattice sites (hexagonal and quasicubic) [93]. To show how the CW-EPR spectra of 4H-SiC:V shall look, values in Table 4 were applied to the MATLAB script for simulation with EasySpin,

```
%% 4H Crystal SiC + V simulation script
HSys.S= [1]; % Hexagonal site, Spin S=1
HSys.g= [1.951 1.956]; % g-factor
HSys.Nucs= 'V'; % Vanadium nuclei
HSys.A= [172 174]; % Hyperfine coupling (MHz)
HSys.D= 2618;     % Zero-Field Splitting (MHz)
HSys.lwpp = [1 1]; % Gaussian and Lorentzian broadening (mT)
HSys.weight= 0.5; % relative to sample
CSys=HSys; % quasi-cubic site
CSys.g= [1.961 1.957];
CSys.A= [177 189];
CSys.D= 10528;
% Simulated experiment parameters
Exp.mwFreq = 349.9; % GHz
Exp.Range = [12275 13275]; % (mT)
Exp.CrystalOrientation = [0 0]*pi/180; % ° to rad
Exp.nPoints= 10000;
% CW spectra simulation for solid-state samples
pepper({HSys, CSys},Exp);
```

and the simulated CW-EPR spectrum is plotted on Figure 44.

Table 4: Spin system properties of paramagnetic centers in 4H-SiC:V, based on literature [93].

Spin system parameters	Hexagonal site		quasicubic site	
	‖c	⊥c	‖c	⊥c
g [-]	1.951	1.956	1.961	1.957
A [MHz]	172	174	177	189
D [MHz]	2618		10528 (4K)	

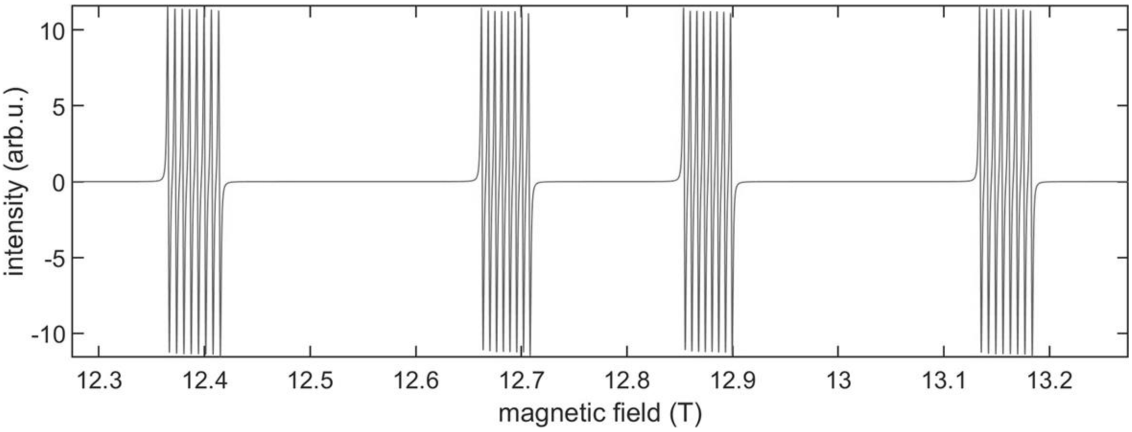

Figure 44: Simulation of CW-HFEPR spectra for 4H-SiC:V at 349.9 GHz. Made via the EasySpin [47] *by using values from the literature* [93].

Two samples of SiC:V (photo on Figure 45) were obtained from Jan Kunc from Charles University in Prague. Both samples were cut off from the same 4H-SiC wafer, with the concentration of V dopants estimated by secondary ion mass spectroscopy to $3{\cdot}10^{17}$ cm^{-3} [91]. Both samples have similar areas, therefore almost the same amount of paramagnetic V centers is expected. Sample A has a distinctive scratch in the right-bottom corner (other visible scratches are only on the mirror), and sample B has minor defects on its edges (especially in the left-bottom corner) that were made probably when crystals were cut from the wafer. These mechanical defects can manifest in crystal lattice defects which can form various paramagnetic species mostly originating from a dangling bond. However, these should be easily distinguished from the V centers. An isotope 51V has a natural abundance of 99.75 % and if the samples were not irradiated by high-energy particles, then the presence of other vanadium isotopes can be neglected in simulations and further analysis.

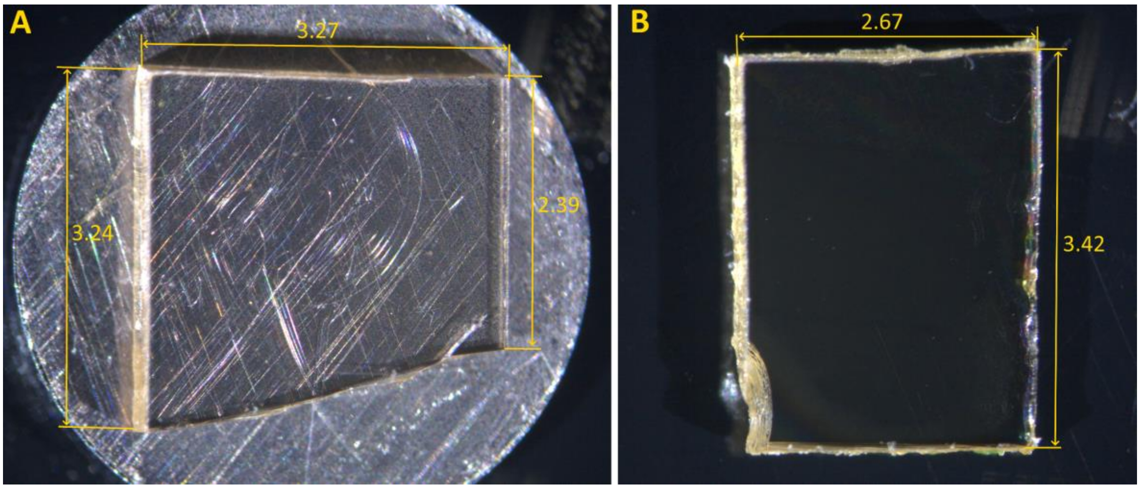

Figure 45: Two samples of 4H-SiC:V cut from a wafer. The sample A with area ~9.2 mm^2 is placed on a mirror, sample B with area ~9.1 mm^2 is in a sample box with black background.

To analyze the paramagnetic centers in the 4H-SiC: V by the built HFEPR FRaScan spectrometer, we will assume that the symmetry axis of the crystal lattice is parallel with the direction of the external magnetic field B_0. First, a series of CW-EPR measurements were performed on sample A. The sample was placed in the simple sample holder, without a heater, field sensor, and reference sample. Then the sample holder was mounted to a probe optimized for 400 GHz. The probe was inserted into the magnet and left to cool down the sample to about 16 K, while the VTI temperature was set to 5 K. Such a large difference in temperature between the sample and VTI was assigned to an insufficient flow of cooling helium that could not properly compensate for heat transferred from the probe head. Then CW-EPR spectra were obtained at 283.07 and 349.9 GHz at several temperature levels to check the behavior of the paramagnetic centers and if a signal from some other center will not appear in a spectrum. Above the temperature of 64 K, the saturation of the sample was no more observed. Later CW-EPR spectra were measured at 283.07, 316.5, and 349.9 GHz up to about 140 K to also have frequency-dependent data.

From these measurements, three representative spectra measured with microwave excitation at a frequency of 349.9 GHz are plotted in Figure 46. One shows how a saturation effect can distort spectra when a sample is at too low a temperature (35 K), the second shows corrected EPR spectra of 4H-SiC:V at 83 K, and the third shows that at a higher temperature (126 K) the intensity of the EPR signal may decline because of smaller population difference (see equation 12). All plotted spectra have a corrected intensity to equalize the level of noise. The noise was evaluated from a region 12.5–12.6 T. Also, a Hilbert transformation (Kramers-Kronig relationship) was used to correct a phase of the EPR signal.

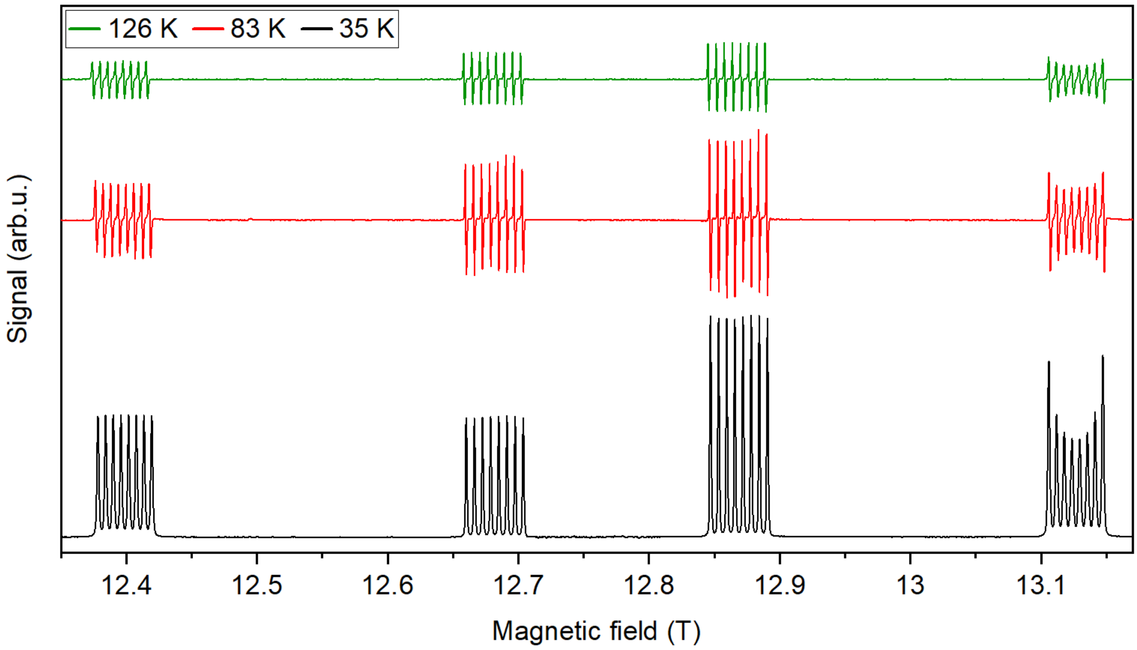

Figure 46: Temperature dependency of 4H-SiC:V CW-EPR spectra at 349.9 GHz. (ramp rate: 1 mT/s,modulation: 3 G at 10 kHz, low pass filter time constant: 150 ms, intensity was corrected based on noise level sampled at 12.5-12.6 T)

Further, frequency-dependent spectra at 65 K are shown in Figure 47, with the same correction done as for the temperature-dependent spectra. An apparent increase in the signal intensity at higher resonance frequencies is caused by a bigger difference in energy levels resulting in a larger difference in the population of states (equation 12 on page 8).

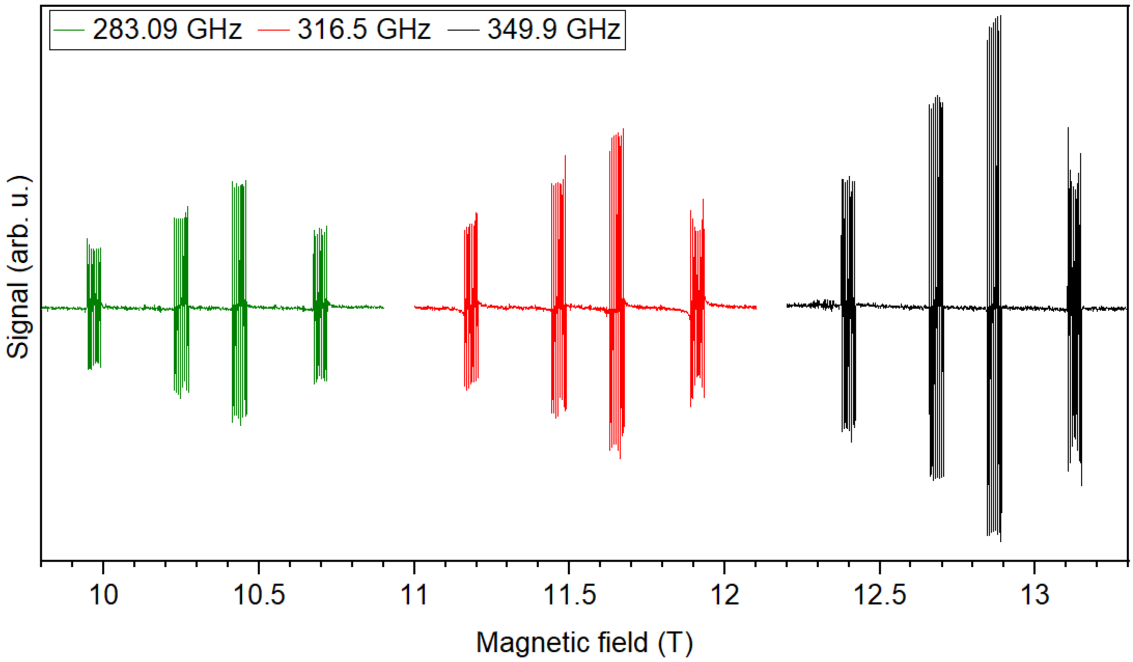

Figure 47: Frequency dependence of 4H-SiC: V CW-EPR spectra at 65 K. (Parameters are same as for temperature dependency on Figure 22. Intensity correction: 0.778: 1: 0.186)

4.3 FS-EPR measurements and EPR maps

2D-EPR mapping is a type of measurement that is performed to obtain EPR spectra in both field and frequency domains to make a Zeeman diagram. Data are then usually plotted in intensity color graphs where magnetic field and frequency are on the x- and y-axis respectively and signal intensity is represented by a color transition (z-axis). The advantage of this diagram is that EPR lines contrast from the background and directly show energy (proportional to microwave frequency) required for the transition of the spin system between states in increasing magnetic field. The g-factor can be then estimated simply from the slope of lines on the diagram. Also, some spin Hamiltonian parameters such as hyperfine splitting and zero-field splitting can be simply obtained from the dataset in the frequency domain.

The mapping can be performed by repeating CW measurements at several frequencies, however, if high resolution in the frequency domain is required, for example, to recover frequency domain spectra, such measurement may be time-demanding. If a single CW measurement takes about 5 minutes and the required resolution in the frequency domain is 2,000 points, then the whole measurement would take about one week. During this time, several parameters such as the temperature of the sample and microwave power must be kept stable, which can be technically challenging.

Another approach is to perform FS-EPR measurements for many steps of the magnetic field. The advantage of FS-EPR is that it can be performed much faster and the most limiting factor is then the time required to step the magnetic field. If the acquisition of averaged FS-EPR spectra with a single step in the magnetic field takes about 30 seconds, then the acquisition of 2 000 spectra dataset will take about 17 hours. However, FS-EPR spectra may contain artifacts from changes in phase and unstable baseline due to microwave power fluctuations. Also, there is a trade-off in measuring parameters (sweep rate, filter time constant) which results in lower SNR. On the other hand, SNR can be improved by averaging of several FS-EPR spectra. A background can be obtained by performing FS-EPR measurement at the magnetic field that is out of resonance and later subtracted from a spectrum to correct the baseline. Microwave power fluctuation can be partially corrected, if the frequency profile of whole terahertz components (sources, detectors, and quasi-optics) is known. Even though, a worse SNR and presence of some minor artifacts can be expected in FS-EPR in comparison to CW-EPR. The presence of noise can be well demonstrated by comparing measured CW-EPR spectra and recovered CW-EPR spectra from the 2D-EPR map.

At last, it is possible to continuously acquire fast FS-EPR spectra while the magnetic field is slowly swept. It is similar to the previous approach, but the magnetic field is not steady, therefore if the frequency sweep takes about 1 second, and the field is swept by 1 mT/s, then the field change during a single scan is 1 mT. In some cases, this can be more than the width of the EPR line, and recovered CW-EPR spectra may not contain important details. However, obtaining data from 2 000 frequency scans will take only about 33 minutes, and will cover a magnetic field region of about 2 T. Also, a precalculated number of scans will be just approximate because of lag at the start and end of the magnetic field sweep. It is a good practice to set the field range to start and end far enough from resonance for a whole range of the frequency sweep. Then the EPR signal is detected only in linear regions of the magnetic field sweep, and nonlinear regions can be omitted. Also, FS-EPR data from regions that do not contain EPR spectral lines can be averaged to get a background pattern of a 2D-EPR map, which can be subtracted in post-processing. However, the background pattern at the start (b_s) and the end (b_e) border of the magnetic field sweep slightly changes. Therefore, subtracting only *bs* from the whole 2D-EPR map (first half of equation 26) would leave a residual background with increasing intensity in the direction region of b_e. Therefore, an increasing difference of b_s and b_e (second half of equation 26), needs to be added to the 2D-EPR map. To subtract the background from the whole dataset of a 2D-EPR map, the following equation can be applied to individual FS-EPR spectra:

$$s_c(i) = s_o(i) - b_s + \left(\frac{i}{n}\right) \cdot (b_s - b_e) \tag{26}$$

where s_c is the corrected signal, s_o is the original signal, b_s and b_e are the backgrounds at the start and end respectively in the dataset, i is the iterator through field domain, n is the total number of FS-EPR scans.

Two examples of 2D-EPR maps are in Figure 48 and Figure 49. Both were obtained by stacking non-averaged FS-EPR spectra during a continuous field sweep. First, the map in Figure 48-A was acquired with parameters in Table 5. Second, a data decimation with averaging of in frequency domain was done to reduce the size of the dataset to 3 048 × 6 000 points. Third, background correction was done following equation 26. Data were then imported to OriginPro 2020b as a matrix and plotted as a 2D image plot with a thermometer color scale for intensity. At last, in the photographic editor contrast and color saturation were increased on the image plot to make EPR signals more visible. The map was done in a relatively broad range, to cover whole spectra in both frequency and magnetic field domain. Despite the fact that the magnetic field ramp rate was set to the lowest possible by the current hardware, ~0.18 mT/s, the resulting number of scans was too low and CW-EPR spectra could not be recovered in sufficient quality. There were also regions in which was not possible to distinguish all peaks from the FS-EPR spectra and faster frequency sweeps would lead to limiting parameters which would result in poor SNR. Anyway, it was possible to extract partial FS-EPR spectra (marked by colored dot lines in Figure 48-A) for each set of lines with were centered around 288 GHz (Figure 48-C) and 307.5 GHz (Figure 48-B). These spectra were used for the determination of the spin system parameters such as a g-factor, a hyperfine coupling A, and a zero-field coefficient D for both quasicubic and hexagonal sites in the 4H-SiC lattice. The g values were determined from the slope of lines in the map by applying equation (4). The A values were obtained as the mean interval between lines in each line group (width of line set divided by seven). The *D* values could be also determined from the FS-EPR spectra as the difference of frequencies at the center of line groups assigned to the same paramagnetic center (crystal lattice site).

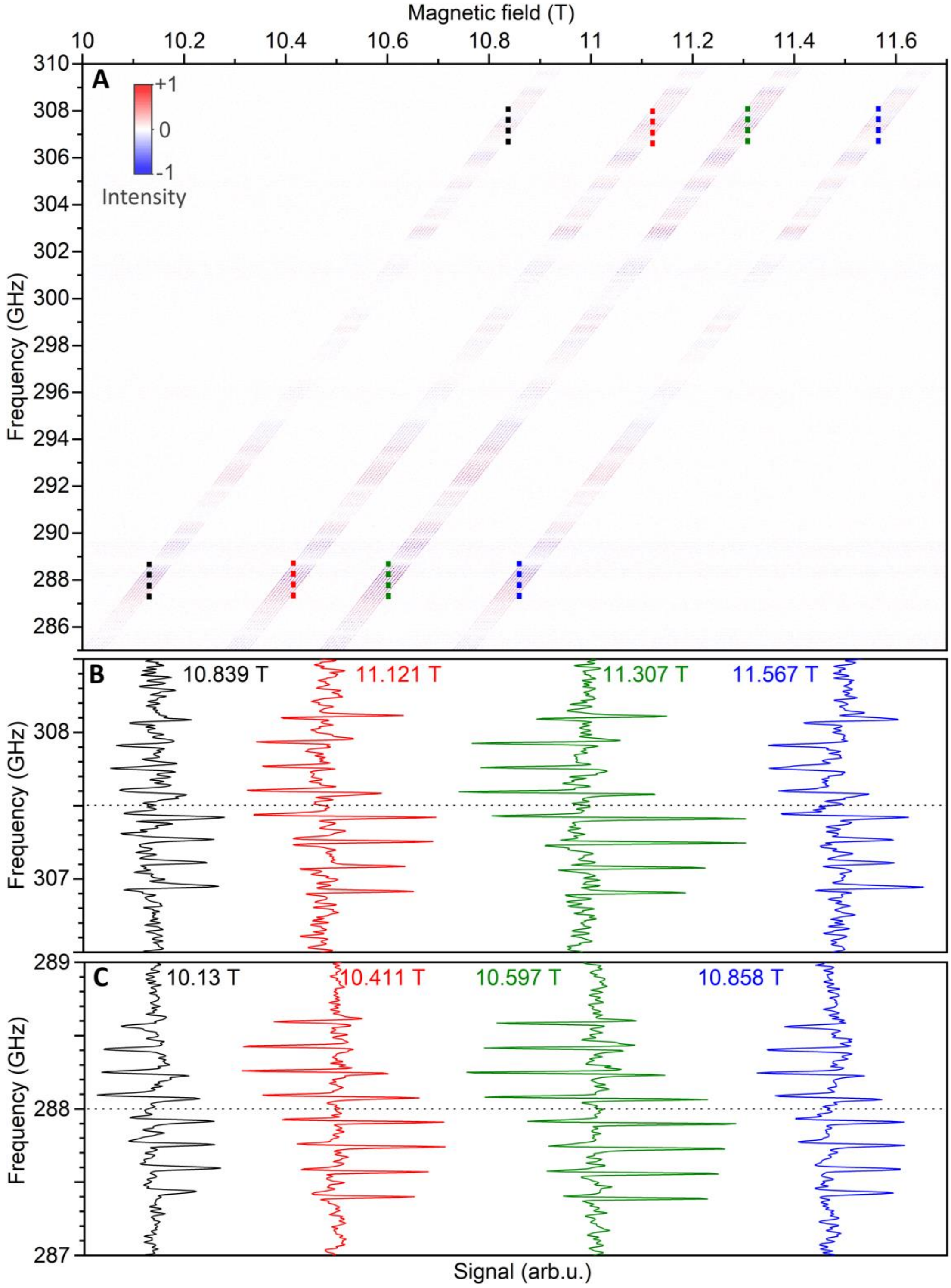

Figure 48: A) Broad 2D-EPR map of 4H-SiC:V. Doted colored lines denotes position of extracted particular FS-EPR spectra. B) Particular FS-EPR spectra for each set of lines that were centred at 307.5 GHz. C) Particular FS-EPR spectra for each set of lines that were centred at 288 GHz.

Table 5:Parameters for acquisition of 2D-EPR map in relatively broad range.

Frequency range	282 – 312 GHz	Field range	9.5 – 12 T
Sweep rate	7.3242 GHz/s	Ramp rate	0.17893 mT/s
Modulation frequency	6 kHz	Modulation amplitude	~ 3 G
Low-pass filter constant	~ 0.25 ms	Sample temperature	~ 80 K
FS-EPR record length	60 000 points	Number of scans	3048

A similar procedure was followed to make a map in Figure 49-A but in this case, the map has a much higher resolution in the magnetic field domain (4779 points). It was achieved by a shorter frequency sweep in a narrower range, while the magnetic field ramp rate was set as low as the power supply for the magnet allowed (0.1789 mT/s). There were enough data points to recover CW-EPR spectra of sufficient quality for further analysis. Two spectra were recovered from the frequencies 292.14 and 294.26 GHz, and plotted in Figure 49-B. In Table 7 and parameters were compared with values found in literature [93]. These values are different since we don’t know the exact orientation of the studied crystal in the magnetic field.

Table 6: Parameters for acquisition of 2D-EPR map in relatively narrow range.

Frequency range	292 – 294.5 GHz	Field range	10 – 11.3 T
Sweep rate	2.4414 GHz/s	Ramp rate	0.17893 mT/s
Modulation frequency	6 kHz	Modulation amplitude	~ 2.5 G
Low-pass filter constant	~ 4.1 ms	Sample temperature	~ 81 K
FS-EPR record length	15 000 points	Number of scans	4779

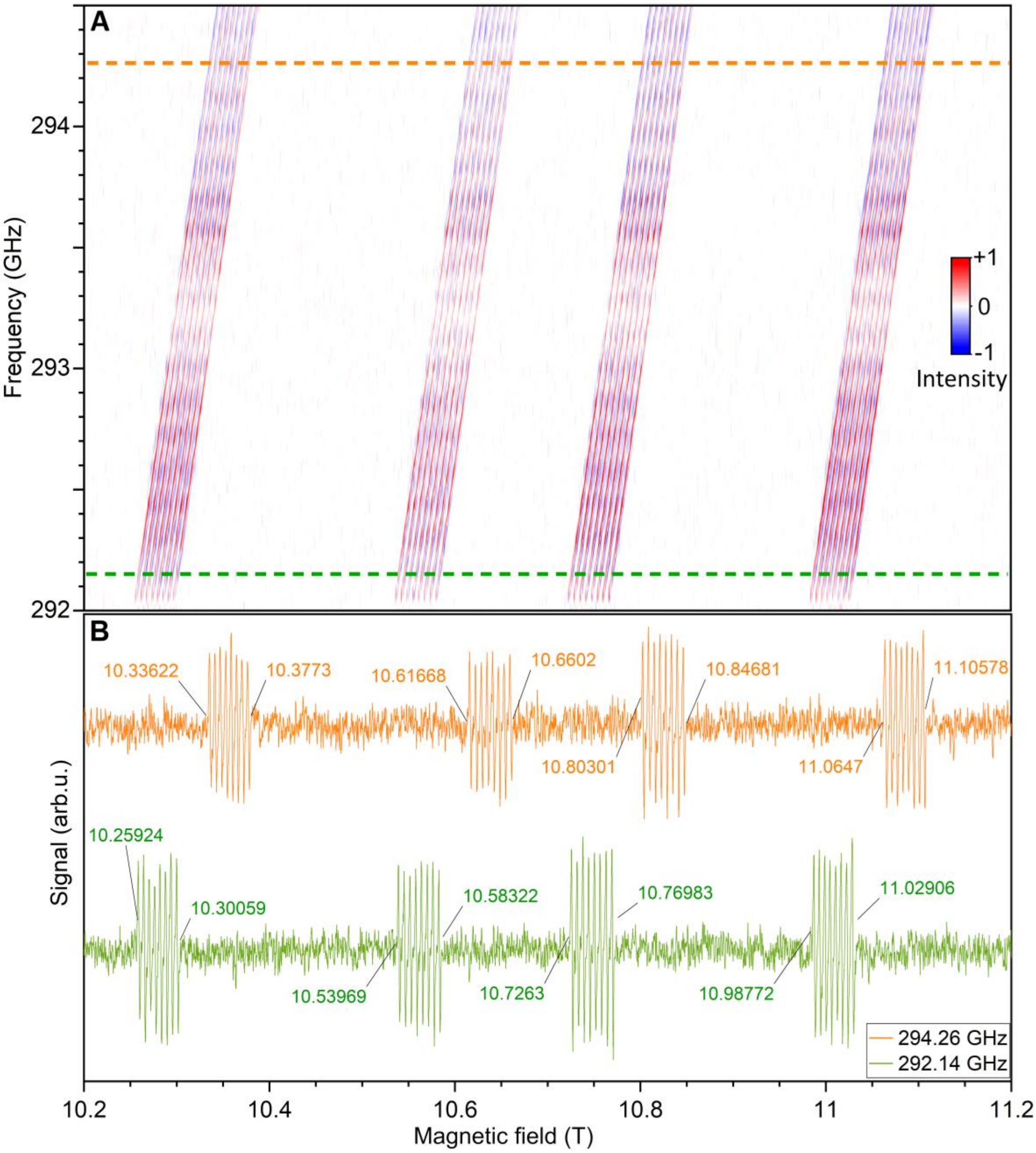

Figure 49: A) 2D-EPR made of 4779 FS-EPR scans at rate 2.44 GHz/s during continuous field sweep at rate 0.179 mT/s. Filter constant 4ms, modulation frequency 6 kHz, modulation amplitude 2.5 G, datapoints in frequency domain - 15 000, 81 K. B) Extracted CW spectra from the map.

Table 7: Spin system parameters of 4H-SiC obtained from a literature, CW measurements, FS-EPR spectra from map on figure 25, and CW recovered from map on figure 26.

Lattice site	Source	$g_\parallel$ [-]	$g_\perp$ [-]	D_{tot} [MHz]	$A_\parallel$ [MHz]	$A_\perp$ [MHz]
Quasicubic	Lit	1.961	1.957	10385	177	189
	Map 1	1.9651		20023	161.96	
	Map 2	1.97102		20096	162.4	
	CW	1.95885		20006	161.2364	
Hexagonal	Lit	1.951	1.956	2618	172	174
	Map 1	1.9623		5108	171.25	
	Map 2	1.9693		5142	171.66	
	CW	1.95692		5117	170.2	

4.4 Rotation measurements

By rotating crystals in the magnetic field, the anisotropic behavior of the EPR spectra of paramagnetic species can be studied. Attempt to do this with 4H-SiC: V unfortunately did not bring satisfying results. The EPR signals were too low in intensity to resolve and distinguish from a background. Moreover, at such low temperatures (~65 K), other signals appeared either from contamination, trapped air bubbles, or defects in the sapphire rod of the rotator.

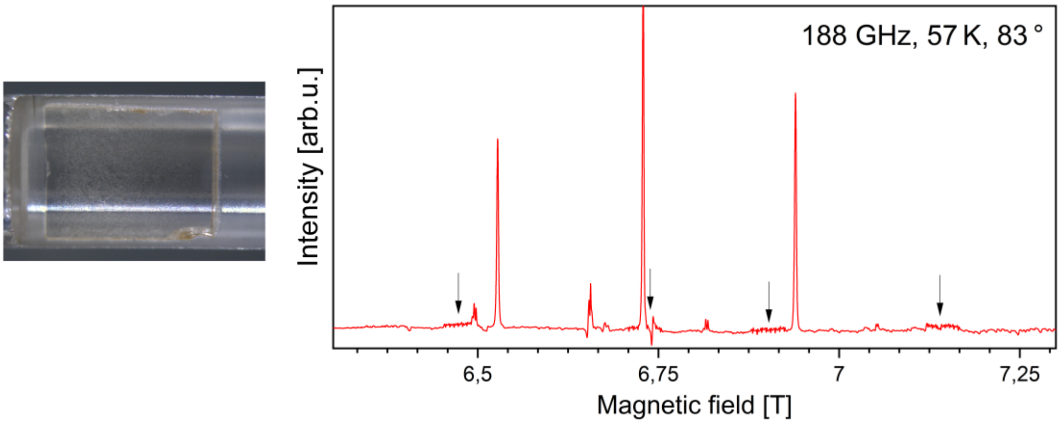

Figure 50: Sample of SiC:V mounted to the rod of the rotator (left), and its CW-EPR spectra (right). The EPR lines which subject of interest has much lower intensity than unwanted signals from some impurities.

For this reason, it was decided to provide an example of the sample of lithium phthalocyanine (LiPc) at room temperature. The sample is a needle-shaped crystal, and the axis of symmetry is the long axis of needles. Its applications include medical and biomolecular research fields such as EPR imaging, where it is used as an oxygen probe for a tumor. LiPc is a molecule that possesses one unpaired electron, resulting in a radical with a spin of $S = 1/2$ and displays weak anisotropy [94–96]. By rotation of LiPc crystal in the magnetic field and measuring the EPR spectra, the g tensor parallel and perpendicular to the long axes of the crystal was determined. The sample was placed in the rotator equipped with the Teflon rod, perpendicular to the axis of rotation. This way the crystal sample can change its orientation from perpendicular to parallel towards the direction of external magnetic field B_0 by 90° rotation. However, for sufficiently precise measurement, several spectra with a small angular step need to be obtained. Doing this in CW mode would be time-consuming. Instead, we used the FS-EPR to obtain 321 spectra with a step of 1° rotation.

Table 8: Parameters for FS-EPR rotational map measuremnts of LiPc crystal.

Frequency sweep range	216.05 – 216.15 [GHz]	Static magnetic field	7.7 T
Sweep time	1.024 s	VTI temperature	280 K
Modulation frequency	10 kHz	Modulation amplitude	~ 0.1 G
Low-pass filter constant	~ 0.1 ms	Record length	15 000 points
Averaging	4 scans	Rotator range	2 – 322 °
Rotator step	1°	Delay between step	3 s

All obtained spectra were processed in OriginPro software [97] and assembled into an FS-EPR rotational map plotted in Figure 51. The data were fit with parameters $g_{\perp}= 2.00529$ and $g_{\parallel}= 2.00533$ via angular-dependent simulation in EasySpin [47]. However, this result may vary from values in the literature [94, 98], because of the relatively large instrumental uncertainty of the used superconducting magnet (~15 mT).

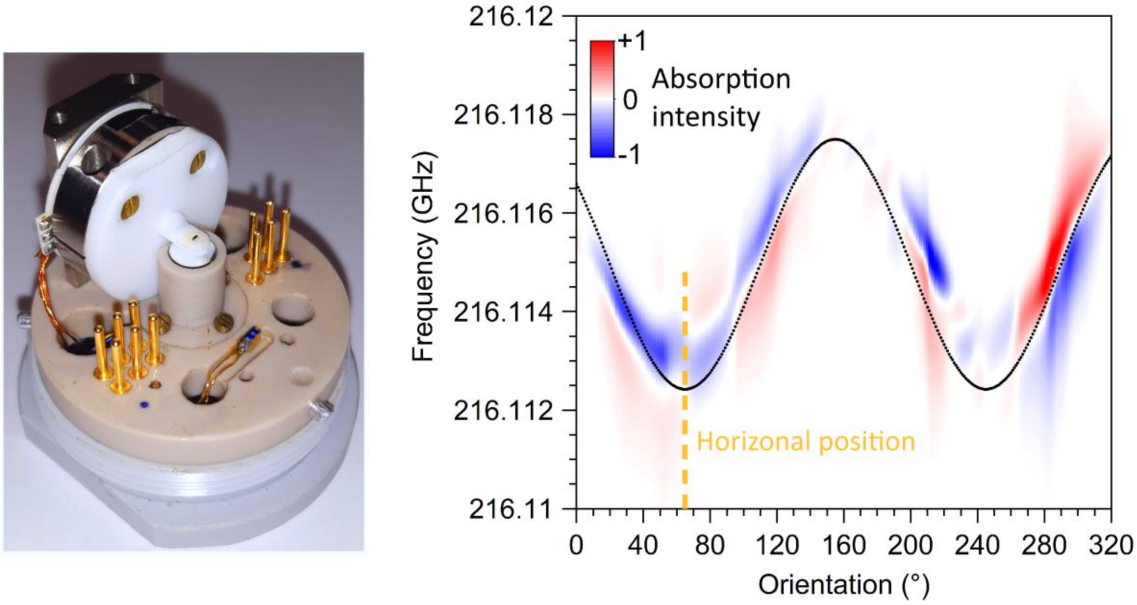

Figure 51: Left - Rotator sample holder with LiPc crystal placed on PTFE rod. Right - Rotational map made of 321 FS-EPR spectra, by 1° step. Measured at room temperature and magnetic field of 7.7 T. Orange dashed line denotes a position in which crystal axis is parallel to XY-plane and perpendicular to magnetic field (~65 °). Published in [99].

4.5 FRaScan measurements

To test the FRaScan capabilities of the spectrometer a trial measurement on a crystal sample of 1,3-bisdiphenylene-2-phenylallyl (BDPA) was performed. The BDPA is commonly used in EPR spectroscopy as a molecular standard, and its g-factor is ~2.003 [100].

To generate frequency scans, we used APVSG20 and the AMCs with the multiplication factor 9. The scan range was 100.5 – 101.3 GHz, and the rate was 0.4 MHz/ns (400 THz/s ≈ 14.27 MT/s). The period of the scans was 2 μs. The magnetic field was set to ~3.6 T, and the temperature of the sample to 70 K. The digitizer was set to acquire 40 000 samples at a rate of 10 GS/s (two sweep periods) and perform 250 000 averages (accumulations). The data acquisition took about 1 second. On the left side of Figure 52 is plotted a portion of data that contains the rapid scan signal along with the background signal that was recorded when the magnetic field was shifted out of the resonance. On the right side is just the rapid scan signal cleared of the background by subtraction. The maxima of each oscillation in the rapid scan spectrum were fitted by an exponential function and from the signal decay a relaxation time of $T_2^*\approx 27.6$ ns was estimated. From the intensity of the first peak and standard deviation of the signal in the 600–700 ns region was estimated the SNR of ~1096.

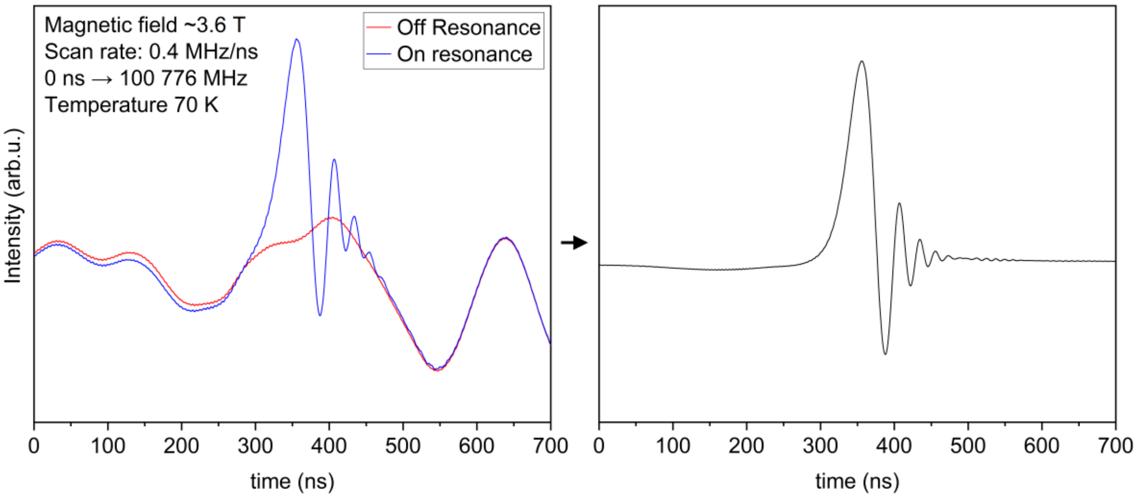

Figure 52: FRaScan performed on crystal of BDPA at temperature of 70 K. On the left side is raw acquiered spectra (on resonance) and its bacground (off resonace. On the right side is the FRaScan spectra clean of the bacground.

Conclusion

The electron paramagnetic resonance spectroscopy was presented in the Introduction as a scientific method for the examination of materials via the interaction of electromagnetic waves with the magnetic dipole momentum of unpaired electrons. It has numerous applications in research and industry. The effective spin Hamiltonian and the Bloch equations were presented in subchapter 1.1 as tools for a mathematical description of the electron paramagnetic resonance phenomenon.

Further, the technical aspects of electron paramagnetic spectroscopy were explained in subchapter 1.2. A function of the main parts of common spectrometers was discussed, especially microwave source, waveguides, resonance cavity, electromagnet, microwave detector, and a lock-in amplifier. Currently are preferred microwave sources based on solid-state oscillators. In a traditional continuous wave EPR setup, the microwaves travel through waveguides into the resonance cavity, where they interact with the sample, and changes in microwave power due to the EPR are detected. A commonly used microwave detector is a Schottky barrier diode. The signal-to-noise ratio can be significantly improved by using a phase-sensitive detection via modulation of magnetic field and processing of detected signal by a lock-in amplifier. Pulse EPR methods can decouple certain interactions to observe only desired effects. They also allow us to study relaxation processes. However, they are technically (and financially) more demanding, limited by their narrowband nature, and in some cases slower than CW-EPR methods. They also cannot be used when the relaxation time is shorter than the dead time of the instrument.

To overcome the limitations of the pulsed and continuous wave techniques, a novel broadband HFEPR spectrometer was developed to implement a frequency rapid scan method. It is well described in chapter 3. The spectrometer uses a cryogen-free superconducting magnet that can create a vertically oriented magnetic field of up to 16 T of positive and negative polarity. The Cryostat of the magnet is equipped with a variable temperature insertion (VTI) that allows to control temperature of a sample down to ~2 K. Besides this, the sub-terahertz sources composed of microwave synthesizers and several combinations of frequency multipliers can generate signals in the overall range of about 82 – 1100 GHz. The synthesizers can operate in the continuous wave mode, and in the frequency sweep mode with a triangle profile. This allows the acquisition of frequency and temperature-dependent CW-HFEPR spectrum, as well as the FS-HFEPR spectra. By performing the frequency sweeps while the magnet is ramped, it is possible to acquire 2D-EPR maps for accelerated characterization of a paramagnetic species, which would be too time-consuming if it needs to be done by a CW-EPR. A pair of mixers was used for heterodyne detection of (sub)terahertz waves. A broadband operation of the spectrometer is supported by a quasi-optical system that passively controls polarization of (sub)terahertz waves, refocus, and guides them to the sample and consequently to detectors. For positioning of the quasi-optical system in longitudinal, lateral, and vertical (x, y, z) axis, a servomotor system was implemented. The usability of the spectrometer is further extended by the developed sample holders described in subchapter 3.2. With them, the spectrometer can perform EPR measurements on solid-state samples including powders pressed into pellets, liquid samples, and crystal samples with the possibility to rotate them in a single axis perpendicular to the magnetic field. For implementation of the frequency rapid scan method, the spectrometer was additionally equipped with a fast digitizer and vector signal generator.

To control experiments with a computer, custom-made software was developed in LabVIEW, which was the one of essential tasks for this thesis. The software solution has a modular architecture based on a queued message handler and state-machine design patterns. The submodules encapsulate application-specific logic for independent control of certain subsystems of the spectrometer's hardware. They react to the state of the subsystem and commands from a higher layer. Above them is a supervising module that handles interaction with users and communicates with each submodule. It also manages automated measurement procedures. Currently, the software solution can control each key subsystem and do automated CW-EPR and FS-EPR measurements, and 2D-EPR mapping. Further explanation of the software implementation is in subchapter 3.4. The frequency rapid scan was not yet implemented in the main software due to compatibility issues of higher-level languages with the API of the digitizer, which are discussed at the end of the subchapter 3.5. However, several workarounds were explored. The suggested solution seems to be in using of the low-level LabVIEW Manager functions.

Functionality of the spectrometer was demonstrated on several measurements shown in chapter 4. The first measured sample was a semiconductor material the 4H polytype of silicon carbide doped by vanadium. The vanadium introduces a paramagnetic center that has the potential to be used as a qubit. On the results of measurements of this sample, we showed the capability of the spectrometer to perform automated temperature-dependent and multifrequency CW measurements. Further, the sample was characterized via 2D-EPR mapping while it was still in the simple sample holder. From the analyzed data and simulation based on parameters found in the literature, we assume that the principal axis of the crystal was slightly off the axis of the magnetic field. Unfortunately, the spectra obtained when the sample was placed in the rotator sample holder could not be analyzed, because the signal could not be recognized from peaks of unknown origin. Instead, a collection of frequency-swept spectra of LiPc crystal was obtained, when the crystal was step-by-step rotated in the magnetic field, to demonstrate the functionality of the rotator sample holder. In the subchapter 4.5 is shown frequency rapid scan spectrum of BDPA crystal, which was obtained by using the vector signal generator. From the decay rate of the signal, we estimated $T2^*\approx 27.6$ ns which suggests that microwave synthesizers would not be able to generate a sufficiently fast sweep.

The outcomes demonstrate the successful implementation of the FRaScan HFEPR spectrometer. It allows to study of a broad variety of samples, via the conventional CW-EPR method at multiple frequencies at hundreds of gigahertz, and under controlled conditions. It also implements the FS-EPR and a novel frequency rapid scan method. The data produced by the spectrometer has already influenced multiple publications [35, 71, 72, 76, 83–87], with more about to come. The developed software was reported in the Journal of Magnetic Resonance [99]. Automation of measurements significantly decreases the amount of time that would be otherwise spent by the operator performing experiments. The source code of the software is publicly available via the GitHub repository at https://github.com/MatSevy/CEITEC-HFEPR-spectrometer-LV under a GNU GPL v3 license. Other researchers (not only from the EPR community) can download it, modify its source code for their needs, or just take inspiration from it. However, there are still many possibilities to improve the spectrometer in terms of hardware and software.

On the hardware side, there is still some room to improve the sample holders. For example, the simple sample holder currently cannot use a local heater and magnetic field sensor at the same time. A simple solution for this is to extend its connector by one pair of contacts. The use of different materials could help distribute heat from the heater to the sample while keeping the sample holder thermally isolated from the probe. The rotator sample holder suffers from a significant drop in the signal which could be improved by redesigning its waveguide. Also, different materials for the shaft should be tried. In the carousel sample holder, the encoded needs to be debugged. Improved airflow around the digitizer in the PXIe chassis can reduce its temperature and extend its life.

On the software side, the architecture of the software can be further improved by the insertion of an intermediate abstraction layer to submodules, and the division of the supervising module into multiple entities. To simplify the implementation of new features and extensions, the application of object-oriented programming should be considered. Submodules for lock-in amplifiers, and magnetic field sensors can be further improved. Also, a submodule for carousel sample holder control needs to be implemented into the main software. Also monitoring the compressor's operation and UPS state should be added. The software for the FRaScan HFEPR spectrometer could be extended to support also the FTIR spectrometer. The submodule for the digitizer will first require a proper driver that shall be done as a collection of wrapper VIs above ADQAPI.dll, while some VIs will need to be modified by a low-level LabVIEW Manager function. Also, a new module for the signal generator needs to be implemented, to be able to generate faster frequency sweeps with a custom sweep profile.

Literature references

[1] RANGUELOVA, Kalina. *EPR-The „workhorse technique" that is still enabling scientists to break new ground after 70+ years* [online]. 2017 [vid. 2022-12-27]. Dostupné z: https://www.europeanpharmaceuticalreview.com/wp-content/uploads/BBS.R.098-EPR-Whitepaper_LayoutFULL-1.pdf

[2] RALPH T. WEBER. *Modern EPR Applications From Beer to DEER* [online]. Rheinstetten (Germany): Bruker BioSpin Corp. EPR Division. 2011 [vid. 2022-12-27]. Dostupné z: https://www.cif.iastate.edu/sites/default/files/uploads/EPR/ModernEPRapps.pdf

[3] EPEL, Boris, Gage REDLER a Howard J. HALPERN. How in vivo epr measures and images oxygen. *Advances in Experimental Medicine and Biology* [online]. 2014, **812**, 113–119 [vid. 2022-12-27]. ISSN 22148019. Dostupné z: doi:10.1007/978-1-4939-0620-8_15/COVER

[4] SATHIYA, M., J. B. LERICHE, E. SALAGER, D. GOURIER, J. M. TARASCON a H. VEZIN. Electron paramagnetic resonance imaging for real-time monitoring of Li-ion batteries. *Nature Communications 2015 6:1* [online]. 2015, **6**(1), 1–7 [vid. 2022-12-27]. ISSN 2041-1723. Dostupné z: doi:10.1038/ncomms7276

[5] LIU, Junjie, Valentin LAGUTA, Katherine INZANI, Weichuan HUANG, Sujit DAS, Ruchira CHATTERJEE, Evan SHERIDAN, Sinéad M. GRIFFIN, Arzhang ARDAVAN a Ramamoorthy RAMESH. Coherent electric field manipulation of Fe3+ spins in PbTiO3. *Science Advances* [online]. 2021, **7**(10), 1–8. ISSN 23752548. Dostupné z: doi:10.1126/sciadv.abf8103

[6] PRIVITERA, Alberto, Ross WARREN, Giacomo LONDI, Pascal KAIENBURG, Junjie LIU, Andreas SPERLICH, Andreas E. LAURITZEN, Oliver THIMM, Arzhang ARDAVAN, David BELJONNE a Moritz RIEDE. Electron spin as fingerprint for charge generation and transport in doped organic semiconductors. *Journal of Materials Chemistry C* [online]. 2021, **9**(8), 2944–2954. ISSN 20507526. Dostupné z: doi:10.1039/d0tc06097f

[7] ASTAKHOV, Oleksandr, Lihong XIAO, Friedhelm FINGER, Tao CHEN, Matthias FEHR, Benjamin GEORGE, Alexander SCHNEGG, Klaus LIPS a Christian TEUTLOFF. Multifrequency EPR study of HWCVD μc-SiC:H for photovoltaic applications. *physica status solidi (a)* [online]. 2016, **213**(7), 1747–1750 [vid. 2022-12-27]. ISSN 1862-6319. Dostupné z: doi:10.1002/PSSA.201533027

[8] CICCULLO, Francesca, Mathias GLASER, Marie S. SÄTTELE, Samuel LENZ, Petr NEUGEBAUER, Yvonne RECHKEMMER, Joris VAN SLAGEREN a M. Benedetta CASU. Thin film properties and stability of a potential molecular

quantum bit based on copper(II). *Journal of Materials Chemistry C* [online]. 2018, **6**(30), 8028–8034 [vid. 2022-12-27]. ISSN 2050-7534. Dostupné z: doi:10.1039/C8TC02610F

[9] GOPHANE, Dnyaneshwar B., Burkhard ENDEWARD, Thomas F. PRISNER a Snorri Th SIGURDSSON. A semi-rigid isoindoline-derived nitroxide spin label for RNA. *Organic & Biomolecular Chemistry* [online]. 2018, **16**(5), 816–824 [vid. 2022-12-27]. ISSN 1477-0539. Dostupné z: doi:10.1039/C7OB02870A

[10] ZHANG, Peng, Mauro PERFETTI, Michal KERN, Philipp P. HALLMEN, Liviu UNGUR, Samuel LENZ, Mark R. RINGENBERG, Wolfgang FREY, Hermann STOLL, Guntram RAUHUT a Joris VAN SLAGEREN. Exchange coupling and single molecule magnetism in redox-active tetraoxolene-bridged dilanthanide complexes. *Chemical Science* [online]. 2018, **9**(5), 1221–1230 [vid. 2022-12-27]. ISSN 2041-6539. Dostupné z: doi:10.1039/C7SC04873D

[11] SALIKHOV, K. M. a N. E. ZAVOISKAYA. Zavoisky and the discovery of EPR. *Resonance* [online]. 2015, **20**(11), 963–968 [vid. 2022-12-27]. ISSN 0973712X. Dostupné z: doi:10.1007/S12045-015-0264-6/METRICS

[12] BAKER, Michael. Brebis Bleaney. *Physics Today* [online]. 2007, **60**(3), 80 [vid. 2022-12-27]. ISSN 0031-9228. Dostupné z: doi:10.1063/1.2718768

[13] PRISNER, T. F., S. UN a R. G. GRIFFIN. Pulsed ESR at 140 GHz. *Israel Journal of Chemistry* [online]. 1992, **32**(2–3), 357–363 [vid. 2023-11-27]. ISSN 1869-5868. Dostupné z: doi:10.1002/IJCH.199200042

[14] GHIM, Barnard T., Jing Long DU, Susanne PFENNINGER, George A. RINARD, Richard W. QUINE, Sandra S. EATON a Gareth R. EATON. Multifrequency electron paramagnetic resonance of irradiated l-alanine. *Applied Radiation and Isotopes* [online]. 1996, **47**(11–12), 1235–1239 [vid. 2023-11-27]. ISSN 0969-8043. Dostupné z: doi:10.1016/S0969-8043(96)00037-1

[15] SCHLECKER, Benedikt, Alexander HOFFMANN, Anh CHU, Maurits ORTMANNS, Klaus LIPS a Jens ANDERS. Towards Low-Cost, High-Sensitivity Point-of-Care Diagnostics Using VCO-Based ESR-on-a-Chip Detectors. *IEEE Sensors Journal* [online]. 2019, **19**(20), 8995–9003 [vid. 2023-11-23]. ISSN 15581748. Dostupné z: doi:10.1109/JSEN.2018.2875767

[16] JOSHI, Janhavi P., John R. BALLARD, George A. RINARD, Richard W. QUINE, Sandra S. EATON a Gareth R. EATON. Rapid-scan EPR with triangular scans and fourier deconvolution to recover the slow-scan spectrum. *Journal of Magnetic Resonance* [online]. 2005, **175**(1), 44–51 [vid. 2022-10-20]. ISSN 1090-7807. Dostupné z: doi:10.1016/J.JMR.2005.03.013

[17] WEIL, John A. a James R. BOLTON. *Electron Paramagnetic Resonance: Elementary Theory and Practical Applications, Second Edition* [online]. B.m.: Wiley-Interscience, 2006. ISBN 9780471754961. Dostupné z: doi:10.1002/9780470084984

[18] WEBER, Y. Ralph. An EPR Primer. In: *Xenon User's Guide* [online]. Billerica (MA): Bruker BioSpin Corporation, 2011 [vid. 2022-12-27]. Dostupné z: https://www.cif.iastate.edu/sites/default/files/uploads/EPR/CW%20EPR%20Primer(XenonSoftware).pdf

[19] EATON, Gareth R., Sandra S. EATON, David P. BARR a Ralph T. WEBER. *Quantitative EPR* [online]. 1. vyd. Viena: Springer, 2010 [vid. 2022-12-27]. ISBN 9783211929476. Dostupné z: doi:10.1007/978-3-211-92948-3/COVER

[20] MAO, S., A. MERAKI, R. E. BOLTNEV, V. V. KHMELENKO a D. M. LEE. Percolation in aggregates of nanoclusters immersed in superfluid helium. *Physical Review B - Condensed Matter and Materials Physics* [online]. 2014, **89**(14), 144301 [vid. 2023-11-30]. ISSN 1550235X. Dostupné z: doi:10.1103/PHYSREVB.89.144301/FIGURES/8/MEDIUM

[21] DUIN, Evert. Basic EPR Theory. In: *Electron Paramagnetic Resonance Theory (course manual)* [online]. nedatováno [vid. 2022-12-27], s. 1–42. Dostupné z: https://webhome.auburn.edu/~duinedu/epr/1_theory.pdf

[22] MISRA, Sushil K. *Multifrequency Electron Paramagnetic Resonance: Theory and Applications* [online]. B.m.: Wiley-VCH, 2011 [vid. 2022-12-27]. ISBN 9783527407798. Dostupné z: doi:10.1002/9783527633531

[23] SCHWEIGER, Arthur a Gunnar JESCHKE. *Principles of pulse electron paramagnetic resonance*. Oxford: Oxford University Press, 2001. ISBN 9780198506348.

[24] WILTSE, James C. Corrections to published curves for atmospheric attenuation in the 10 to 1000 GHz region. *IEEE Antennas and Propagation Society, AP-S International Symposium (Digest)* [online]. 1997, **4**, 2580–2583 [vid. 2022-12-28]. ISSN 02724693. Dostupné z: doi:10.1109/APS.1997.625531

[25] DUIN, Evert. Practical Aspects . In: *lectron Paramagnetic Resonance Theory* [online]. Auburn (AL): Auburn University, nedatováno [vid. 2022-12-28]. Dostupné z: https://webhome.auburn.edu/~duinedu/epr/2_pracaspects.pdf

[26] HRUSZOWIEC, Mariusz, Kacper NOWAK, Bogusław SZLACHETKO, Michał GRZELCZAK, Wojciech CZARCZYŃSKI, Edward F PLIŃSKI a Tadeusz WIĘCKOWSKI. The Microwave Sources for EPR Spectroscopy. *Journal of Telecommunications and Information Technology* [online]. 2017, **2**, 18–25 [vid. 2022-12-28]. Dostupné z: https://www.itl.waw.pl/czasopisma/JTIT/2017/2/18.pdf

[27] CHARLES P. POOLE. *Electron spin resonance: a comprehensive treatise on experimental techniques* [online]. 2nd vyd. Mineola, N.Y.: Dover Publications, 1996 [vid. 2022-10-20]. ISBN 0486694445. Dostupné z: https://books.google.com/books/about/Electron_Spin_Resonance.html?hl=cs&id=P-4PIoi7Z7IC

[28] NASH, Eamon. *UNDERSTANDING, OPERATING, AND INTERFACING TO INTEGRATED DIODE-BASED RF DETECTORS* [online]. 2015 [vid. 2022-12-28]. Dostupné z: https://www.analog.com/en/technical-articles/integrated-diode-based-rf-detectors.html

[29] TSEITLIN, M. P., V. S. IYUDIN a O. A. TSEITLIN. Advantages of digital phase-sensitive detection for upgrading an obsolete CW-EPR spectrometer. *Applied Magnetic Resonance* [online]. 2009, **35**(4), 569–580 [vid. 2022-12-28]. ISSN 09379347. Dostupné z: doi:10.1007/S00723-009-0186-0/METRICS

[30] R. CAMMACK AND J.K. SHERGILL. EPR SPECTROSCOPY OF PROTEINS. In: *Proteins labfax* [online]. San Diego (CA): BIOS Scientific Publishers, 1996 [vid. 2023-12-18], s. 217–231. ISBN 9780125647106. Dostupné z: https://search.worldcat.org/title/301231066

[31] KRSTIĆ, Ivan, Burkhard ENDEWARD, Dominik MARGRAF, Andriy MARKO a Thomas F. PRISNER. Structure and dynamics of nucleic acids. In: *EPR spectroscopy - Applications in Chemistry and Biology* [online]. B.m.: Springer, Berlin, Heidelberg, 2011 [vid. 2023-12-12], s. 159–198. ISBN 9783642283468. Dostupné z: doi:10.1007/128_2011_300/COVER

[32] WEBER, Ralph T. *Pulsed EPR Primer* [online]. Billerica (MA): Bruker Instruments, 2000 [vid. 2022-12-28]. Dostupné z: http://www.sb.fsu.edu/~fajer/Fajerlab/LinkedDocuments/Primer.pdf

[33] DELIGIANNAKIS, Yiannis, Maria LOULOUDI a Nick HADJILIADIS. Electron spin echo envelope modulation (ESEEM) spectroscopy as a tool to investigate the coordination environment of metal centers. *Coordination Chemistry Reviews* [online]. 2000, **204**(1), 1–112 [vid. 2023-12-20]. ISSN 0010-8545. Dostupné z: doi:10.1016/S0010-8545(99)00218-0

[34] A. SCHWEIGER AND G. JESCHKE. *Principles of Pulse Electron Paramagnetic Resonance. Oxford University Press* [online]. Oxford: Oxford University Press, 2001 [vid. 2024-01-08]. ISBN 0198506341. Dostupné z: https://books.google.com/books/about/Principles_of_Pulse_Electron_Paramagneti.html?hl=cs&id=tkvQQElkW1wC

[35] LAGUTA, O., A. SOJKA, A. MARKO a P. NEUGEBAUER. Rapid scan ESR: A versatile tool for the spin relaxation studies at (sub)THz frequencies. *Applied Physics Letters* [online]. 2022, **120**(12), 120502 [vid. 2022-12-08]. ISSN 0003-6951. Dostupné z: doi:10.1063/5.0083010

[36] TSEYTLIN, Mark. General solution for rapid scan EPR deconvolution problem. *Journal of Magnetic Resonance* [online]. 2020, **318**, 106801 [vid. 2024-01-10]. ISSN 1090-7807. Dostupné z: doi:10.1016/J.JMR.2020.106801

[37] TSEITLIN, Mark, George A. RINARD, Richard W. QUINE, Sandra S. EATON a Gareth R. EATON. Deconvolution of sinusoidal rapid EPR scans. *Journal of*

Magnetic Resonance [online]. 2011, **208**(2), 279–283 [vid. 2023-05-11]. ISSN 1090-7807. Dostupné z: doi:10.1016/J.JMR.2010.11.015

[38] NGUYEN, Doan N., James MICHEL a Chuck H. MIELKE. Status and Development of Pulsed Magnets at the NHMFL Pulsed Field Facility. *IEEE Transactions on Applied Superconductivity* [online]. 2016, **26**(4) [vid. 2023-05-11]. ISSN 10518223. Dostupné z: doi:10.1109/TASC.2016.2515982

[39] ZHERLITSYN, S., B. WUSTMANN, T. HERRMANNSDÖRFER a J. WOSNITZA. Magnet-technology development at the dresden high magnetic field laboratory. *Journal of Low Temperature Physics* [online]. 2013, **170**(5–6), 447–451 [vid. 2023-05-11]. ISSN 00222291. Dostupné z: doi:10.1007/S10909-012-0764-7/FIGURES/2

[40] HYDE, James S., Robert A. STRANGEWAY, Theodore G. CAMENISCH, Joseph J. RATKE a Wojciech FRONCISZ. W-band frequency-swept EPR. *Journal of Magnetic Resonance* [online]. 2010, **205**(1), 93–101 [vid. 2024-01-09]. ISSN 1090-7807. Dostupné z: doi:10.1016/J.JMR.2010.04.005

[41] BORIS DZIKOVSKI. EPR Simulations with SimFonia Software | Bruker. *EPR simulations with SimFonia* [online]. 27. červenec 2022 [vid. 2024-01-11]. Dostupné z: https://www.bruker.com/en/services/training/magnetic-resonance/epr-trainings/united-states/epr-simulation-with-simfonia-software.html

[42] *EPR Software Suites: From Acquisition through Processing and Simulation* [online]. Billerica (MA): Bruker BioSpin. 2019 [vid. 2022-12-28]. Dostupné z: https://www.bruker.com/en/products-and-solutions/mr/epr-instruments/epr-software.html

[43] WEBER, Ralph. *Xenon Data Processing Reference* [online]. Billerica (MA USA): Bruker BioSpin, 2012. Dostupné z: http://www.nmrcenter.buffalo.edu/EPR_Processing.pdf

[44] JINJIE JIANG, Ralph Weber. *EPR Spectrometer User's Manual - ELEXSYS E500* [online]. Billerica (MA USA): Bruker BioSpin Corporation, 2001. Dostupné z: http://www.sb.fsu.edu/~fajer/Fajerlab/LinkedDocuments/E500 Basic.pdf

[45] BORIS EPEL. *SpecMan4EPR* [online]. Chicago (IL): FeMi Instruments. 2017 [vid. 2022-12-28]. Dostupné z: www.specman4epr.com

[46] EPEL, Boris, Igor GROMOV, Stefan STOLL, Arthur SCHWEIGER a Daniella GOLDFARB. Spectrometer manager: A versatile control software for pulse EPR spectrometers. *Concepts in Magnetic Resonance Part B: Magnetic Resonance Engineering* [online]. 2005, **26B**(1), 36–45 [vid. 2023-01-12]. ISSN 1552-504X. Dostupné z: doi:10.1002/CMR.B.20037

[47] STOLL, Stefan a Arthur SCHWEIGER. EasySpin, a comprehensive software package for spectral simulation and analysis in EPR. *Journal of Magnetic*

Resonance [online]. 2006, **178**(1), 42–55. ISSN 10907807. Dostupné z: doi:10.1016/j.jmr.2005.08.013

[48] TAIT, Claudia E., Matthew D. KRZYANIAK a Stefan STOLL. Computational tools for the simulation and analysis of spin-polarized EPR spectra. *Journal of Magnetic Resonance* [online]. 2023, **349**, 107410 [vid. 2024-01-11]. ISSN 1090-7807. Dostupné z: doi:10.1016/J.JMR.2023.107410

[49] REIJERSE, Edward J. High-frequency EPR instrumentation. *Applied Magnetic Resonance* [online]. 2010, **37**(1), 795–818 [vid. 2022-10-20]. ISSN 09379347. Dostupné z: doi:10.1007/S00723-009-0070-Y

[50] WANG, Qiuliang, Zhipeng NI, Chunyan CUI, Qiuliang WANG, Zhipeng NI a Chunyan CUI. Superconducting Magnet Technology and Applications. In: *Superconductors - Materials, Properties and Applications* [online]. B.m.: IntechOpen, 2012 [vid. 2023-01-02]. ISBN 978-953-51-0794-1. Dostupné z: doi:10.5772/48465

[51] HAHN, Seungyong, Kwanglok KIM, Kwangmin KIM, Xinbo HU, Thomas PAINTER, Iain DIXON, Seokho KIM, Kabindra R. BHATTARAI, So NOGUCHI, Jan JAROSZYNSKI a David C. LARBALESTIER. 45.5-tesla direct-current magnetic field generated with a high-temperature superconducting magnet. *Nature 2019 570:7762* [online]. 2019, **570**(7762), 496–499 [vid. 2024-01-12]. ISSN 1476-4687. Dostupné z: doi:10.1038/s41586-019-1293-1

[52] CHEN, Pin Hui, Chukun GAO, Nicholas ALANIVA, Snædís BJÖRGVINSDÓTTIR, Ioannis Gr PAGONAKIS, Michael A. URBAN, Alexander DÄPP, Ronny GUNZENHAUSER a Alexander B. BARNES. Watch-sized 12 Tesla all-high-temperature-superconducting magnet. *Journal of Magnetic Resonance* [online]. 2023, **357**, 107588 [vid. 2024-01-17]. ISSN 1090-7807. Dostupné z: doi:10.1016/J.JMR.2023.107588

[53] ALEXANDER BARNES. MOTES Group seminar: Instrumentation for high-field magnetic resonance. In: . Zurich. 2024.

[54] KRAMER DAVID. Helium shortage has ended, at least for now. *Physics Today* [online]. 2020, **2020**(2) [vid. 2023-01-02]. ISSN 0031-9228. Dostupné z: doi:10.1063/PT.6.2.20200605A

[55] SMIRNOV, Alex I., Tatyana I. SMIRNOVA, Ryan L. MACARTHUR, Jeremy A. GOOD a Renny HALL. Cryogen-free superconducting magnet system for multifrequency electron paramagnetic resonance up to 12.1 T. *Review of Scientific Instruments* [online]. 2006, **77**(3). ISSN 00346748. Dostupné z: doi:10.1063/1.2182571

[56] REIJERSE, E., P. P. SCHMIDT, G. KLIHM a W. LUBITZ. A CW and pulse EPR spectrometer operating at 122 and 244 GHz using a quasi-optical bridge and a cryogen-free 12 T superconducting magnet. *Applied Magnetic Resonance 2007*

31:3 [online]. 2007, **31**(3), 611–626 [vid. 2022-12-12]. ISSN 1613-7507. Dostupné z: doi:10.1007/BF03166606

[57] UDAL, Andres, Martin JAANUS, Gintaras VALUŠIS, Irmantas KAŠALYNAS, Zoran IKONIC a Dragan INDJIN. Progress in development of the resonant tunneling diodes as promising compact sources at the THz gap bottom. *NATO Science for Peace and Security Series B: Physics and Biophysics* [online]. 2017, **PartF1**, 169–178 [vid. 2023-01-02]. ISSN 18746500. Dostupné z: doi:10.1007/978-94-024-1093-8_20

[58] FEDOTOV, A. E., V. L. BRATMAN, B. S. DUMESH, P. B. MAKHALOV a F. S. RUSIN. Orotron oscillators and frequency multipliers as sources of coherent terahertz radiation. *Proceedings - TERA-MIR 2009, NATO Advanced Research Workshop Terahertz and Mid Infrared Radiation: Basic Research and Practical Applications* [online]. 2009, 19–20 [vid. 2023-01-02]. Dostupné z: doi:10.1109/TERAMIR.2009.5379648

[59] HORNSTEIN, M. K., R. G. GRIFFIN, J. MACHUZAK, M. A. SHAPIRO, R. J. TEMKIN a K. E. KREISCHER. A 460 GHz gyrotron oscillator for use in DNP / NMR spectroscopy. *IEEE International Conference on Plasma Science* [online]. 2001 [vid. 2023-01-02]. ISSN 07309244. Dostupné z: doi:10.1109/PPPS.2001.961319

[60] KAINZ, Martin Alexander, Sebastian SCHÖNHUBER, Aaron Maxwell ANDREWS, Hermann DETZ, Benedikt LIMBACHER, Gottfried STRASSER a Karl UNTERRAINER. Barrier Height Tuning of Terahertz Quantum Cascade Lasers for High-Temperature Operation. *ACS Photonics* [online]. 2018, **5**(11), 4687–4693 [vid. 2023-01-02]. ISSN 23304022. Dostupné z: doi:10.1021/ACSPHOTONICS.8B01280/ASSET/IMAGES/LARGE/PH-2018-012802_0007.JPEG

[61] BLAKE WILSON, C., Samuel ARONSON, Jessica A. CLAYTON, Steffen J. GLASER, Songi HAN a Mark S. SHERWIN. Multi-step phase-cycling in a free-electron laser-powered pulsed electron paramagnetic resonance spectrometer. *Physical Chemistry Chemical Physics* [online]. 2018, **20**(26), 18097–18109 [vid. 2024-01-18]. ISSN 1463-9084. Dostupné z: doi:10.1039/C8CP01876F

[62] MEHDI, I., G. CHATTOPADHYAY, E. SCHLECHT, J. WARD, J. GILL, F. MAIWALD a A. MAESTRINI. Terahertz multiplier circuits. *IEEE MTT-S International Microwave Symposium Digest* [online]. 2006, 341–344 [vid. 2023-01-02]. ISSN 0149645X. Dostupné z: doi:10.1109/MWSYM.2006.249521

[63] PRAJAPATI, Dhruvi D a Neelkanthan USHA. Review Paper on Frequency Multiplier at Terahertz Range. *International Journal on Recent and Innovation Trends in Computing and Communication* [online]. 2017, **5**(2), 228–232 [vid. 2023-01-02]. ISSN 2321-8169. Dostupné z: doi:10.17762/IJRITCC.V5I2.204

[64] LIU, Xiao-Yu, 刘晓宇, Yong ZHANG, 张勇, De-Jiao XIA, 夏德娇, Tian-Hao REN, 任田昊, Jing-Tao ZHOU, 周静涛, Dong GUO, 郭栋, Zhi JIN a 金智. A High-Sensitivity Terahertz Detector Based on a Low-Barrier Schottky Diode*. *Chinese Physics Letters* [online]. 2017, **34**(7), 070701 [vid. 2023-01-02]. ISSN 0256-307X. Dostupné z: doi:10.1088/0256-307X/34/7/070701

[65] *Bolometers and IR Detectors - IRLabs* [online]. [vid. 2024-01-12]. Dostupné z: https://www.irlabs.com/products/bolometers/

[66] EFETOV, Dmitri K., Ren Jye SHIUE, Yuanda GAO, Brian SKINNER, Evan D. WALSH, Hyeongrak CHOI, Jiabao ZHENG, Cheng TAN, Gabriele GROSSO, Cheng PENG, James HONE, Kin Chung FONG a Dirk ENGLUND. Fast thermal relaxation in cavity-coupled graphene bolometers with a Johnson noise read-out. *Nature Nanotechnology 2018 13:9* [online]. 2018, **13**(9), 797–801 [vid. 2023-01-02]. ISSN 1748-3395. Dostupné z: doi:10.1038/s41565-018-0169-0

[67] GOLDSMITH, Paul F. Quasi-Optical Techniques. *Proceedings of the IEEE* [online]. 1992, **80**(11), 1729–1747 [vid. 2023-01-02]. ISSN 15582256. Dostupné z: doi:10.1109/5.175252

[68] SMITH, G. M., J. C.G. LESURF, R. H. MITCHELL a P. C. RIEDI. Quasi-optical cw mm-wave electron spin resonance spectrometer. *Review of Scientific Instruments* [online]. 1998, **69**(11), 3924 [vid. 2022-11-10]. ISSN 0034-6748. Dostupné z: doi:10.1063/1.1149200

[69] NEUGEBAUER, Petr a Anne Laure BARRA. New cavity design for broad-band quasi-optical hf-epr spectroscopy. *Applied Magnetic Resonance* [online]. 2010, **37**(1), 833–843 [vid. 2021-03-22]. ISSN 09379347. Dostupné z: doi:10.1007/s00723-009-0092-5

[70] NAFTALY, M., R.E. MILES a P.J. GREENSLADE. THz transmission in polymer materials &#x2014; a data library. *2007 Joint 32nd International Conference on Infrared and Millimeter Waves and the 15th International Conference on Terahertz Electronics* [online]. 2007, 819–820 [vid. 2024-01-18]. Dostupné z: doi:10.1109/ICIMW.2007.4516747

[71] SOJKA, Antonín, Matúš ŠEDIVÝ, Adam LAGIN, Andrej GABRIS, Tomáš LÁZNIČKA, Vinicius Tadeu SANTANA, Oleksii LAGUTA a Petr NEUGEBAUER. Sample Holders for Sub-THz Electron Spin Resonance Spectroscopy. *IEEE Transactions on Instrumentation and Measurement* [online]. 2022, **71** [vid. 2022-10-13]. ISSN 15579662. Dostupné z: doi:10.1109/TIM.2022.3164135

[72] SOLODOVNYK, Artur, Dariya SAVCHENKO, Oleksii LAGUTA a Petr NEUGEBAUER. Implementation of Broadband Electrically Detected Magnetic Resonance in a sub-THz FraScan Spectrometer. *IEEE Transactions on Instrumentation and Measurement* [online]. 2023 [vid. 2023-08-02]. ISSN 15579662. Dostupné z: doi:10.1109/TIM.2023.3284951

[73] KALKMAN, Cor J. LabVIEW: A software system for data acquisition, data analysis, and instrument control. *Journal of Clinical Monitoring* [online]. 1995, **11**(1), 51–58 [vid. 2021-05-17]. ISSN 07481977. Dostupné z: doi:10.1007/BF01627421

[74] ELLIOTT, Chance, Vipin VIJAYAKUMAR, Wesley ZINK a Richard HANSEN. National Instruments LabVIEW: A Programming Environment for Laboratory Automation and Measurement. *Journal of Laboratory Automation* [online]. 2007, **12**(1), 17–24 [vid. 2021-05-17]. ISSN 15402452. Dostupné z: doi:10.1016/j.jala.2006.07.012

[75] SOJKA, Antonín. *Development of a Novel Terahertz Magnetic Resonance Spectrometer for Spin Dynamics Investigations* [online]. B.m., 2022. Brno University of Technology. Dostupné z: https://dspace.vutbr.cz/handle/11012/204114

[76] MIDLÍKOVÁ, Jana Dubnická, Matúš ŠEDIVÝ, Antonín SOJKA, Vinicius Tadeu SANTANA, Adam DUBROKA a Petr NEUGEBAUER. A Versatile Setup for Fourier-Transform Infrared Magneto-Spectroscopy. *IEEE Transactions on Instrumentation and Measurement* [online]. 2023, **72**, 1–11 [vid. 2023-07-26]. ISSN 0018-9456. Dostupné z: doi:10.1109/TIM.2023.3284943

[77] ST MARIE, Luke, Abdel EL FATIMY, Jakub HRUBÝ, Ivan NEMEC, James HUNT, Rachael MYERS-WARD, D. KURT GASKILL, Mattias KRUSKOPF, Yanfei YANG, Randolph ELMQUIST, Raphael MARX, Joris VAN SLAGEREN, Petr NEUGEBAUER a Paola BARBARA. Nanostructured graphene for nanoscale electron paramagnetic resonance spectroscopy. *Journal of Physics: Materials* [online]. 2020, **3**(1), 014013 [vid. 2023-11-09]. ISSN 2515-7639. Dostupné z: doi:10.1088/2515-7639/AB6AF8

[78] MARTYNIUK, Oleh, Vivek CHAUDHARY, M. BARTOŠ, O. LAGUTA, Rachael MYERS-WARD, D Kurt GASKILL, P. BARBARA, A. EL FATIMY a Petr NEUGEBAUER. Graphene Quantum Dot Bolometer Camera: Practical Approaches and Preliminary Results. *2023 48th International Conference on Infrared, Millimeter, and Terahertz Waves (IRMMW-THz)* [online]. 2023, 1–2 [vid. 2023-11-09]. Dostupné z: doi:10.1109/IRMMW-THZ57677.2023.10298959

[79] COLLE, Jean Yves, Jouni RAUTIO a Daniel FREIS. A modular LabVIEW application frame for Knudsen Effusion Mass Spectrometry instrument control. *SoftwareX* [online]. 2021, **16**, 100875 [vid. 2022-02-24]. ISSN 23527110. Dostupné z: doi:10.1016/j.softx.2021.100875

[80] TITOV, Igor. Using LabVIEW for building laboratory server: Pros and cons, design patterns, software architecturing and common pitfalls. *IEEE Global Engineering Education Conference, EDUCON* [online]. 2014, (April), 1101–1107. ISSN 21659567. Dostupné z: doi:10.1109/EDUCON.2014.6826247

[81] FABIOLA DE LA CUEVA. *Delacor Queued Message Handler* [online]. 2022 [vid. 2023-08-31]. Dostupné z: https://dqmh.org/

[82] CZERWINSKI, Fabian a Lene B. ODDERSHEDE. TimeSeriesStreaming.vi: LabVIEW program for reliable data streaming of large analog time series. *Computer Physics Communications* [online]. 2011, **182**(2), 485–489 [vid. 2022-10-18]. ISSN 0010-4655. Dostupné z: doi:10.1016/J.CPC.2010.10.019

[83] SOLODOVNYK, Artur, Oleksii LAGUTA, Andrey PROKHOROV, Michele SEGANTINI, Boris NAYDENOV, Petr NEUGEBAUER, Siegmund GREULICH-WEBER, Ekaterina KALABUKHOVA a Dariia SAVCHENKO. Spin dynamics of exchange-coupled nitrogen donors in heavily doped n -type 15R SiC monocrystals: Multifrequency EPR and EDMR study. *Physical Review B* [online]. 2023, **107**(15), 155202 [vid. 2023-08-02]. ISSN 24699969. Dostupné z: doi:10.1103/PHYSREVB.107.155202

[84] GIRALDO, Jorge Navarro, Jakub HRUBÝ, Šárka VAVREČKOVÁ, Ondřej F. FELLNER, Lubomír HAVLÍČEK, Da Vonne HENRY, Shehan DE SILVA, Radovan HERCHEL, Miroslav BARTOŠ, Ivan ŠALITROŠ, Vinicius T. SANTANA, Paola BARBARA, Ivan NEMEC a Petr NEUGEBAUER. Tetracoordinate Co(II) complexes with semi-coordination as stable single-ion magnets for deposition on graphene. *Physical Chemistry Chemical Physics* [online]. 2023, **25**(43), 29516–29530 [vid. 2024-01-15]. ISSN 1463-9084. Dostupné z: doi:10.1039/D3CP01426F

[85] JURÁKOVÁ, Jana, Ondřej F. FELLNER, Sören SCHLITTENHARDT, Šárka VAVREČKOVÁ, Ivan NEMEC, Radovan HERCHEL, Erik ČIŽMÁR, Vinicius Tadeu SANTANA, Milan ORLITA, Denis GENTILI, Giampiero RUANI, Massimiliano CAVALLINI, Petr NEUGEBAUER, Mario RUBEN a Ivan ŠALITROŠ. Neutral cobalt(II)-bis(benzimidazole)pyridine field-induced single-ion magnets for surface deposition. *Inorganic Chemistry Frontiers* [online]. 2023, **10**(18), 5406–5419 [vid. 2024-01-15]. ISSN 2052-1553. Dostupné z: doi:10.1039/D3QI00931A

[86] CALVO, Rafael, Rosana P. SARTORIS, Otaciro R. NASCIMENTO, Matúš ŠEDIVÝ, Antonin SOJKA, Petr NEUGEBAUER a Vinicius T. SANTANA. Quantum phase transitions probed by EPR spectra in dimeric spin arrays with supramolecular couplings. *Coordination Chemistry Reviews* [online]. 2023, **480**, 215007 [vid. 2023-02-14]. ISSN 0010-8545. Dostupné z: doi:10.1016/J.CCR.2022.215007

[87] SOJKA, Antonín, Matúš ŠEDIVÝ, Oleksii LAGUTA, Andriy MARKO, Vinicius T. SANTANA a Petr NEUGEBAUER. High-frequency EPR: Current state and perspectives. *Electron Paramagnetic Resonance* [online]. 2021, **27**, 214–252 [vid. 2022-10-12]. ISSN 14651955. Dostupné z: doi:10.1039/9781839162534-00214

[88] ZOLNAI, Zsolt. *Irradiation-induced crystal defects in silicon carbide* [online]. B.m., 2005. Ph . D . Thesis. Budapest University of Technology and Economics. Dostupné z: https://repozitorium.omikk.bme.hu/handle/10890/418

[89] GRUBER, Gernot. *Performance and Reliability Limiting Point Defects in SiC Power Devices* [online]. B.m., 2016. Technischen Universität Graz. Dostupné z: https://diglib.tugraz.at/download.php?id=5988e7b30147b&location=browse

[90] CASTELLETTO, S., C. T.K. LEW, Wu Xi LIN a Jin Shi XU. Quantum systems in silicon carbide for sensing applications. *Reports on Progress in Physics* [online]. 2023, **87**(1), 014501 [vid. 2024-01-16]. ISSN 0034-4885. Dostupné z: doi:10.1088/1361-6633/AD10B3

[91] REJHON, Martin, Mykola BRYNZA, Roman GRILL, Eduard BELAS a Jan KUNC. Investigation of deep levels in semi-insulating vanadium-doped 4H-SiC by photocurrent spectroscopy. *Physics Letters, Section A: General, Atomic and Solid State Physics* [online]. 2021, **405**, 127433 [vid. 2022-05-26]. ISSN 03759601. Dostupné z: doi:10.1016/j.physleta.2021.127433

[92] MITCHEL, W. C., W. D. MITCHELL, G. LANDIS, H. E. SMITH, Wonwoo LEE a M. E. ZVANUT. Vanadium donor and acceptor levels in semi-insulating 4H - And 6H-SiC. *Journal of Applied Physics* [online]. 2007, **101**(1). ISSN 00218979. Dostupné z: doi:10.1063/1.2407263

[93] VON BARDELEBEN, Hans Jürgen, S. A. ZARGALEH, J. L. CANTIN, Weibo. B. GAO, Timur BIKTAGIROV a Uwe GERSTMANN. Transition metal qubits in 4H -silicon carbide: A correlated EPR and DFT study of the spin S=1 vanadium V3+ center. *Physical Review Materials* [online]. 2019, **3**(12), 124605 [vid. 2022-10-20]. ISSN 24759953. Dostupné z: doi:10.1103/PHYSREVMATERIALS.3.124605/

[94] SATO, Hideo, Lauraine A. DALTON, Duc HA, Richard W. QUINE, Sandra S. EATON a Gareth R. EATON. Electron Spin Relaxation in x-Lithium Phthalocyanine. *Journal of Physical Chemistry B* [online]. 2007, **111**(28), 7972–7977 [vid. 2022-12-21]. ISSN 15206106. Dostupné z: doi:10.1021/JP070810Y

[95] WACHTEL, H., J. C. WITTMANN, B. LOTZ, M. A. PETIT a J. J. ANDRÉ. Anisotropic spin transport in oriented lithium phthalocyanine thin films. *Thin Solid Films* [online]. 1994, **250**(1–2), 219–231 [vid. 2022-12-20]. ISSN 0040-6090. Dostupné z: doi:10.1016/0040-6090(94)90189-9

[96] AFEWORKI, Mobae, Nathan R. MILLER, Nallathamby DEVASAHAYAM, John COOK, James B. MITCHELL, S. SUBRAMANIAN a Murali C. KRISHNA. Preparation and EPR Studies of Lithium Phthalocyanine Radical as an Oxymetric Probe. *Free Radical Biology and Medicine* [online]. 1998, **25**(1), 72–78 [vid. 2022-12-20]. ISSN 0891-5849. Dostupné z: doi:10.1016/S0891-5849(98)00039-2

[97] *OriginPro*. Northampton, MA, USA: OriginLab Corp. 2022

[98] BRINKMANN, M. a J. J. ANDRÉ. Electrodeposited lithium phthalocyanine thin films. Part II:† magnetic properties and mesoscopic effects. *Journal of Materials Chemistry* [online]. 1999, **9**(7), 1511–1520 [vid. 2022-12-21]. ISSN 1364-5501. Dostupné z: doi:10.1039/A809778J

[99] ŠEDIVÝ, Matúš, Vinicius SANTANA, Antonín SOJKA, Oleksii LAGUTA a Petr NEUGEBAUER. MEPROS – Modular electron paramagnetic resonance operating software for multifunctional high-frequency EPR spectrometer. *Journal of Magnetic Resonance* [online]. 2023, **355**, 107556 [vid. 2024-01-16]. ISSN 1090-7807. Dostupné z: doi:10.1016/J.JMR.2023.107556

[100] KÜNSTNER, Silvio, Anh CHU, Klaus Peter DINSE, Alexander SCHNEGG, Joseph E. MCPEAK, Boris NAYDENOV, Jens ANDERS a Klaus LIPS. Rapid-scan electron paramagnetic resonance using an EPR-on-a-Chip sensor. *Magnetic Resonance* [online]. 2021, **2**(2), 673–687 [vid. 2024-01-17]. ISSN 26990016. Dostupné z: doi:10.5194/MR-2-673-2021

List of symbols and abbreviations

Abbreviations

EPR – electron paramagnetic resonance

ESR – electron spin resonance

DNP – dynamic nuclear polarization

FRaScan – frequency rapid scan

CW – continuous wave

PLL – phase locked loop

IMPATT - ionization avalanche transition time

YIG – Yttrium Iron grenade

BWO – backward wave oscillator

RTD – resonant tunneling diode

TWT – traveling wave tube

QCL – quantum cascade laser

HBV – heterostructure barrier varactor

HEMT – high electron mobility transistor

VCO – voltage controlled oscillator

AWG – arbitrary waveform generator

SNR – signal-to-noise

PSD – phase sensitive detection

NEP – noise equivalent power

DC – direct current

FID – free induction decay

FWHM – full width at half maximum

LabVIEW – laboratory virtual instrument engineering workbench

EPRoC – EPR on chip

HFEPR – high field/ high frequency EPR

NMR – nuclear magnetic resonance

MRI – nuclear magnetic resonance imaging

ESEEM – electron spin echo envelope modulation

HYSCORE – hyperfine sublevel correlation

ENDOR – electron-nuclear double resonance
PELDOR – pulse electron double resonance
DEER – double electron-electron resonance
PTFE – polytetrafluoroethylene, Teflon
PET – polyethylene terephthalate
PEEK – polyether ether ketone
CFM – cryogen free magnet
VTI – variable temperature insert
FS-EPR – frequency swept EPR
QO – quasi-optics
MFLI – medium frequency lock-in amplifier
SMS – superconducting magnet supply
SMU – source meter unit
PSU – power supply unit
DMM – digital multimeter
AMC – amplification multiplication chain
UPS – uninterruptible power supply
FTIR – Fourier-transform infrared
SSH – simple sample holder
LSH – liquid sample holder
RSH – rotator sample holder
CSH – carousel sample holder
ChSH – chip sample holder
DQMH – Delacor Queued Message Handler
FIFO – first in first out buffer
TDMS – technical data management streaming
GUI – graphical user interface
SiC – silicon carbide
MOSFET – metal-oxide-semiconductor field-effect transistor
LiPc – phthalocyanine
BDPA – Koelsch's radical or 1,3(α,γ)-bisdiphenylene-2(β)-phenylallyl

Symbols

β_e – Bohr magneton of electron
f,ν – frequency
q – elementary charge
g – g-factor
m_e – mass of electron
$\hbar$ – reduced Planck constant
S – spin momentum
μ – magnetic dipolar momentum
φ – phase shift
Ω, ω – angular frequency
k_b – Boltzmann constant
T – absolute temperature, relaxation time, time period
B_0 – external (static) magnetic field
ΔE – difference in energy levels
m_s – electron quantum spin number
m_I – nuclear quantum spin number
I – nuclear spin momentum, current
A – hyperfine coupling constant
D – Zero-field splitting constant
$\hat{H}$ – spin Hamiltonian
N_u, N_l – density of states at upper and lower level
$\boldsymbol{M}$ – magnetization vector
δE – excess energy
τ – relaxation time
B_1 – oscillating magnetic field
V - voltage
Q – quadrupole interaction constant, quality factor
γ – gyromagnetic ration

List of figures

List of tables

List of author’s most significant publications

MEPROS – Modular electron paramagnetic resonance operating software for multifunctional high-frequency EPR spectrometer
Journal of Magnetic Resonance
2023-10 | journal-article, DOI: 10.1016/j.jmr.2023.107556, Part of ISSN: 1090-7807

Quantum phase transitions probed by EPR spectra in dimeric spin arrays with supramolecular couplings
Coordination Chemistry Reviews
2023-04 | journal-article, DOI: 10.1016/j.ccr.2022.215007

A Versatile Setup for Fourier-Transform Infrared Magneto-Spectroscopy
IEEE Transactions on Instrumentation and Measurement
2023 | journal-article, DOI: 10.1109/TIM.2023.3284943

Sample Holders for Sub-THz Electron Spin Resonance Spectroscopy
IEEE Transactions on Instrumentation and Measurement
2022 | journal-article, DOI: 10.1109/tim.2022.3164135, Part of ISSN: 0018-9456

High-frequency EPR: current state and perspectives
Electron Paramagnetic Resonance
2020 | book-chapter, DOI: 10.1039/9781839162534-00214, Part of ISSN: 1465-1955

Appendix A – Construction of HFEPR spectrometer

Construction of HF-EPR FRaScan spectrometer in EPR laboratory of CEITEC BUT has started in 2018. Here is a brief overview history of the construction:

- 1st Q 2018: Learning of LabVIEW as preparation for later software development while Antonin Sojka designed main *base support frame*, *table frame*, and *positioning system* for the FRaScan HF-EPR spectrometer.
- 2nd Q 2018: Building of the base frame.
- 3rd Q 2018: Installation of the cryogen free magnet system. Installation of energetic belt into supporting frame. Prototype of a software module for the magnet remote control. Antonin Sojka finalized an air lock design and positioning system. Construction of the table frame. Installation of linear movement mechanism into the base frame.
- 4th Q 2018: Additional adjustments of the base frame and magnet installation. Preliminary test of servo drives. Prototyping of software module for control of servo drives. Installation of Servo drive for X-axis positioning. Design connection plate for easy connection of the spectrometer's table to the rest of the system. Installation of Quasi-optical table. Antonin Sojka troubleshoot air lock system and designed a rack-mounting system for instruments inside the table frame.
- 1st Q 2019: Troubleshooting and additional wiring for all five axes of the positioning system. Antonin Sojka installed air lock and made a simple sample holder.
- 2nd Q 2019: EPR probe wiring. VTI and THz system control module.
- 3rd Q 2019: Tests of quasi optical and terahertz systems. Software module for lock-in amplifier.
- 4th Q 2019: Test run of the spectrometer (homodyne detection). Testing and debugging of the control software.
- Since 2020: Initial run of the spectrometer - first results. Further enhancements of the spectrometer. Additional software modules (rotator, source meter). Heterodyne detection. Frequency swept measurements. Calibration of temperature sensors. Magnetic field meter. Replacement of hermetic connectors on probe head and rewiring of probe. Antonin Sojka made new sample holders.

A particular information on the HFEPR FRaScan spectrometer is in the following subsections.

Base frame and table frame

Main function of the base frame is a mechanical support of cryostat, CFM, VTI and enable linear positioning of the table frame. It is made of aluminum strut profiles and brackets and mounted by stainless steel screws and T nuts (M6 and M8). Materials were chosen to be nonmagnetic and withstand a heavy load. The base frame has a rectangular shape and part of it is placed over a pit in the laboratory floor, that was made for placing of CFM. The base frame also contains rails on top of which is a movable platform with aligning grooves. Inside the platform is a plate with electric sockets and connectors (3x IEC C19 for ~230V electric power, USB3.0 connected to USB hub, RJ45 connected to ethernet switch, 24VDC a pneumatic push-in fitting for nitrogen, XT90E-M and NAC3MPA1 to power the servo drivers). An energetic belt, fastened to the base frame on one side and to the platform on the other side, protects cables which leads to sockets and connectors. A powerful servomotor with precise encoder and threated rod provides control over positioning of the movable platform towards the CFM (X-axis).

The table frame is a cage made of the same building components as a base frame. Its function is to carry the QO table and necessary instruments for spectrometer. At the bottom of the table frame are aligning pins that fits into grooves on the movable platform. Therefore, the frame moves together with the platform. Optionally, it can be easily taken away and later put back to the very same place. Upper part of the table frame contains one servomotor for positioning of QO table in Y-axis and three servomotors for vertical (Z-axis) positioning and inclination. Control units for servomotors are also mounted in the table frame. The frame was additionally equipped with rack system that carry a power socket (C13) extender, a power supply for THz sources and mixers, a lock-in amplifier, a multimeter, PXI chassis, USB 3.0 hub and ethernet switch. By sides of the frame are installed drawers, in which exchangeable QO components as faraday rotators and horns are always at hand.

Both frames were designed by Antonin Sojka. Most of construction parts and many consultations were provided by PK SERVIS.

Installation of cryogenic system

A cryogen-free magnet system (CFM) was bought from a company Cryogenic Limited and delivered in summer 2018. The system uses two-stage pulse cryocoolers to liquify helium pumped by a pair of compressors. System can be cooled down from room temperature to a base temperature in 2 days. A magnet is attached to second stage of the cryocoolers and is composed from outer and inner superconducting coils. Both coils have a common central axis and are connected parallelly. Coils are placed vertically in a cryostat with a variable temperature insertion (VTI) feature that allows to control temperature inside of a sample space. The VTI has a 50 mm vertical sample access bore. Outer vessel of the cryostat is manufactured from aluminum alloy; the VTI is manufactured from stainless steel. On top of the cryostat are ports for: a cryocooler, evacuation, gas return port for the VTI flow circuit, magnet current leads and instrumentation (superconducting switch heater, several temperature sensors, VTI heater and electronic control of needle valve). A high temperature superconductor is used for a current lead between first and second stage. The cryostat further contains a radiation shield attached to the first stage of the cryocoolers.

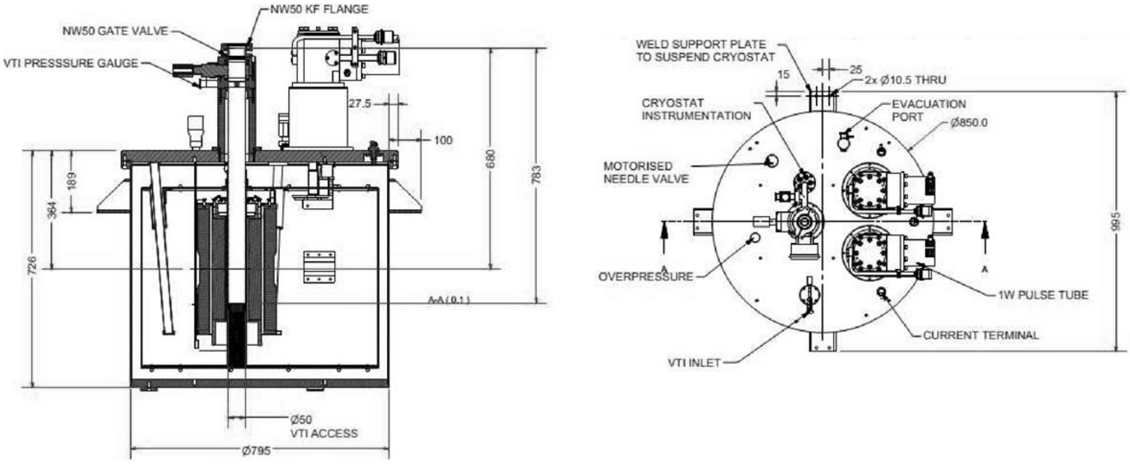

Figure S-1: Drawings of cryostat taken from a documentation to 16T superconducting magnet system made by the Cryogenics Ltd.

Compressors which provide circulation of helium in the cryogen-free system were placed in a separate room one floor below the lab to reduce noise and vibrations. The cryostat containing SCM was placed into the pit and mounted to the base frame. After installation of cryostat its temperature isolation space was evacuated over night with a turbomolecular pump. After that, cryocooler heads were connected to compressors and SCM was cooled down. Then magnet current terminals were connected to a power supply unit (PSU) and magnet was tested. During the energizing test magnet experienced so-called training quench at about 11 T. This training quench sometimes occurs when a new superconducting magnet is energized for the first time. The PSU contains safety circuits for discharging of the magnet in case of quench. Additionally, there is a passive protection in cryostat (resistor and thyristor connected in parallel to magnet coils) for case that quench will occur during a power outage. After magnet recovered from a quench, it was energized again to the maximum field 16 T and discharged.

Later, during the maintenance the position of cryostat was changed deeper into the pit to reduce effects of magnetic field to a nearby objects. It also helped to achieve better match of distance between QO table and center of magnetic field according to length of a EPR probe with sample holders. Before that, compressors were turned off and magnet was left freely to heat up to a room temperature for about three days. After maintenance was done, magnet was cooled down again.

Table S-1: CFM system specifications (according to 16T Cryogen free Magnet 4382 manual)

VTI access bore diameter	50 mm
Cryostat diameter	850 mm
Cryostat height (to top of gate valve)	1051 mm
Cold head	Sumitomo RP 082
Cooldown time	42 hours
Magnetic field constant	149.11 mT/A
Electric current at 16 T	107.3 A
Maximum magnetic field (tested)	16.18 T
Magnet inductance	102 H
Switch temperature in persistence mode	≤ 4.0 K
Switch temperature in ramping mode	≥ 5.0 K
Recommended switch temperature	2.5 V
Recommended ramp rates for magnetic field ranges	
Range 0–3 T	7.544966 mT/s
Range 3–9.6 T	5.66618 mT/s
Range 9.6–13.3 T	4.249635mT/s
Range 13.3–15.5 T	3.176043 mT/s
Range 15.5–16 T	1.550774 mT/s
Base temperatures:	
Cryocooler A first stage	36.7 K
Cryocooler A second stage	3.5 K
Cryocooler B first stage	38.1 K
Cryocooler B second stage	3.8 K
Inner magnet coil	5.07 K
Outer magnet coil	3.91 K
Persistence mode switch	3.7 K
Supporting plate	9.83 K

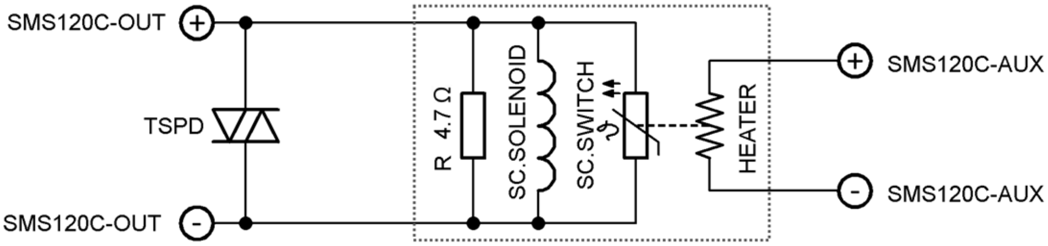

Figure S-2: A simplified functional scheme of the 16T superconducting magnet connection to its power supply SMS120C. Green dotted line denotes components inside of the cryostat.

A variable temperature insertion (VTI) system allows to control a temperature of a sample placed inside the magnet in a range of approximately from 2 K to 325 K. The VTI is a built-in part of cryostat. In principle, it creates a secondary helium circuit, which takes a cooling power from the primary helium circuit and delivers liquefied helium into the sample space, where it evaporates and cools down a sample.

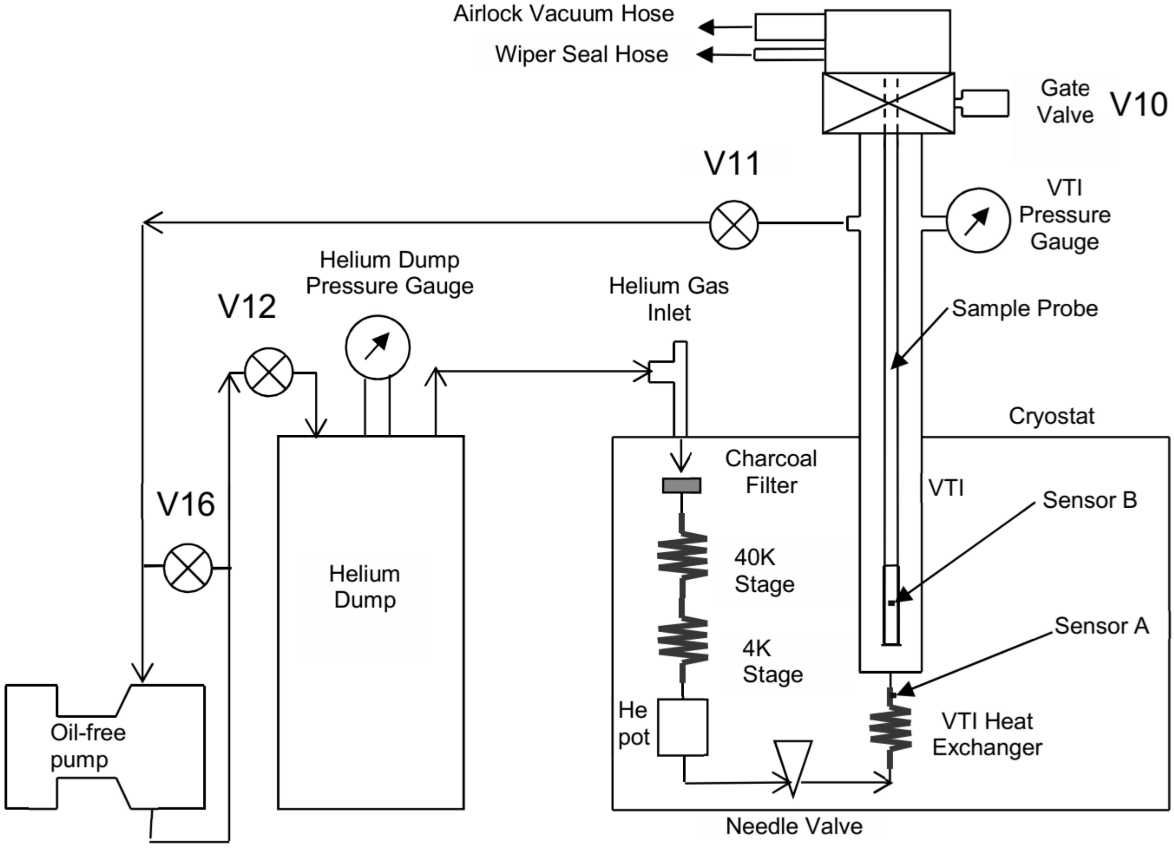

Figure S-3: Schematic diagram of the VTI system provided by Cryogenics Ltd.

The system is controlled by three elements. First is a pump, which causes that helium flows in the circuit. To suppress effect of mechanical noise, pump is placed outside of the cryostat and connected by a pair of flexible and properly thermally isolated hoses. Pump can operate in normal mode for maximum flow, standby mode when motor speed is decreased, or be turned off to stop helium flow completely. A part of pump station is small helium tank, that serves as a supply of helium. Second control element is needle valve for a very fine regulation of the helium flow, because even a relatively small change of the flow can cause either overload of primary cooling circuit, or insufficient cooling of sample. After the needle valve, there is a pressure gauge for indicative measurement of flow, which is proportional to the pressure. A third control element is a heater which can heat the incoming helium and prevent its liquefaction before it enters the sample space.

Servo drive system for the quasi-optical table

Aluminum profiles were used to build a frame of the spectrometer. The frame consists of a stationary base frame with rails on which a movable table frame is placed. One servomotor and its gear is placed in the base frame to move the table frame along X-axis. Another servomotor is placed in table frame to move a quasi-optical (QO) table along Y-axis. Three more servomotors control a position and inclination of QO table in Z-axis. This positioning system was designed by Antonin Sojka. Role of positioning system is important because even small misalignment can cause significant loss of an EPR signal. Servomotors and controllers were supplied by a Bosch Rexroth company.

Each axis was tested separately at first. However, when all servo controllers were turned on at once, it triggered 30 mA residual-current device (RCD). Therefore a few modifications in a power supply line to servo drive system was done. A schematic of power distribution is shown in Figure S-4. Whole system is protected by 16 A circuit breaker of type C and RCD that has 100 mA sensitivity. A filter prevents voltage distortions produced by servo controllers to return into the power line. Controllers require DC supply at 24 V that is provided by EDR-150-24 power source. A timing relay is used to delay a power distribution for other controllers in order to shrink a peak current. Each controller is connected with computer by SFTP cable via Ethernet interface. Optical sensors are planned to be used as end switches.

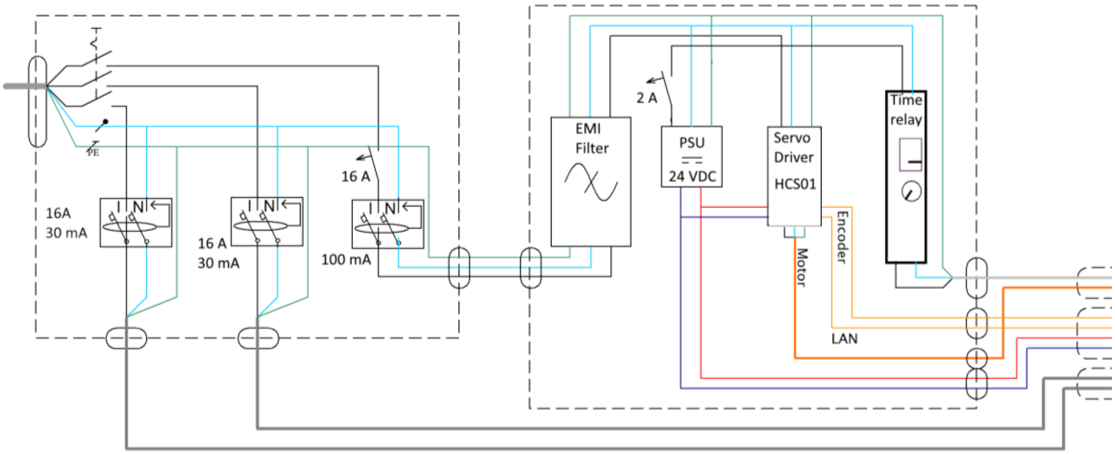

Figure S-4: Power distribution to servo drive controllers HCS01.

A whole QO table with all individual components was supplied by Thomas Keating Ltd company. In Figure S-5 is a top view of QO table, that is complementary to Figure 27. Gaussian beam starts and ends its journey in feed horns. Elliptical mirrors are placed within certain distances to refocuses the beam. When the beam reaches the first polarizer its components are reflected, absorbed, or passes through. Other polarizers ensure, that the unwanted component is properly filtered out. Simple metallic mirrors are used to extend and match a travel distance of the RF and LO beams. Finally, a wave that carries the EPR signal is combined with a wave from a local oscillator, for a heterodyne detection.

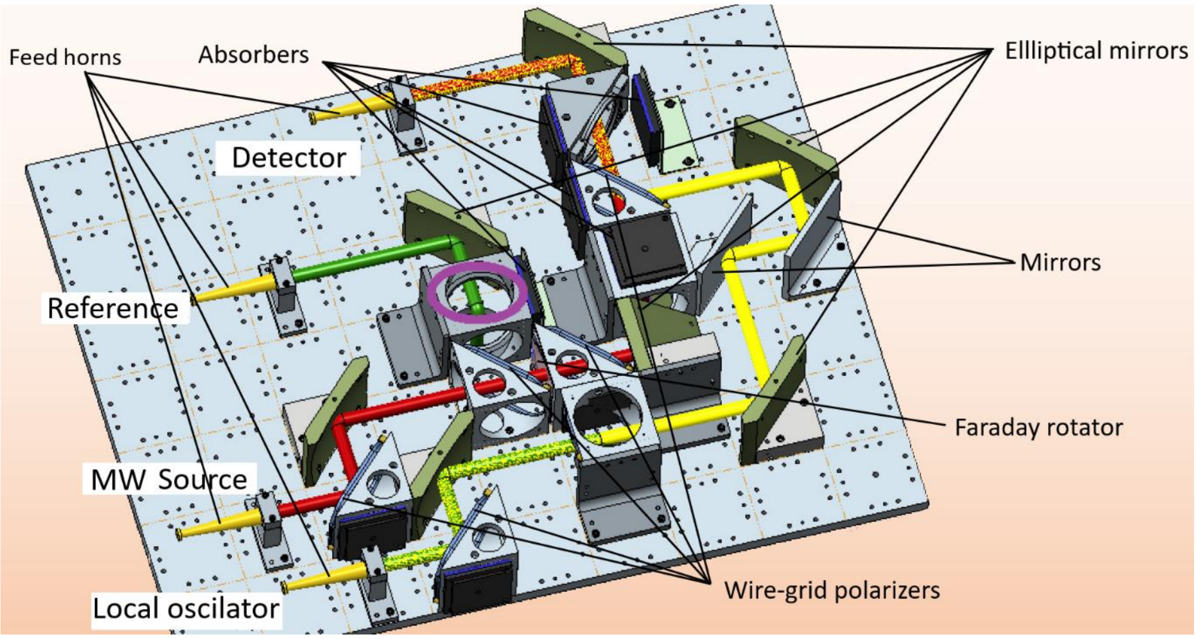

Figure S-5: Diagram of terahertz beam pathways in quasi-optical table.

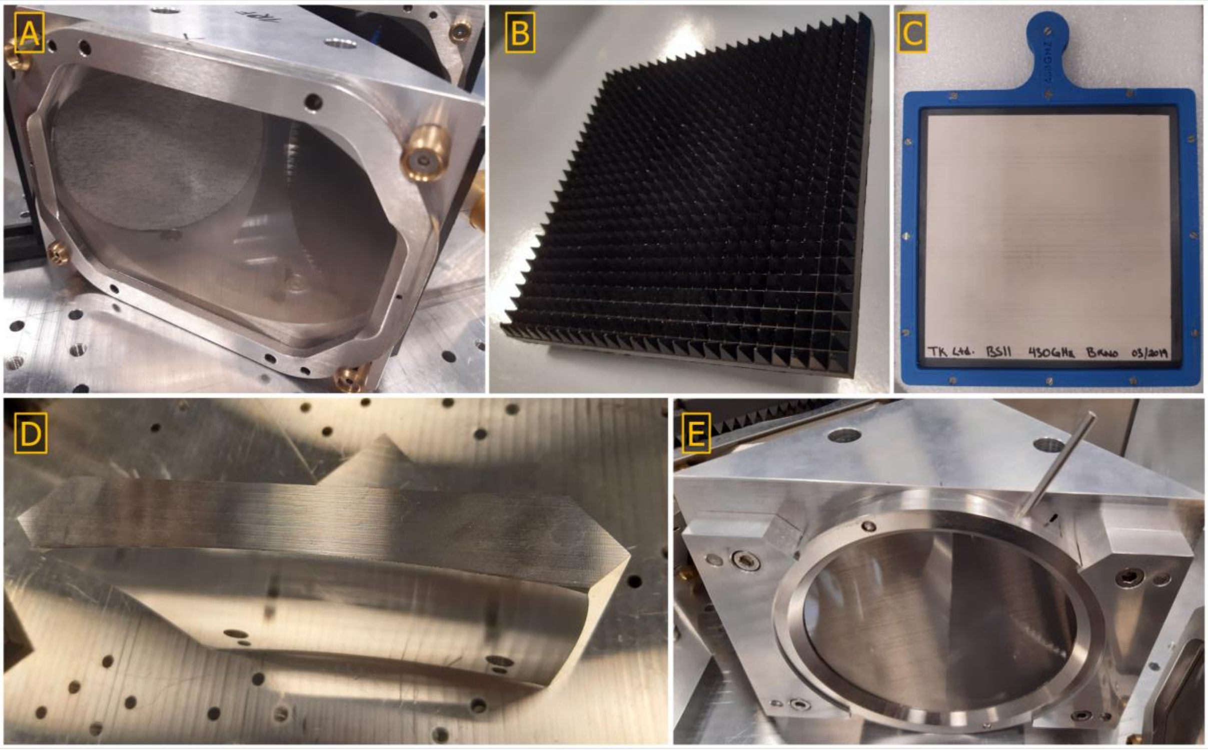

Figure S-6: QO components. A) Polarization wire grid (polarization parallel to the wires is reflected), B) Absorber, C) Faraday rotator (rotates polarization by 45 °), D) Elliptical mirror (refocuses a beam) E) Adjustible polarization wire grid.

Excitation and detection system

Main components of the excitation and detection system were bought from the Virginia Diodes, Inc company. An excitation part consists of two synthesizers, an amplification and multiplication chain (AMC), passive doublers and triplers. The synthesizers generate a microwave radiation in a range 8-20 GHz with a 20 Hz resolution. A signal frequency from synthesizers is multiplied in the AMC to 82-170 GHz. Moreover, by a combination of doublers and triplers, the maximum achievable frequency is 1020 GHz (Table S-2). Detectors work as a mixers therefore they can be used either for homodyne or heterodyne detection. A block scheme of heterodyne detection setup is in the Figure 26. Signal from one synthesizer is used for excitation of the sample, while the second (tracking) synthesizer serves as a local oscillator. An intermediate frequency must be chosen with respect to a sweep rate and the multiplication factor. A part of both signals is deflected in QO system to the reference mixer. The rest of the signal continues to the measurement mixer. Resulting signal at intermediate frequency from both mixers one more down converted. A difference of both signals cancels inconsistency between two sources, resulting in a pure EPR signal.

Table S-2:Frequency ranges for various configurations of terahertz sources.

Range [GHz]	82–125	110–170	170–250	250–375	325–500	500-750	750-1100
λ [mm]	3.66–2.4	2.73–1.76	1.76–1.2	1.2–0.799	0.922–0.6	0.6–0.4	0.4–0.273
Multipliers	**9**(AMC)	**12**(AMC)	**9**(AMC) **x2**	**9**(AMC) **x3**	**12**(AMC) **x3**	**9**(AMC) **x2 x3**	**9** (AMC) **x3 x3**
Output flange	WR9.0	WR6.5	WR4.3	WR2.8	WR2.2	WR1.5	WR1.0
Horn vendor	Thomas Keating	Bridge12	Thomas Keating	Thomas Keating	Thomas Keating	Thomas Keating	Thomas Keating
Power [dBm] avg. | min.	20 | 17	17 | 14	11 | 7	5 | 0	1.6 | -3.7	-7 | -19	-18 | -28
Power [mW] avg. | min.	100 | 50	50| 25	12.5 | 5	3 | 1	1.4 | 0.43	0.2 | 0.013	0.015 | 0.0016

The resulting signal is then either sampled by a fast digitizer in FRaScan EPR measurements, or in case of CW and FS EPR measurements it is demodulated by a medium frequency lock-in (MFLI) amplifier from the Zurich Instruments company. MFLI also generates a reference signal for a magnetic field modulation. For this we use a differential coaxial output that provides shielding to modulation signal. One of the coaxial cables goes through an amperemeter, that is used to measure the alternating current flowing through the modulation coil, which is proportional to modulation of magnetic field. A tuning capacitors placed in a shielded box are used only if modulation frequency is above 20 kHz, to reach the higher modulation amplitude.

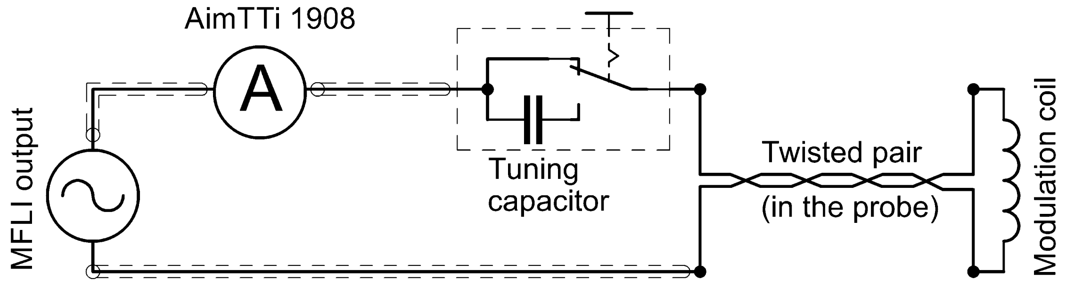

Figure S-7: Modulation subsystem scheme.

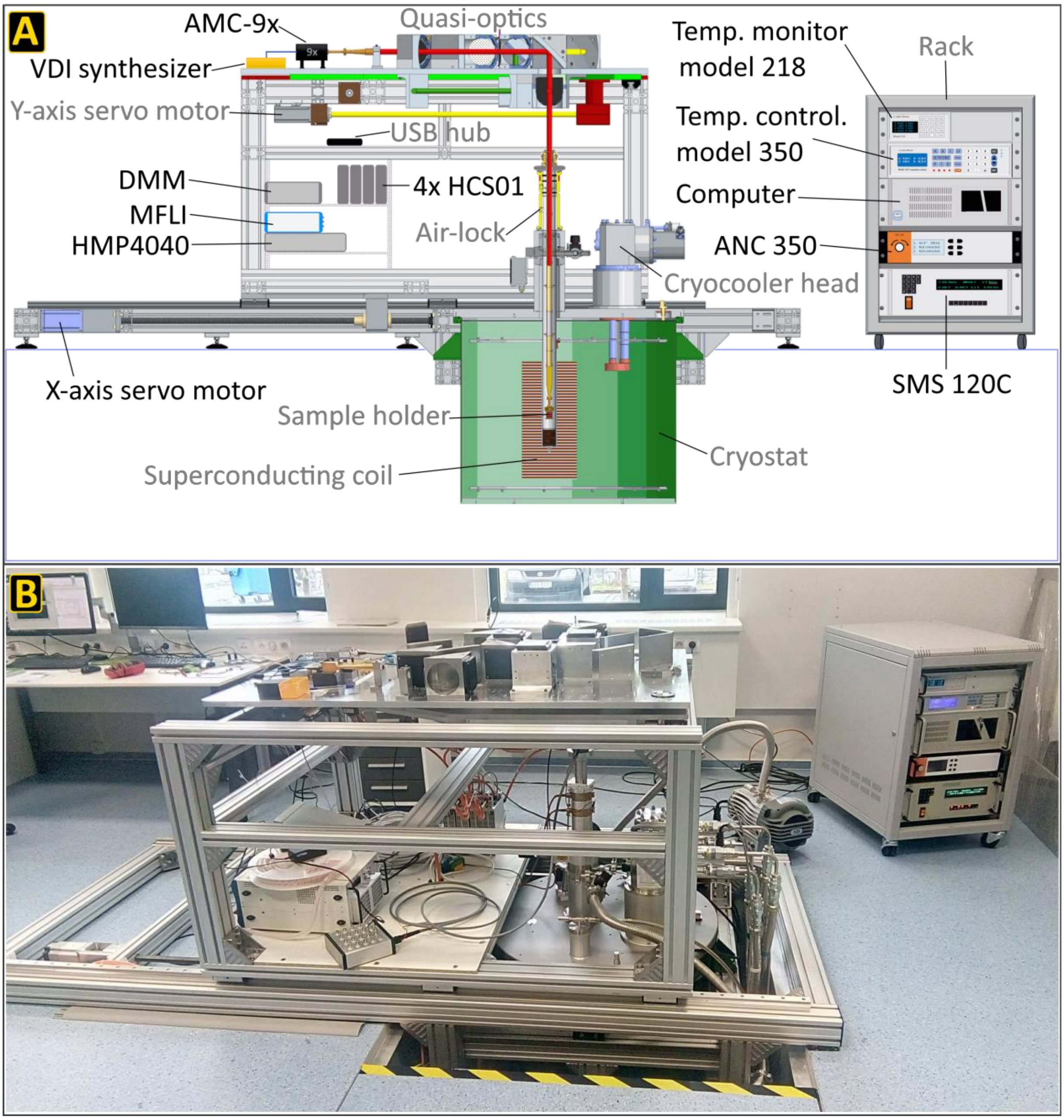

Figure S-8: A- cross section view from a side of the spectrometer. B- early state of the spectrometer (2019)

Other used instrumentation

Field sensor

Power supply unit (PSU) does not provide reliable information about actual magnetic field and ramp rate. There are two main sources of error. First, the PSU communication interface has a low baud rate and querying actual magnetic field and ramp rate may take up to 500 ms. If we consider most used ramp rate 3 mT/s, this may lead in offset of 1.5 mT along whole range. Second, high inductance of superconducting coil causes that magnetic field is delayed from electric current and does not rise up linearly on a start-up. Effect of both errors are higher with a ramp rate. Therefore, a magnetic field sensor was implemented to provide correct information about magnetic field.

A Lake Shore Cryotronics Hall sensor HGCT-3020 with operating temperature down to 1.5 K was used. Its sensitivity is about 10 mV/T (nominal current 100 mA) and has up to 2% linearity error in 15T range. To drive a sensor with electrical current and read out a voltage we use source meter unit (SMU) Keithley 2450. SMU is connected from the rear panel by coaxial cables to a small distribution box, where wires are reconnected to shielded measuring cable composed of twisted pairs, that is shared with temperature sensor and heater. All signals are DC, therefore no interference is expected. Furthermore, phosphor bronze twisted pair wires (32 and 36 AWG) were used inside of EPR probe. The sensor itself was placed in axis with sample, right below a mirror that reflects microwaves.

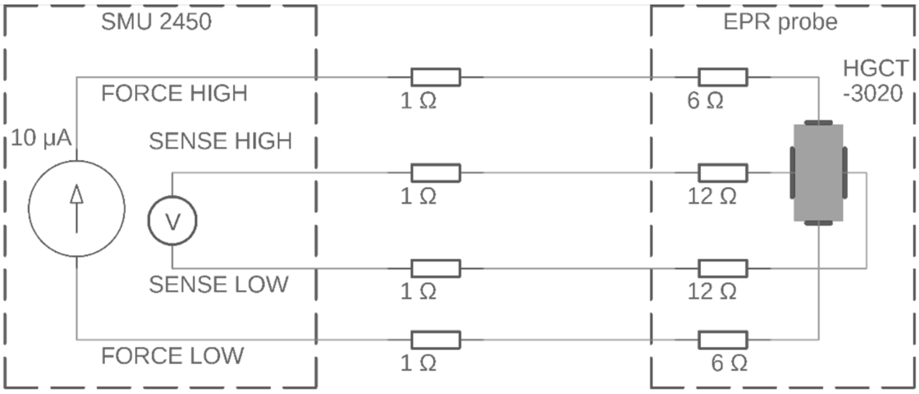

Figure S-9: Scheme of hall sensor connection. The resistors represent resistance of leads.

The SMU is set in a four-wire configuration (remote sense), in which output is set as a source of constant current (100 mA) and input reads the voltage (200mV range) from sensor. Integration time is set to four power line cycles (4 PLCs = 80 ms). Source Readback and Auto Zero functions are done only once, when measurement is started and then are disabled to allow read input value in 100 ms intervals that matches a read-out interval of a Lock-in amplifier, to keep EPR signal data paired with magnetic field data. Measured voltage is then converted in magnetic field by equation:

$$B = (V_h - V_0)/S_{Hh}$$

where S_h and V_0 are sensitivity constant and offset voltage of sensor respectively, V_h is the measured voltage on the hall sensor.

By EPR measurements on sample (MgO:Cr) with well-known g-factor 1.9897, a more accurate sensitivity constant and offset voltage were determined to be S_h= 10.2 mV/T, and V_0= 37 μV. Measurements were done at different microwave frequencies and at temperatures from 290 K to 10 K. It was found that at low temperatures, heat produced by the sensor is not negligible, therefore a smaller driving current is recommended (10-. Moreover, in a high magnetic field (> 5 T) and in cryogenic temperatures (< 150 K) a significant deviation in form of oscillations in measured field. (Visible if $B_{measured}$ - B_{read} is ploted as function of B_{read}). These are in range of accuracy declared on datasheet of sensor. Intensity and periodicity of oscillations increase with a magnetic field and. Decreasing temperature also increases amplitude of oscillations but has no effect on periodicity. This behavior indicates that deviation in sensed voltage is caused by a Shubnikov-de Hass conductivity oscillations in active material of the Hall sensor. They can be described by formula:

$$\frac{\Delta\sigma_{osc}}{\sigma_0} = \frac{5}{2}\sqrt{\frac{\pi e\hbar B}{E_F m^* S''_{extr}}} \cdot \sum_{p=1}^{\infty} \frac{1}{\sqrt{p}} R_T(p) R_D(p) R_S(p) \cos\left[2\pi p\left(\frac{B_F}{B}\right) - \gamma + \delta\right],$$

$$where{:}\ R_T(p) = \frac{\alpha \frac{m^*}{m_e}\frac{T}{B}}{\sinh\left(\alpha p \frac{m^*}{m_e}\frac{T}{B}\right)}, \qquad \alpha = \frac{2\pi^2 k_B m_e}{\hbar e},$$

$$R_D(p) = \exp\left(-\alpha p \frac{m^*}{m_e}\frac{T_D(\tau)}{B}\right), \qquad T_D = \frac{\hbar}{2\pi k_B \tau},$$

$$R(p) = \cos\left(\frac{\pi}{2} pg \frac{m^*}{m_e}\right)$$

where m_e is the mass of electron, m^* is an effective mass, k_b is the Boltzmann constant, $\hbar$ is the reduced Planck constant, e is elementary charge E_F is fermi energy, B_F is field of fundamental frequency σ_0 is conductivity at zero magnetic field, γ is a phase term, δ is a phase factor and p is an integer number. (Equation 2.27 in *"Johannes M. Schneider. ELECTRONIC PROPERTIES OF GRAPHITE. Physics. Grenoble;Université Joseph-Fourier - Grenoble I, 2010. English. tel-00547304,"*)

Based on this, the SdH oscillations were modeled in MATLAB by a simplified formula. On the Figure S-10 is shown that by subtraction of modeled oscillations the measured magnetic field is more linear (more correct results). By iterating this process should converge to more accurate results, and only nonlinearity would be at the beginning of magnetic field ramp.

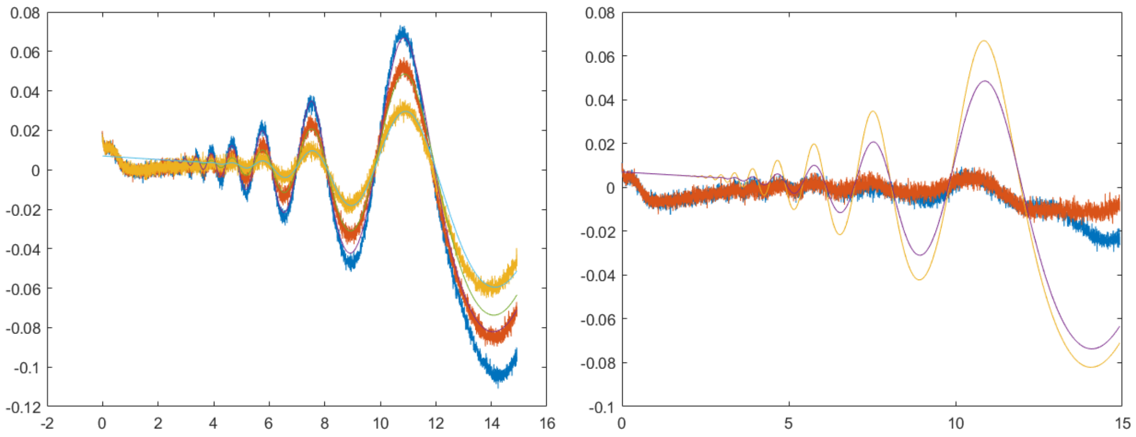

Figure S-10: Left- Deviations in the magnetic field caused by SdH conductivity oscillations and modelled fit for several temperatures. Right- modelled oscillations and result after their subtraction. On axis is a magnetic field in T.

Uninterruptible power supply

During a simulated blackout, it appeared that central backup power supply in the building has unacceptable delay for the magnet system. A UPS need to be installed for PSU, PC, TM, and TC. First, the measurement of the systems power consumption was done by a wattmeter DT-26 to estimate maximum power load. The magnetic field was gradually increased by step of 2 T up to 16 T and the power consumption was recorded one minute after reaching the target value. Resulting dependency of the power drain on the magnetic field is in Figure S-11. It should be noted that these values are valid for a stable magnetic field. When field is ramped up, a power consumption can be higher by 40 %. For that reason, an uninterruptible power supply (UPS) unit should be able to provide at least twice as much power than is required at maximum field. Further, it should have an output to trigger an emergency discharging of the magnet.

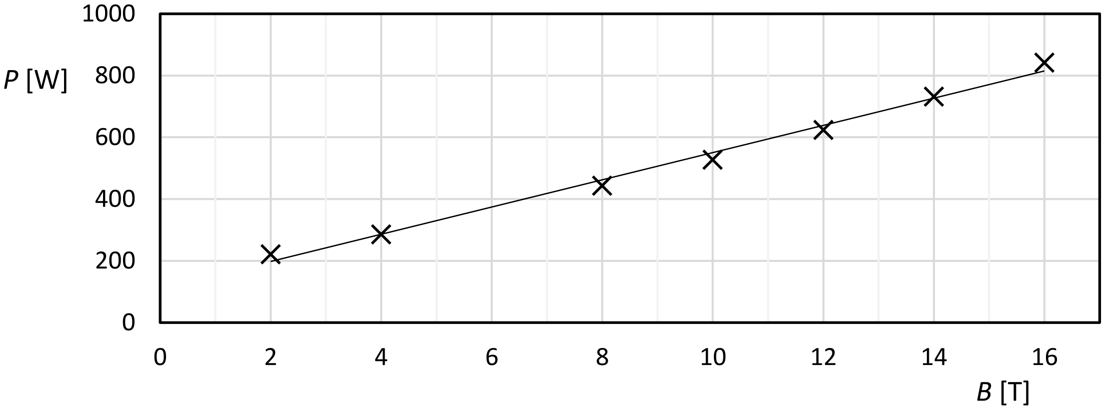

Figure S-11:Dependency of the magnets system power consumption on magnetic field

Finally, *PR2200ELCDSL* (Cyber Power Systems, Inc.) of a *line-interactive* topology was chosen for its short transfer time (4 ms), sufficient power and high effectivity. Another advantage was that this UPS is *plug and play* device, which means that generic driver of operating system *Windows* interprets USP as battery power supply. This allows simple check of AC power by calling a system function *GetSystemPowerStatus*. However, after setting up the UPS and few tests it was found, that this UPS creates interference, probably originating from a high-power switching component. On **picture bellow** it is shown a record from oscilloscope connected to 5 V linear DC power supply, that was powered by UPS.

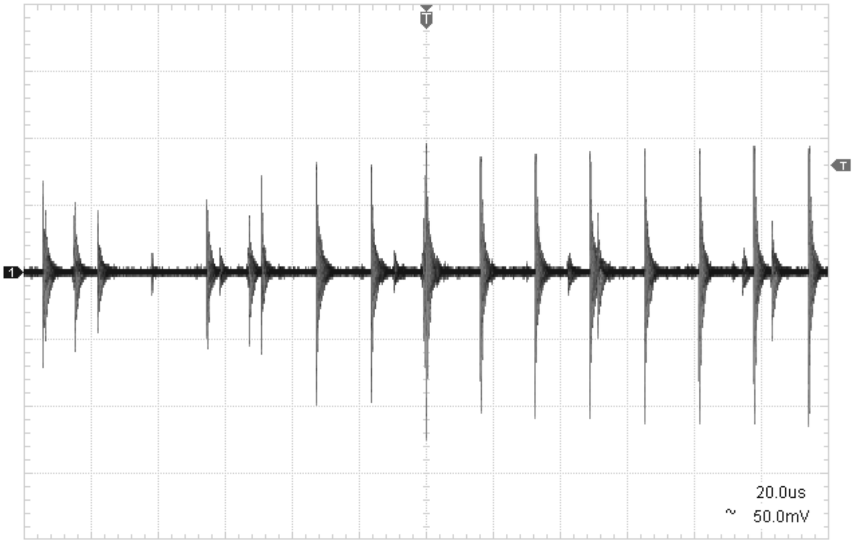

Figure S-12: Spike interference of PR2200ELCDSL

This behavior was consulted with manufacturer, who advised us to try UPS *OLS3000E* with *Online* topology (sometimes called *double conversion*). Advantage of this topology is a zero-transfer time, because UPS converts AC power to DC which is used to charge battery and also power output inverter, that continuously generates AC power again. Disadvantage is slightly higher acoustic noise and lower power efficiency. Same test as previously was done to check interference from UPS. Recording from oscilloscope is shown on **picture bellow**. Spikes decay much faster and their period is approximately double compared to previous case. Anyway, it was decided that not even this UPS is suitable to our needs.

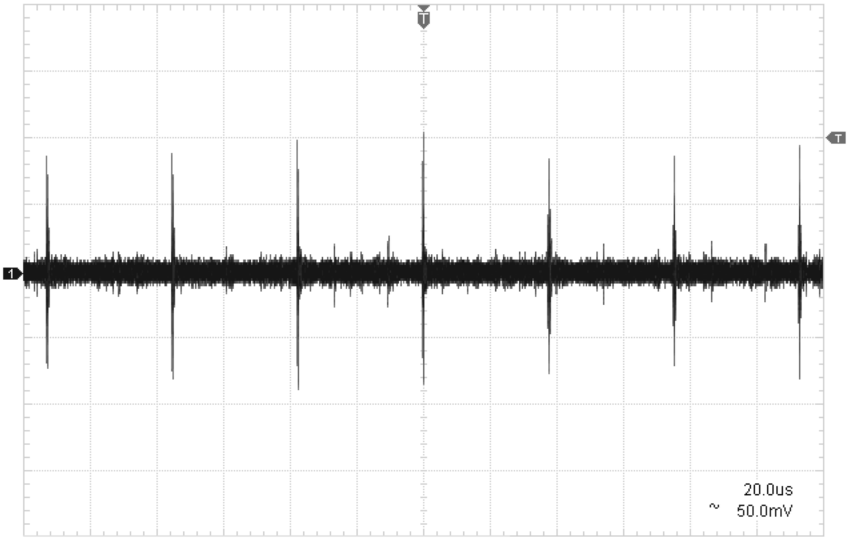

Figure S-13: Spike interference of OLS3000E

Later, two more UPS systems with *Online* topology were tested in the same way. Records made by oscilloscope for *ZP120N-3K* from G-Tec and *SEP 2200* from Riello company are shown at pictures **A** and **B** respectively. Unfortunately, both UPS does not behave as plug and play battery source, and manufacturer does not provide such driver. Therefore, communication would be difficult. Some communication protocols were found at website: https://networkupstools.org/ups-protocols.html. Alternatively, it is possible to use control signals of RS232 interface (Figure S-16) to check status of the UPS. While the LabVIEW can access properties and individual signals of serial ports, this was successfully tested. However, the USP backs-up only power for the PC, the power supply SMS120C, the temperature monitor 218, the temperature controller 350, the piezo driver ANC 350 and the Keithley 2450. Other instruments such as microwave synthesizers, loc-in amplifier, and servo drivers will be shut down during power outage. Moreover, the compressors and cryocoolers may stop working even if there is no problem with electric power. This can be caused by decree in flow of cooling water, and safe shutdown of compressors to prevent their overheating. For this reason, the compressors F-70 should be also monitored. This can be done again via serial interface, as the communication protocol of the compressors is described in manual. Unfortunately, one of the compressors has malfunction in its communication interface so only the second one can be properly monitored. Since the compressors are in separate room, a cabling has to be done first. Alternatively, a customized LTP interface could be used.

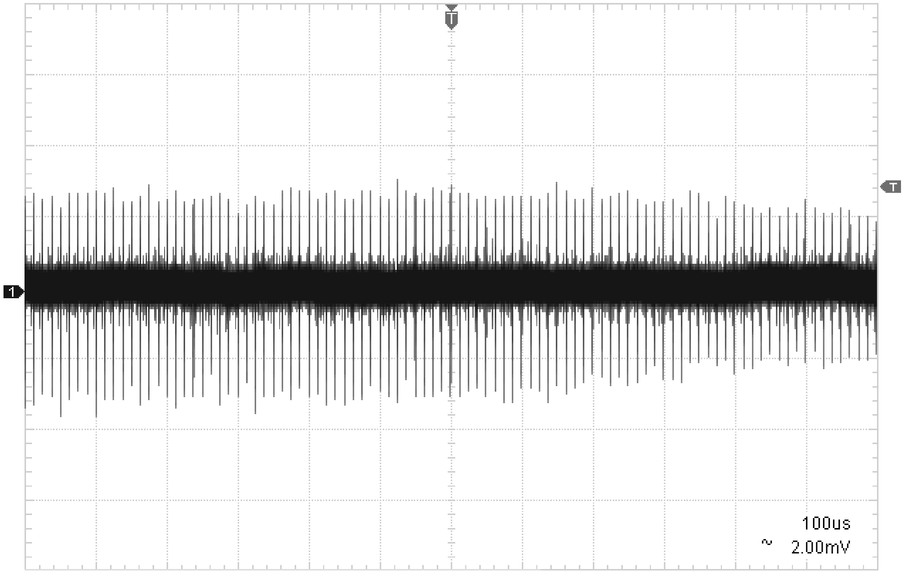

Figure S-14: Spike interference of ZP120N-3K

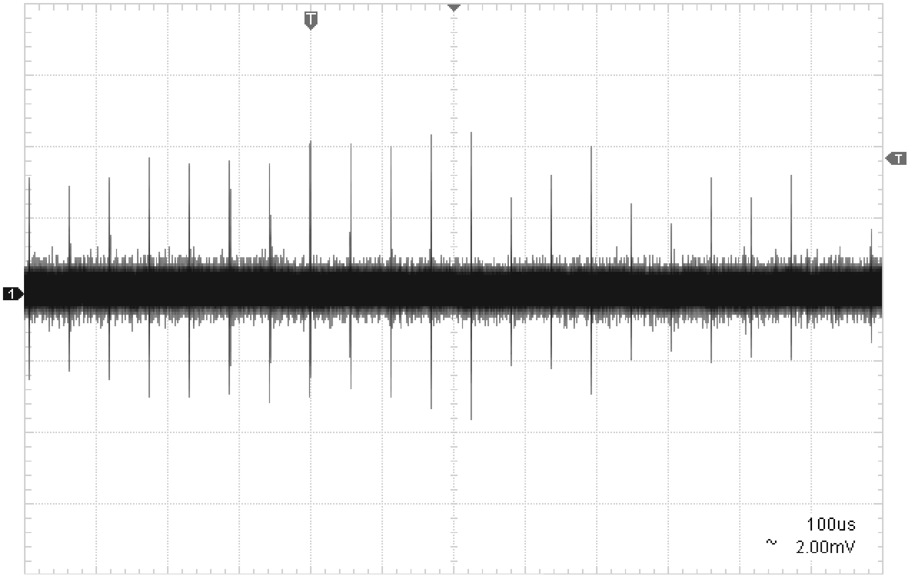

Figure S-15: Spike interference of SEP 2200

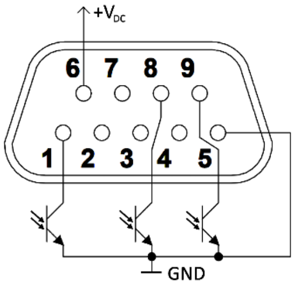

Pin	Signal (note)
1	Prog. output (default: UPS in lock)
2	TXD
3	RXD
5	GND
6	Power supply ($V_{CC} \approx 12$ V, $I_{MAX} = 20$ mA)
8	Prog. output (default: low battery)
9	Prog. output (default: battery operation)

Figure S-16: Rear panel monitoring and control port of SEP 2200

Appendix B – Software for a HFEPR spectrometer

Software development

An inseparable part of the spectrometer is a custom-made software. It must accomplish several tasks:

- A user friendly and intuitive environment for an easy operation.
- A safe and reliable control of the superconducting magnet up to 16 T.
- Work with various instruments together.
- Control of servo drives in all axes to adjust the QO table in the right position.
- Setting the parameters of experiment – microwave power, sweeping rate, temperature in a sample space, angle of sample rotator, carousel sample holder.
- Execute a different type of measurements – CW-EPR, frequency rapid-scan.
- Combine sequences of operations into automated experiments.
- Receiving of a raw data from digitizer and its processing into EPR spectrum.
- Export of measured data in standard format for further analysis.
- Import data from previous measurements.
- Solve common errors and log unexpected errors.
- Transformation of measured spectra into frequency/field maps.

To comply given requirements, we suggest that the software solution should meet following properties:

- Responsivity – The user interface must react to the operator’s actions with a negligible delay. The operator must be informed about the change of instrument settings, and about the reason why his action was denied if that is the case.
- Visualization of results – Measured data must be displayed in real-time in a graph. The software must be able to load previously measured and saved data and compare results. Application of post-processing routines on the data as smoothing, baseline correction, phase correction, and field shift correction is favorable.
- Safety – Software must be developed considering the possibility of hazardous situations caused either by the direct action of the operator or as a consequence of instrument settings. Spectrometer must react also to external influences such as a power outage or sudden failure of some instrument. In some cases, an operator must be prompted to confirm his action. Data must be recorded on a hard drive during measurement. Events must be logged for later analysis.
- Modularity – Each subsystem has its self-contained software module. A module monitors the state of the instrument and can react to the internal change of state, or external events caused by the interaction of an operator.
- Unity – All modules report their state to a supervising entity, which also coordinates modules for the cooperation of instruments during the measurement procedure. Communication is unified and the format of messages is the same for all modules.

- Automation – Once all parameters are set, a batch of measurements is done without the interaction of the operator. The operator may modify the parameters of a particular measurement, which has not started yet. The operator can further stop the currently executed measurement. The tool for faster setting of parameters for the batch of measurements is favorable.

To build the software solution it was decided to develop it in the LabVIEW. The LabVIEW is a graphical programing IDE developed by National Instruments (NI), with intention to create environment for easy implementation of various instruments into scientific and industrial applications. Unlike most of programming tools, the LabVIEW is using a dataflow concept and a graphical interpretation of a code. Therefore, a design patterns as a finite state machine or producer-consumer loop are widely used in software applications created in the LabVIEW. A code editor consists of two windows. The first one is a front panel and the second one is a block diagram. Front panel is essentially a workbench for graphical user interface (GUI). Most common components of GUI are controls and indicators that have their representation in a block diagram as inputs and outputs respectively.

A software architecture for a custom-made HFEPR spectrometer is derived from queued message handler and event driven state machine. It implements a client-server model in a way that client is a main controller (supervising module) of measurement routine and servers are the individual modules (submodules) for each physical instrument. This approach guarantees parallel execution of a code for each module. A main controller is essentially an event-based state machine that handles user actions and sends commands to individual subordinate modules. It also processes responses from modules. Modules execute commands on dedicated instrument, while checking the validity of orders. In case when given command cannot be executed, an error message is sent to main the controller. Each module also regularly checks a status of the instrument and reports changes. Sending commands and reports between main controller and subordinated module is provided by a shared service called messenger. A messenger manages several FIFO buffers that serve as mailboxes. In Figure S-17 is a block diagram of sending a response from a module to the main controller. Each message contains an information about which module is sending the response, a cause of the response, particular data, and a time stamp when the response was sent. In case of a risen error on the input, instead of message data an error report is sent, and a string *"Error"* is added to the cause of response.

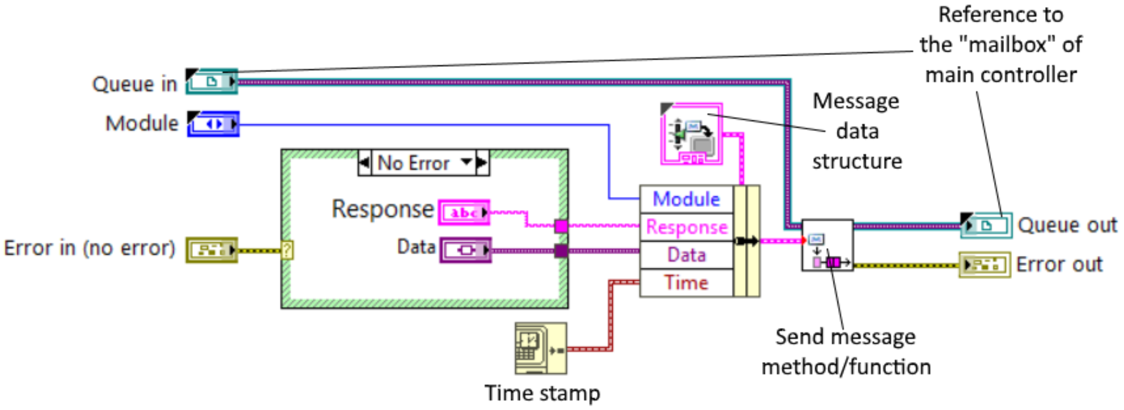

Figure S-17: Block diagram of sending a response from subordinated module.

List of used LabVIEW libraries and drivers for instruments:

- Lake Shore Cryotronics Temperature Monitor model 218 driver: http://sine.ni.com/apps/utf8/niid_web_display.model_page?p_model_id=1171
- Lake Shore Cryotronics Temperature Controller model 350 driver: http://sine.ni.com/apps/utf8/niid_web_display.model_page?p_model_id=21707
- Bosch Rexroth servomotor driver IndraDrive HCS01 driver: https://www.vipm.io/package/eal4labview/
- Virginia Diodes Microwawe Synthesizer driver: https://vadiodes.com/en/resources/downloads
- Attocube piezomotor controller ANC 350: For newest one, please contact Attocube https://www.attocube.com/en/contact/info-request and ask for ANC350_4.2.2_LV12.llb or newer. Alternatively, an older LLB can be found at: https://github.com/fuoar/CARODotManip/tree/92b688bc7234877625a4ee00df4d2d3d6db0faf5/Documentation/Attocubes/ANC350/Software, or one can create a wrapper VIs for 32 or 64 bit ANC350v4.dll from https://github.com/attocube-systems/ANC350_Python_Control.
- OpenG toolkit: https://www.vipm.io/package/openg.org_lib_openg_toolkit/
- MGI Library: https://www.vipm.io/package/mgi_lib_mgi_library/
- Gpower toolset: https://www.vipm.io/package/gpower_lib_all/
- Cryogenics Superconducting power supply SMS120C: Has to be requested from Cryogenics Ltd. http://cryogenic.co.uk/contact
- Zurich Instruments MFLI: in LabOne https://www.zhinst.com/europe/en/support/download-center/type/api/os/windows/platform/mf/current or available as API for LabVIEW
- ADQAPI: Is part of SDK from Teledyne SP Devices. Please contact them for more information at https://www.spdevices.com/who-we-are/contact-us. They also provide a LabVIEW driver, however that works only with FWDAQ firmware. User guides, manuals and ADQAPI **reference guide** can be found at: https://www.spdevices.com/en-us/Products_/Pages/ADQ7DC.aspx.

List of functions that are valid for ADQ7DC:

SetTriggerEdge (trigger, edge), SetTriggerInputImpedance (input_num, mode), SetTriggerMode (trig_mode), SWTrig ( ), SetTriggerThresholdVoltage (trigger, vthresh), SetLvlTrigChannel (channel), SetLvlTrigLevel(), ASetLvlTrigEdge(), SeternalTriggerPeriod (TriggerPeriodClockCycles), SeternalTriggerFrequency (Trig_Freq), SetExternalTriggerDelay (delaycycles), ResetTimestamp ( ), SetupLevelTrigger (level, edge, reset_level, channel_mask, individual_mode), SetupTimestampSync (mode, trig_source), SetTriggerMaskPXI (mask), GetNofChannels ( ), SetGainAndOffset (Channel, Gain, Offset), SetAdjustableBias (channel, ADCcodes), SSetAfeSwitch (afe), EnableClockRefOut (enable), EnableGPIOPort (port, enable); EnableGPIOSupplyOutput (enable), HasAdjustableBias ( ), HasAdjustableInputRange ( ), HasGPIOHardware ( ), HasTrigHardware (trignum), HasTrigoutHardware (trignum), HasVariableTrigThreshold (trignum), ReadGPIO ( ), ReadGPIOPort (port, data), SetDirectionGPIOPort (port, direction, mask), SetConfigurationTrig (mode, pulselength, invertoutput), SetupTriggerOutput (outputnum, mode, pulselength, invertoutput), WriteGPIOPort (port, data, mask), CCreateADQControlUnit ( ), DeleteADQControlUnit (adq_cu_ptr), ADQControlUnit_EnableErrorTrace (adq_cu_ptr, trace_level, trace_file_dir), ADQControlUnit_FindDevices (adq_cu_ptr),

ADQControlUnit_UserLogMessage (adq_cu_ptr, trace_level, _ message, ...),
GetPCIeAddress ( ), uGetUSBAddress ( ), HasFeature (featurename),
IsPCIeDevice ( ) , IsUSB3Device ( ), IsUSBDevice ( ), IsAlive ( ),
GetBoardProductName ( ), GetTemperature(addr, _ temperature),
ResetDevice (resetlevel), SetTestPatternMode (mode), BypassUserLogic (ul_target, bypass),
EnableUseOfUserHeaders (mode,api_value), EnableUserLogicFilter (channel, enable),
ResetUserLogicFilter (channel),
SetUserLogicFilter (channel,coefficients, length, format, rounding_method)
SetClockInputImpedance (input_num, mode), SetClockSource (source),
SetExternalReferenceFrequency (ref_freq), ArmTrigger ( ), DisarmTrigger ( ), GetAcquiredAll ( )
GetAcquiredRecords ( )
GetData(target_buffers, target_buffer_size, target_bytes_per_sample, StartRecordNumber,
NumberOfRecords, ChannelsMask, StartSample, nSamples, TransferMode),
GetDataWH (. . . . . ..), TGetDataWHTS (. . . . . .), MultiRecordClose ( ),
MultiRecordSetup (NumberOfRecords, SamplesPerRecord), SetPreTrigSamples (PreTrigSamples)
SetTriggerDelay (triggerdelay_samples), SetSampleSkip (DecimationFactor)
ATDEnableAccumulationGridSync (enable), ATDFlushWFA (),
ATDGetAdjustedRecordLength (record_length, search_direction),
ATDGetDeviceNofAccumulations (nof_accumulations),
ATDGetWFAStatus (wfa_progress_percent, records_collected,stream_status,wfa_status),
ATDRegisterWFABuffer (channel,buffer), ATDSetThresholdFilter (channel, coefficients),
ATDSetupThreshold (channel, threshold, baseline, polarity, bypass),
ATDSetupWFA (record_length,nof_pretrig_samples, nof_triggerdelay_samples, nof_accumulations, nof_repeats),
ATDSetWFAernalTimeout (timeout_ms), ATDStartWFA (target_buffers, channels_mask, blocking)
ATDStopWFA (), ATDUpdateNofAccumulations (nof_accumulations)
ATDWaitForWFABuffer (channel, buffer, timeout), ATDWaitForWFACompletion (),
SetTransferBuffers (nOfBuffers, bufferSize), GetNofDBSInstances (nof_dbs_instances),
SetupDBS (DBS_instance, bypass, dc_target, lower_saturation_level, upper_saturation_level),
SetupTriggerBlocking (mode, trig_source, u64_t window_length, tcount_limit), DisarmTriggerBlocking ( ),
ArmTriggerBlocking ( ), ArmTimestampSync ( ), DisarmTimestampSync ( ), ADQ_GetNofBytesPerSample(nofBpS)

Files

The developed software can create//load several datafiles. Here are some showed examples of an event logfile, temperature logfile, configuration file, script file and datafile.

Example of event log file:

```
2023-07-31 11.51 GUI initialized.
2023-07-31 11.51 Temperature controller 350 initialized.
2023-07-31 11.51 Magnet module initialized.
........ REMOTE CONTROL: ENABLED
........ EXTERNAL TRIP: DISABLED
........ FIELD CONSTANT: 0.14911 T/A
........ HEATER OUTPUT: 2.6 VOLTS
........ VOLTAGE LIMIT: 9.9 VOLTS
........ RAMP RATE: 0.00329 A/SEC
........ MID SETTING: 0.50000 TESLA
```

```
........ MAX SETTING: 16.10010 TESLA
........ HEATER STATUS: SWITCHED OFF AT -0.5000 TESLA
........ PAUSE STATUS: OFF
........ FILTER STATUS: ON
........ RAMP STATUS: HOLDING ON TARGET AT -0.4999 TESLA
........ LEVEL GAUGE: 0 mm
........ CURRENT DIRECTION: NEGATIVE
10:31:28 OUTPUT: -0.49920 TESLA AT 0.1 VOLTS
10:31:29 DATE: 31/07/2023
2023-07-31 11.51 Temperature monitor: 218E
2023-07-31 11.52 VDI Synth Rev 4bx2 is connected 548254584 and
VDI Tracking Synth is connected 548254736.
2023-07-31 11.53 DEV4029 connected as ACQ.
2023-07-31 12.19 Switching to persistent mode.
2023-07-31 12.20 Switching to ramping mode.
Setting magnetic field from -0.499900 [T] to 0.500000 [T] with
ramp 0.178932 [mT/s]
Warning: Custom ramp was adjusted
```

Example of temperature log file:

```
Time 1stStageA 2ndStageA 1stStageB 2ndStageB InnerCoil
OutercCoil ScSwitch SupportPlate VIT Sample Trap HePot Field/T

7/31/2023 11:51:47 AM 34.576 3.376 33.791 4.153 4.329 3.948
3.721 9.825 1.93867 4.97951 42.8908 4.58904 -0.5000

7/31/2023 11:52:09 AM 34.574 3.489 33.789 4.254 4.327 3.947
3.715 9.825 1.94066 4.98486 42.8828 4.58796 -0.5000
```

Config File

```
[Magnet Constants]
Switch resistant \5BK\5D = "5.000000"
Switch superconducting \5BK\5D = "4.200000"
First stage critical temperature \5BK\5D = "50.000000"
Second stage critical temperature \5BK\5D = "7.000000"
Inner magnet critical temperature \5BK\5D = "8.000000"
Outer magnet critical temperature \5BK\5D = "7.500000"
Field Constant \5BT/A\5D = "0.149110"
Maximum Current \5BA\5D = "107.300000"
Maximum field \5BT\5D = "16.000000"
Maximum source ramp \5BA/s\5D = "0.5"
Source precision \5BT\5D = "0.0004"
Ramp limits \5BA/s\5D = "<size(s)=5> 0.050600 0.038000
0.028500 0.021300 0.010400"
Field limits \5BT\5D = "<size(s)=5> 3.000000 9.600000
13.300000 15.500000 16.000000"
SMS = "\00\00\00\04COM3"
LSC218 = "\00\00\00\04COM1"
```

```
[Servo config constants]
IP addresses.<size(s)> = "5"
IP addresses 0 = "192.138.4.1"
IP addresses 1 = "192.138.4.2"
IP addresses 2 = "192.138.4.3"
IP addresses 3 = "192.138.4.4"
IP addresses 4 = "192.138.4.5"
Axis limits \5Bmm\5D = "<size(s)=2> 80.000000 20.000000"

[THz parameters]
Base frequency \5BGHz\5D = "210.000000"
Sweep rate \5BGHz/s\5D = "0.000000"
End frequency \5BGHz\5D = "0.000000"
Im frequency \5BMHz\5D = "10.000000"
AMC = "9"
Multip = "2"

[ACQ parameters]
Filter order = "7.000000"
Filter constant \5Bms\5D = "10.000000"
F_Mod \5BkHz\5D = "193.100000"
Amp_Mod \5BmV\5D = "1036.071777"
Enable output = "1"
Phase \5B°\5D = "0.000000"
Time constant \5Bms\5D = "0.050771"

[VID control]
Base frequency \5BGHz\5D = "185.000000"
Sweep rate \5BGHz/s\5D = "10.000000"
End frequency \5BGHz\5D = "245.000000"
Im frequency \5BMHz\5D = "1880.000000"
AMC = "9"
Multip = "2"
Sweep up \5Bms\5D = "512.000000"
Reset trigger? = "TRUE"
```

Example of script file for CW measurements with various crystal orientation:

```
[Info]
Rounds = 2
Multiplication factor = 9

[0]
Start = "-3.000000"
Start Caption = "Start [T]"
End = "3.000000"
End Caption = "End [T]"
Sweep = "1.000000"
Sweep caption = "Rate [mT/s]"
Constant = "283.000000"
Constant caption = "Freq [GHz]"
Mod_F \5BkHz\5D = "100.000000"
Mod_A \5BG\5D = "2.000000"
Tau \5Bms\5D = "100.000000"
Angle \5B°\5D = "20.000000"
Tmp \5BK\5D = "3.000000"
Wait \5Bmin\5D = "1.000000"
Carousel = "0"
Comment = "HOPG1"
Auto-mod = "TRUE"
Execute = "TRUE"

[1]
Start = "-3.000000"
Start Caption = "Start [T]"
End = "3.000000"
End Caption = "End [T]"
Sweep = "1.000000"
Sweep caption = "Rate [mT/s]"
Constant = "283.000000"
Constant caption = "Freq [GHz]"
Mod_F \5BkHz\5D = "100.000000"
Mod_A \5BG\5D = "2.000000"
Tau \5Bms\5D = "100.000000"
Angle \5B°\5D = "21.000000"
Tmp \5BK\5D = "3.000000"
Wait \5Bmin\5D = "1.000000"
Carousel = "0"
Comment = "HOPG2"
Auto-mod = "TRUE"
Execute = "TRUE"
```

Table S-3: Data structure of CW-EPR text files

Operator:	[personal name] *(example: Sedivy)*				
Global comment:	[text] *(A note valid to all measurements in series. Example: 4H-SiC:V from Prague)*				
Local comment:	[text] *(A note valid to a single measurement. Example: Lower frequency)*				
Measurement mode:	[mode] *(example: CW7_20 = continuous wave 2020)*				
Sample holder:	[holder name] *(example: Simple)*				
Created:	[date] *(example: Saturday, July 16, 2022 5:54 PM)*				
Field sweep:					
Start:	[value] [unit] *(example: 9.5 T)*				
End:	[value] [unit] *(example: 11.5 T)*				
Rate:	[value] [unit] *(example: 1 mT/s)*				
Frequency:	[value] [unit] *(example: 283.07 GHz)*				
Angle:	[value] [unit] *(example: -1 °)*				
Temperature:	[value] [unit] *(example: 74 K)*				
Stabilization delay:	[value] [unit] *(example: 5 min)*				
Modulation amplitude:	[value] [unit] *(example: 3 G)*				
Modulation frequency:	[value] [unit] *(example: 10 kHz)*				
Filter time constant:	[value] [unit] *(example: 150 ms)*				
Carousel position:	[value] [unit] *(example: 0)*				
________________					
Field_expected	*Signal_X-ch*	*Signal_Y-ch*	*VTI_Temperature*	*Modulation*	*Field_actual*
[T]	*[V]*	*[V]*	*[K]*	*[A]*	*[T]*
9.5000E+0	*2.4990E-6*	*2.4630E-6*	*7.4190E+1*	*1.0000E-2*	*9.5000E+0*
9.5001E+0	*2.5020E-6*	*2.4550E-6*	*7.4190E+1*	*1.0000E-2*	*9.5000E+0*

Other micro applications

Two applications were created for initial processing and data reduction of large datafiles such as 2D-EPR maps, and sets of FS-EPR spectra. Another application was made to obtain calibration data for temperature sensors. An application to automate FTIR spectra acquisition with dependence on magnetic field was also created.

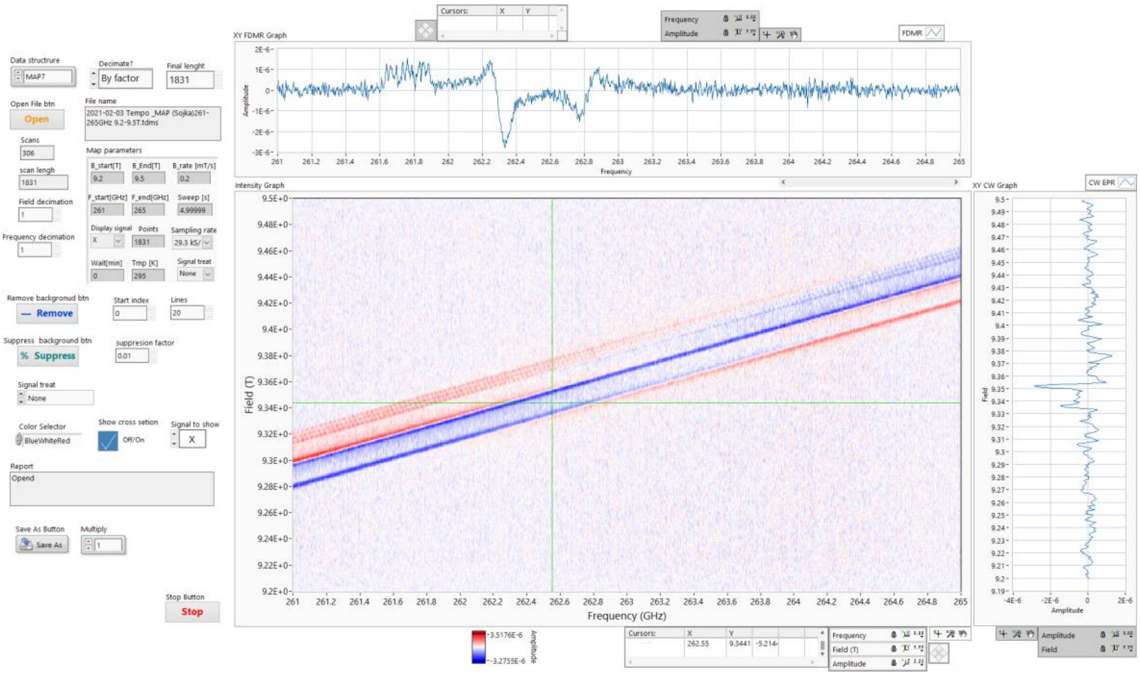

Data structrure: MAP7
Decimate?: By factor
Final lenght: 1831
File name: 2021-02-03 Tempo _MAP (Sojka)261-265GHz 9.2-9.5T.tdms
Scans: 306
scan lengh: 1831
Field decimation: 1
Frequency decimation: 1
Map parameters
B_start[T]: 9.2
B_End[T]: 9.5
B_rate [mT/s]: 0.2
F_start[GHz]: 261
F_end[GHz]: 265
Sweep [s]: 4.99999
Display signal: X
Points: 1831
Sampling rate: 29.3 kS/
Wait[min]: 0
Tmp [K]: 295
Signal treat: None
Start index: 0
Lines: 20
suppresion factor: 0.01
Signal treat: None
Color Selector: BlueWhiteRed
Show cross setion: Off/On
Signal to show: X
Report: Opend
Multiply: 1

Figure S-18: Post processing application for visualization of 2D-EPR maps. It can reduce background, decimate dataset, extract CW/FS-EPR spectra.

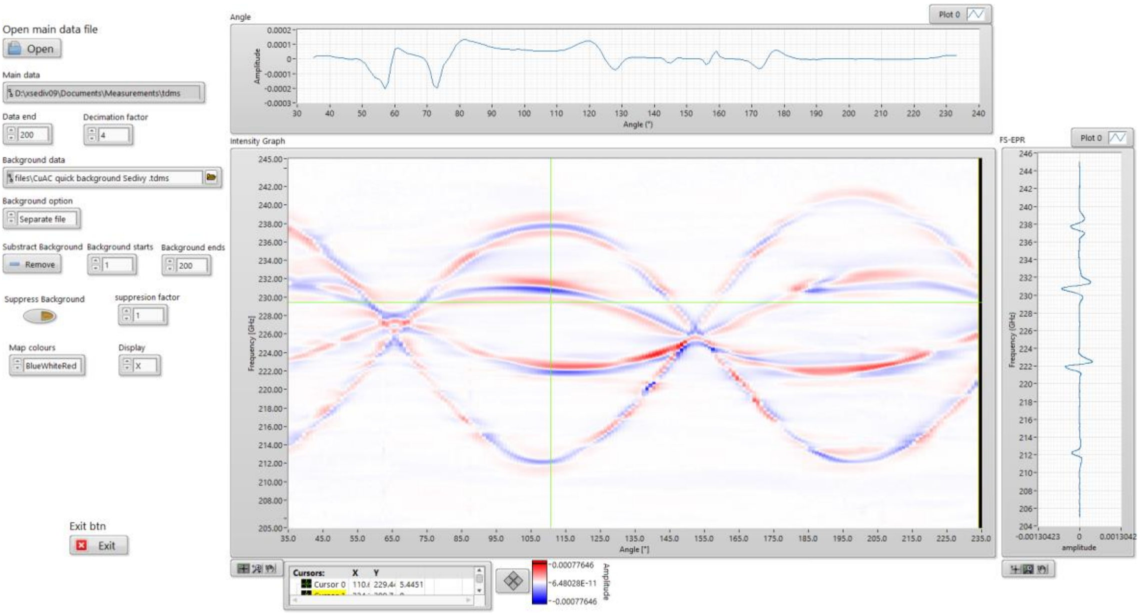

Main data: D:\xsediv09\Documents\Measurements\tdms
Data end: 200
Decimation factor: 4
Background data: files\CuAC quick background Sedivy .tdms
Background option: Separate file
Background starts: 1
Background ends: 200
suppresion factor: 1
Map colours: BlueWhiteRed
Display: X

Figure S-19: Post processing application for visualization of multiple FS-EPR spectra of oriented crystals. It can subtract background, decimate dataset in frequency domain, extract FS-EPR spectra.

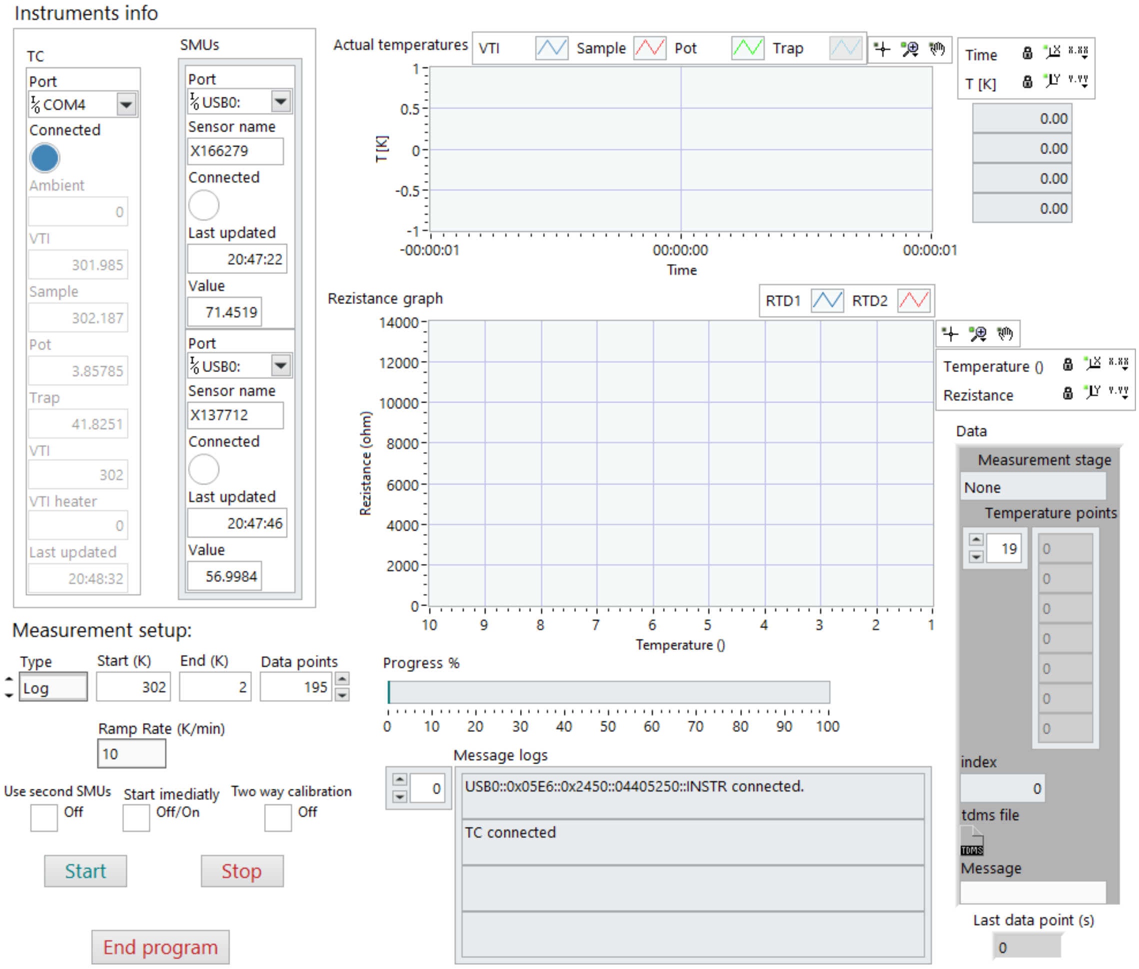

TC
Port
COM4
Connected
Ambient
0
VTI
301.985
Sample
302.187
Pot
3.85785
Trap
41.8251
VTI
302
VTI heater
0
Last updated
20:48:32

SMUs
Port
USB0:
Sensor name
X166279
Connected
Last updated
20:47:22
Value
71.4519
Port
USB0:
Sensor name
X137712
Connected
Last updated
20:47:46
Value
56.9984

Time
0.00
0.00
0.00
0.00

Measurement stage
None
Temperature points
19
0
0
0
0
0
0
0
index
0
tdms file
Message
Last data point (s)
0

Type
Log
Start (K)
302
End (K)
2
Data points
195
Ramp Rate (K/min)
10
Use second SMUs
☐ Off
Start imediatly
☐ Off/On
Two way calibration
☐ Off

Message logs
0
USB0::0x05E6::0x2450::04405250::INSTR connected.
TC connected

Figure S-20: A micro application for measurement of calibration curves

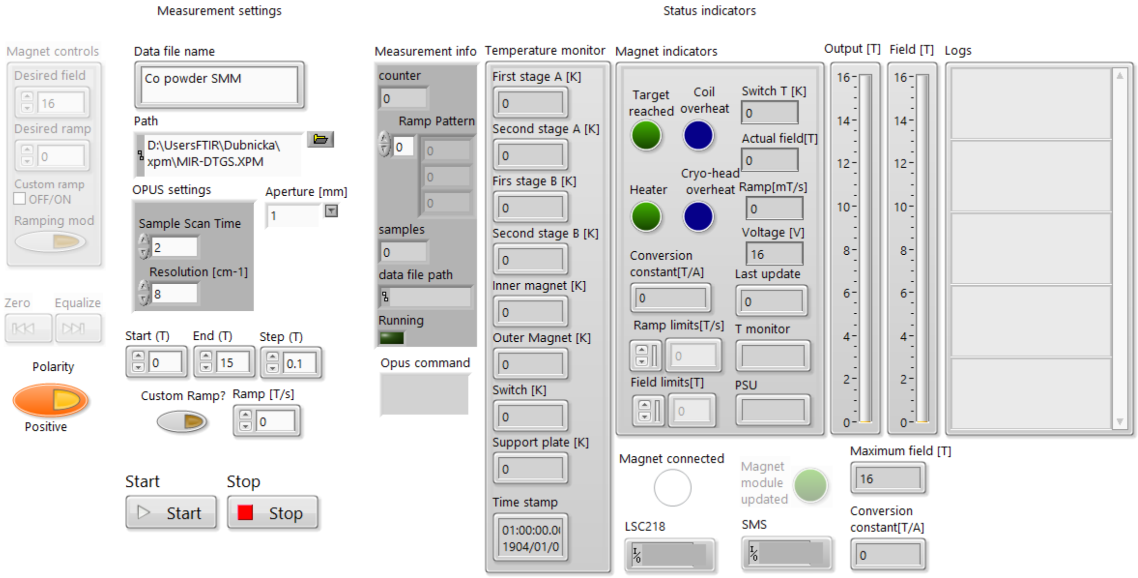

Desired field
16
Desired ramp
0
Custom ramp
☐ OFF/ON
Ramping mod

Data file name
Co powder SMM
Path
D:\UsersFTIR\Dubnicka\xpm\MIR-DTGS.XPM
OPUS settings
Sample Scan Time
2
Resolution [cm-1]
8
Aperture [mm]
1
Start (T)
0
End (T)
15
Step (T)
0.1
Ramp [T/s]
0

counter
0
Ramp Pattern
0
0
0
0
samples
0
data file path

First stage A [K]
0
Second stage A [K]
0
Firs stage B [K]
0
Second stage B [K]
0
Inner magnet [K]
0
Outer Magnet [K]
0
Switch [K]
0
Support plate [K]
0
Time stamp
01:00:00.0
1904/01/0

Switch T [K]
0
Actual field[T]
0
Ramp[mT/s]
0
Voltage [V]
16
Conversion constant[T/A]
0
Last update
0
Ramp limits[T/s]
0
T monitor
Field limits[T]
0
PSU

Maximum field [T]
16
Conversion constant[T/A]
0

Figure S-21: A micro application for measurement of magnetic field dependent FTIR spectra

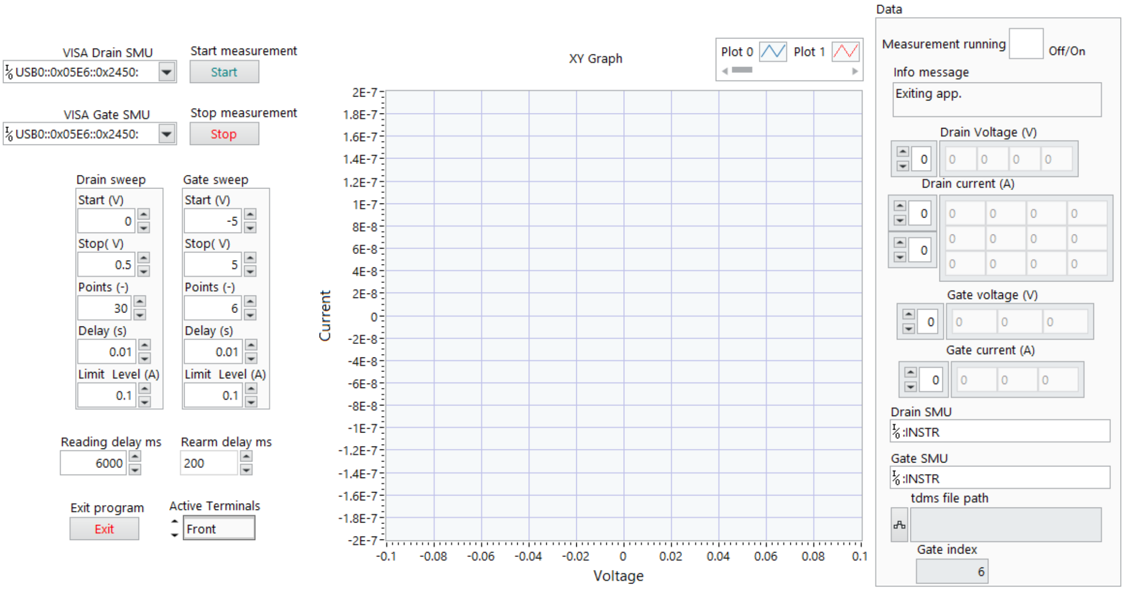
VISA Drain SMU
USB0::0x05E6::0x2450:

VISA Gate SMU
USB0::0x05E6::0x2450:

Drain sweep
Start (V) 0
Stop(V) 0.5
Points (-) 30
Delay (s) 0.01
Limit Level (A) 0.1

Gate sweep
Start (V) -5
Stop(V) 5
Points (-) 6
Delay (s) 0.01
Limit Level (A) 0.1

Reading delay ms 6000
Rearm delay ms 200

Active Terminals Front

Data
Measurement running Off/On
Info message
Exiting app.

Drain Voltage (V) 0
Drain current (A) 0
Gate voltage (V) 0
Gate current (A) 0
Drain SMU :INSTR
Gate SMU :INSTR
tdms file path
Gate index 6

Figure S-22: Screenshot of prototype program for automation of VA characterization.

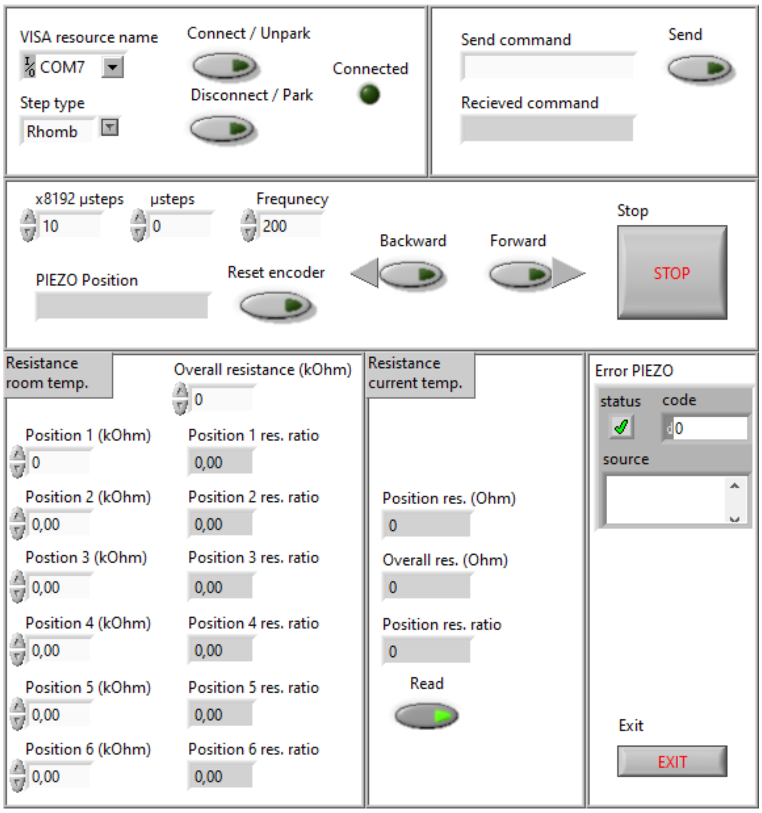
VISA resource name COM7
Step type Rhomb
Send command
Recieved command
x8192 µsteps 10
µsteps 0
Frequnecy 200
PIEZO Position

Resistance room temp.
Overall resistance (kOhm) 0
Position 1 (kOhm) 0
Position 1 res. ratio 0,00
Position 2 (kOhm) 0,00
Position 2 res. ratio 0,00
Postion 3 (kOhm) 0,00
Position 3 res. ratio 0,00
Position 4 (kOhm) 0,00
Position 4 res. ratio 0,00
Position 5 (kOhm) 0,00
Position 5 res. ratio 0,00
Position 6 (kOhm) 0,00
Position 6 res. ratio 0,00

Resistance current temp.
Position res. (Ohm) 0
Overall res. (Ohm) 0
Position res. ratio 0

Error PIEZO
status ✓
code 0
source

Figure S-23: Screenshot of prototype program for control of carousel sample holder.